Università degli Studi di Padova

DIPARTIMENTO DI FISICA E ASTRONOMIA "GALILEO GALILEI"
Corso di Laurea Magistrale in Astronomia

Tesi di Laurea Magistrale

Ionized gas metallicity in galaxies from the GASP Survey

Candidato:
Andrea Franchetto

Relatore:
Prof. Rodighiero Giulia

Correlatori:
Dr. Poggianti Bianca Maria
Dr. Gullieuszik Marco

Anno Accademico 2017-2018

Contents

Abstract

This thesis is performed in the context of GAs Stripping Phenomena in galaxies with MUSE (GASP) survey. The high-quality spectroscopic data provided by MUSE allow a spatially-resolved study of the ionized gas chemical abundance. This work aims to compare the gas-phase metallicity properties of 10 disk galaxies with no morphological anomalies and 12 gas-stripped galaxies with evident signs of unilateral debris and gas tails. The chemical abundance of the ionized gas is estimated analyzing the emission line fluxes in star-forming regions using the calibrator `pyqz` based on theoretical models of photoionization.

The analysis of the metallicity distribution derived in this work confirms that the normal galaxies are characterized by a clear negative gradient. Moreover, the gas-stripped galaxies also exhibit a negative metallicity gradient in the main galaxy body, though it is flatter, that continues in the gas tails. This suggests that the gas-removal process in these galaxies, mainly the ram-pressure stripping, eradicates the gas proceeding outside-in.

This work focuses also on the dependence of the metallicity on the global and local properties of galaxies, finding that the local chemical abundance of normal galaxies presents a clear correlation with the stellar mass density, while in gas-stripped galaxies there is a mismatch between these quantities.

The results in this work allow to improve the knowledge of the ram-pressure mechanism demonstrating that the gas-phase metallicity can trace the gas-stripping history.

Chapter 1

Introduction

The mechanisms which lead the formation and evolution of disk galaxies are still a topic of debate in the astronomic community.

Many models tend to built disk galaxies due to the accretion of material following the so-called inside-out scenario (Matteucci & Francois, 1989; Molla, Diaz, & Ferrini, 1996; Boissier & Prantzos, 1999).

The inside-out scenario results from the combination of the spherical collapse, due to dark matter, and the angular momentum redistribution into the gaseous material. When the dark matter virializes, the shocked gas is heated to the virial temperature. The cooling time in the inner regions is very short and part of the gas may quickly condense into cold lumps and forms bulge stars. Thus the gas is fast reprocessed, providing a population of old, metal-rich stars surrounded by a high-metallicity gaseous environment.

However, in the outer regions, higher virial temperatures and lower gas densities result in longer cooling times, so that as the gas cools and falls to its corresponding angular momentum radius, it can be shocked again and can form stars. Higher angular momentum material remains outside the bulge and forms the disk of younger, metal-poor stars from poorly enriched environment. Lower angular momentum material falls into the bulge, which continues to grow slowly but may be halted by energy input from a supernova and/or a massive black hole that can initiate a wind that blows out the gas (Kepner, 1999).

1.1 Gas metallicity in galaxies

The metals are the main products of stellar nucleosynthesis and when the enriched material is expelled during the star evolution, these products are mixed with the surrounding gas, which in turn can condense to form new stars. The study of abundance in interstellar medium (ISM) can provide important clues about

chemical evolution and help constraining the star formation history and gas flows in and out of galaxies. The distribution of gas abundance in galaxies is historically obtained from the analysis of strong nebular lines in discrete photoionized regions. These emission lines trace very well young, hot, massive stars, that illuminating and ionizing cubic kiloparsec-sized volumes (HII regions), indicate where star formation takes place (Osterbrock & Ferland, 2006).

Since oxygen is the most abundant heavy element in Universe, it's a common practice to describe the metallicity distribution by the abundance ratio O/H and the main abundance measure methods use its forbidden lines.

The classical technique is represented by the direct method that it's based on the measurement of the electron temperature T_e, derived from temperature-sensitive lines such as [OIII]λ4363/[OIII]λ5007, assuming a classical HII region model. T_e is converted in metallicity, taking into account the observed atomic specie ions and applying an ionization correction factors (ICFs) for the unobserved ions of the same atomic species (Peimbert & Costero, 1969). This method suffers from some issues: the [OIII]λ4363 line is very weak; electron temperature fluctuations in HII regions may cause metallicity underestimation; ICFs depend on all ionization and recombination processes, and not only on the ionization potential.

Starting from the samples of HII regions for which the T_e was directly measured by the ratio of the oxygen forbidden lines, the empirical metallicity methods were developed. The comparison between metallicity estimates by T_e measurements and strong emission line ratios has allowed to express empirical fits that can be applied to HII regions where the [OIII]λ4363 line is not observed (Díaz & Pérez-Montero, 2000; Pilyugin, 2001; Oey et al., 2002; Pettini & Pagel, 2004; Pilyugin & Thuan, 2005). This kind of calibrations is affected by the same issues of direct method. In addition, metallicity estimators resulting from empirical formulas based on different line ratios show discrepancies and offsets.

Other tools to estimate the gas chemical abundance from emission line measurements are theoretical methods (Pagel et al., 1979; McGaugh, 1991; Zaritsky, Kennicutt, & Huchra, 1994; Kewley & Dopita, 2002; Kobulnicky & Kewley, 2004). These calibrations adopt photoionization models, that describe the thermal balance at steps through a dusty spherical or plan parallel nebula, and stellar population synthesis models, that calculate the ionizing radiation field. Fixing metallicity and the ionization degree, the model can predict the theoretical emission line ratios. Thus, it's possible to build a theoretical grid on diagnostic diagrams which can be used to compute metallicity from observed emission line ratios. The choice of line ratios into diagnostic diagrams is important to get a good metallicity and ionization degree sensitivity and to avoid possible degeneracies, as it's highlighted in Dopita et al. (2013).

All uncertainties of this calibration are connected to the precision degree of models. These do not consider all necessary physics as they take some simplifications: the nebula geometry is usually assumed sphere-like or plane parallel; the eventual clumping of dust and gas is not taken into account; the atomic models are very simplified.

The abundance measurements by theoretical methods are systematically higher than other techniques (López-Sánchez et al., 2012). Moreover, a comparison of various calibrations has shown evident discrepancies in $12 + \log(O/H)$ with an offset up to 0.7 dex (Kewley & Ellison, 2008). Despite these differences, relative metallicity measurements remain reliable and the authors prefer to indicate the chemical abundance distribution in a sample.

Decades of studies about chemical abundance across the disks of spiral galaxies by measurement of emission lines in HII regions have shown the presence of negative radial abundance gradients, namely higher metallicity in the centre that decreases going outwards (Searle, 1971; Peimbert, Rayo, & Torres-Peimbert, 1978; Martin & Roy, 1992; Oey & Kennicutt, 1993; Zaritsky, Kennicutt, & Huchra, 1994; van Zee et al., 1998; Magrini et al., 2007; Gusev et al., 2012).

In order to find an explanation for the formation of this gradient, some chemical evolution models were proposed, as well as the classical closed box model. Goetz & Koeppen (1992) found that models adopting radial variation of star formation rate, gas flow and infall rate were able to reproduce the observed gradients, consistently with the inside-out scenario.

1.2 Integral field spectroscopic surveys

In order to refine the models it is necessary to obtain high quality spectroscopic data, which can provide an adequate statistics. However the reliability of these spectroscopic studies is directly connected to the individuation of suitable number of bright individual HII regions. From this point of view, the advent of recent integral field spectroscopy (IFS) technologies has allowed a huge step forward in this research field. The IFS techniques provide the opportunity to perform two-dimensional spatial studies on nearby galaxies and to acquire hundreds of spectra which cover most of the galaxy, from the centre to the outskirt, over a wide range of wavelengths.

A new generation of surveys performed with this technology is taking place. A first successful attempt was the PINGS (PPAK Integral Field Spectroscopy Nearby Galaxies Survey), that acquired a spectroscopic mosaicking of 17 nearby disk galaxies in the optical wavelength range (Rosales-Ortega et al., 2010). This project has shown the feasibility for the CALIFA (Calar Alto Legacy Integral Field Area; Sánchez et al. 2012a) survey.

CALIFA has obtained spatially resolved spectra from 3750 to 7000 Å for a sample of 600 local galaxies of all morphological types. Both PINGS and CALIFA have used the PPAK (Kelz et al., 2006) integral field unit (IFU) of the Potsdam Multi-Aperture Spectrograph (PMAS; Roth et al., 2005) instrument at the 3.5 m telescope of Centro Astronómico Hispano Alemán (CAHA) at Calar Alto (Spain). This IFU consists of 331 science fibres (2.7″ diameter each) covering a large hexagonal field-of-view of $74'' \times 64''$. The aim of these projects, especially CALIFA's, is to investigate the galaxy properties, such as age and metallicity of stellar populations, chemical abundance and distribution of ionized gas, star and gas kinematic. These integral field spectra, supplied by periodic data releases (Husemann et al., 2013; García-Benito et al., 2015; Sánchez et al., 2016) to the public, provide an important contribution to understand evolutionary processes which occur in galaxies: merging and secular mechanisms, environment effects, star formation history and AGN (Active Galaxy Nuclei) influence.

The demand to extend the research to a wider sample of galaxies has pressed the forth-generation SDSS (Sloan Digital Sky Survey) team to perform a new survey project, with the ambitious purpose to obtain integral field spectra of a sample of 10000 galaxies at low redshift: in 2014 the MaNGA survey (Mappings Nearby Galaxies at Apache Point Observatory; Bundy et al. 2015) have started. MaNGA makes use of an instrumental system consisting of the 2.5 m Sloan Telescope in its spectroscopic mode (Gunn et al., 2006), a set of 17 hexagonal fiber bundle IFUs (Drory et al., 2015) and the BOSS spectrographs covering a long, continuous wavelength range, from 3600 to 10300 Å with a resolution R $\sim$ 2000 (Smee et al., 2013). Also MaNGA aims to provide new insights in galaxy formation and evolution, and to be a starting point for current and future high-redshift studies.

CALIFA and MaNGA have already shown their potentiality for the galaxy chemical abundance study in recent works (Sánchez et al., 2014; Sánchez-Menguiano et al., 2016; Zinchenko et al., 2016; Pérez-Montero et al., 2016; Belfiore et al., 2017). The great advantage of the IFS technologies is the possibility to sample the galaxy from center to the outer radii with a large spatial resolution; this has allowed to measure accurate metallicity distributions of a large number of galaxies. Sánchez et al. (2014) find a common metallicity gradient when it is normalised to the effective radius of disk. Furthermore, they show outer flattening of abundance gradient beyond 2 r_e confirming previous argumentation of other authors (Bresolin et al., 2009; Marino et al., 2012), and inner metallicity drop in several galaxies. This study is extended in Sánchez-Menguiano et al. (2016), who analyze the dependence of the metallicity gradients on the morphology properties finding a relation between the presence of the bar or ring and the inner flattening. Belfiore et al. (2017) study the relation between the galaxy mass and the abundance slope and they argue for a steepening of metallicity gradient for

galaxies with $M_\star \sim 10^{10.5} M_\odot$ and find that the central flattening is more frequent in the most massive galaxies.

1.3 Gas removal processes

The spectroscopic studies are useful to infer the galaxy evolution from the metallicity and the kinematics. Sánchez et al. (2014) observe that galaxies subjected to mergers or interactions exhibit a clearly flatter chemical abundance distribution according to the results of Kewley et al. (2010) and Rich et al. (2012). Therefore, if on one side the metallicity distribution in galaxies can prove the theories of galaxy formation, on the other side it can testify ongoing dynamical processes extraneous to the inside-out scenario. The evolution of galaxies is due to internal and environment processes. Internal processes, such as galactic winds by star formation, stellar winds, supernova feedback or AGN activity, can drive the in and outflow of gas from galaxies (Veilleux, Cecil, & Bland-Hawthorn, 2005). Environment processes can affect the evolution by gravitational or hydrodynamical mechanisms. In a crowded environment, the cumulative effect of several weak and fast tidal encounters with the members of the cluster, the so-called harassment (Moore et al., 1996), or strong galaxy interactions and merges (Barnes & Hernquist, 1992) affect both the gas and stellar component. By the so-called strangulation (Larson, Tinsley, & Caldwell, 1980), hydrodynamical interactions between the galaxies and the intra-cluster medium (ICM) can remove the halo gas that is more loosely bound to the galaxy than the disk gas. Several mechanisms can instead remove the disk gas and leave intact the stellar component, such as the ram-pressure stripping (RPS) that is the pressure exerted by the intergalactic medium and the ICM (Gunn & Gott, 1972), thermal evaporation (Cowie & Songaila, 1977), and viscous stripping (Nulsen, 1982).

Multi-band observations are an important utility to resolve the physics both of gas and star to distinguish the dynamical processes occurring in the galaxy, for example to discern the ram-pressure stripping affecting only the gas, from tidal interactions that influence also the stellar component. There are many observations of ram-pressure phenomena: HI studies show the efficiency of stripping of the neutral gas (e.g., Haynes, Giovanelli, & Chincarini, 1984; Verdes-Montenegro et al., 2001); studies based on H_α imaging conclude that ionized gas is a excellent tracer of gas stripping in clusters (e.g., Gavazzi et al., 2002); the young stars often formed in the stripped gas can be identified from ultraviolet or blue images (e.g., Cortese et al., 2007); in recent years, systematical optical searches for gas-stripping candidates have been conducted (McPartland et al., 2016; Poggianti et al., 2016).

Integral field observations can be insightful to understand the impact of ram-pressure stripping on the evolution of galaxy properties, such as

metallicity, star formation, kinematics (Merluzzi et al., 2013; Fossati et al., 2016). Measurements of the velocity field of gas reveal that it is still dominated by the gravitational potential of the galaxy maintaining a coherent rotation with the stellar component, but the velocity dispersion shows many fluctuations, that increase in the outermost regions (Merluzzi et al., 2013; Fumagalli et al., 2014; Poggianti et al., 2017a; Bellhouse et al., 2017). Moreover, the current star formation rate is quenched in the regions where the gas is removed, instead the stripped gas is place of recent starbust following the collapse due to thermal instabilities and turbulent motions, therefore the star formation history results particular useful to derived the epoch of ram-pressure stripping.

Many studies of ram-pressure stripping are carried out comparing the observations with hydrodynamical models (Gullieuszik et al., 2017). These simulations require to estimate the ram-pressure intensity exerted by the cluster.

The strength of ram-pressure is proportional to the density of the intra-cluster medium and the square of the infall velocity of the galaxy (Gunn & Gott, 1972) and hydrodynamical simulations show that the gas removal efficiency is a function of the galaxy inclination with respect to the velocity direction (Abadi, Moore, & Bower, 1999; Vollmer et al., 2001).

The impact of the ram-pressure on the galaxy metallicity is still not very explored. Fossati et al. (2016), using spectroscopic MUSE data, find that the spatial variations of the chemical abundance in ESO137-001 galaxy are small and consistent with constant metallicity throughout the tail with an average value of 0.75 times the value assumed for the Solar metallicity.

The increasing of studies performed in the last years testifies the interest in the gas-removal processes, such as the ram-pressure stripping, and it requires to extend the number of observations. From this point of view, GASP (GAs Stripping Phenomena in galaxies with MUSE; Poggianti et al., 2017a, and following papers) is the only survey that addresses statistically the study of the ram-pressure stripping mechanism. The first results of GASP confirmed the stripped nature of the galaxies observed so far, showing spectacular evidence for ram-pressure stripping in action. The Multi Unit Spectroscopic Explorer (MUSE, Bacon et al., 2010) represents the ideal instrument to investigate the gas-removal processes in cluster galaxies.

MUSE is a second generation Very Large Telescope (VLT) panoramic integral field spectrograph. It has a field of view of 1" $\times$ 1", sampled at 0.2" $\times$ 0.2". The spectral range is $4650 - 9300$ Å with a spectral resolution of ~ 3000. MUSE couples the discovery potential of a large imaging device to the measuring capabilities of a high-quality spectrograph, while taking advantage of the increased spatial resolution provided by adaptive optics. Its performance is supported by an expected spectacular gain achieved in spatial resolution without any loss in

throughput and with almost full sky coverage. With its 400 megapixels per frame and 90000 spectra in one exposure, MUSE is already the largest integral field spectrograph ever built, and the only one that allows to achieve a very high level on the spatially resolved studies of the stellar population and gas properties.

1.4 Scope and structure of the thesis

This thesis takes maximum advantage of the potential provided by MUSE and aims to perform a spatially resolved study putting in relation the physical properties of the gaseous component, especially the metallicity of the ionized gas, with those of the stellar populations. Furthermore, this work probes the connection between gas metallicity and the local and global properties of galaxies subjected to ram-pressure stripping.

The thesis is organized as follows:

Chapter 1: This chapter presents an introduction about: the galaxy formation; the methods of analysis based on metallicity studies; the new generation of integral field spectroscopic surveys capable to improve the observations; the results on the metallicity distribution in disk galaxies by IFS data; the most important environmental processes, in particular the gas-removal mechanisms; the new studies aimed to investigate these phenomena.

Chapter 2: It introduces the GASP project and it describes its main scientific drivers and the galaxy sample observed with MUSE. Moreover, the procedures of reduction and elaboration of MUSE data are described.

Chapter 3: In this chapter, the two samples of galaxies, extracted from the GASP sample and analyzed in this work, are presented. A sample includes disk galaxies with no signs of morphological anomalies and it represents a control-sample, while the other collects the most spectacular cases of galaxies with gas removed by ram-pressure stripping, called jellyfish galaxies.

Chapter 4: The methods of analysis to derive the main quantities are described in this chapter. The code `pyqz` is used to estimate the gas metallicity. H_α-knots are identified and their properties are obtained. The structural parameters of the control-galaxies are estimated by a photometric and morphological analysis; finally, the structure of the main galaxy body of the gas-stripped galaxies is derived.

Chapter 5: This chapter presents the results obtained for the sample of the control-galaxies. The metallicity distributions are derived and the chemical abundance dependence on the global and local properties of the galaxy are discussed.

Chapter 6: The results achieved for the jellyfish galaxies are described in this chapter. The metallicity distribution in the main galaxy body and in the gas tails are presented. Then, the dependence of the metallicity on the properties

of the galaxy is investigated and compared with the results obtained for the control-galaxies.

Chapter 7: This last chapter presents a summary of this work, the main results and the future outlook.

Chapter 2

GASP project

GAs Stripping Phenomena (GASP) is a new integral field spectroscopy survey with MUSE that aims to study in detail the physical mechanisms involved in the gas removal processes from galaxies (Poggianti et al., 2017a,b; Bellhouse et al., 2017; Fritz et al., 2017; Gullieuszik et al., 2017; Moretti et al., 2018; Vulcani et al., 2017, 2018; Jaffe' et al., 2018). The goal of this project is to significantly improve the understanding of effects that can cause galaxies to only lose their gas. GASP is observing over 100 disk galaxies in the redshift range $z = 0.04 - 0.07$ from galaxy clusters to groups, poor groups and filaments. The targets of the survey are mainly galaxies presenting optical signatures of unilateral debris or disturbed morphology by gas-only removal processes, but galaxies devoid of such signatures are also included to constitute a control-sample.

The most striking examples of galaxies with unilateral gas debris are the so-called "jellyfish galaxies" that exhibit tentacles of material from the galaxy body, making the galaxy resemble a jellyfish (Ebeling, Stephenson, & Edge, 2014).

The key scientific drivers of GASP are:

- understand the efficiency of gas removal processes as a function of galaxy environment and galaxy mass;
- quantify the effects of ram-pressure stripping on the star-formation activity and galaxy quenching monitoring their evolution;
- investigate the connection between the gas physical conditions and the activity of the galaxy central black hole;
- analyze the kinematics and the dynamics of a galaxy during its motion through the intra-cluster medium;
- estimate the spatially resolved star formation hystory and metallicity distribution.

2.1 GASP sample and MUSE data

GASP primary targets were taken from the atlas of jellyfish candidates of Poggianti et al. (2016), who selected a large sample of galaxies with signatures of stripping from optical images of the WIde-field Nearby Galaxy-cluster Survey (WINGS; Fasano et al., 2006; Moretti et al., 2014), its extension OmegaWINGS (Gullieuszik et al., 2015; Moretti et al., 2017), and the Padova-Millennium Galaxy and Group Catalogue (PM2GC; Calvi, Poggianti, & Vulcani, 2011). The selection of the primary targets aims to include galaxies with tails or surrounding debris located on one side of galaxies, asymmetric or disturbed morphologies suggestive of unilateral external force and/or a distribution of star-forming regions on one side of galaxy. Since GASP focuses on gas-only removal processes, galaxies with evident tidal features or subjected to mergers were excluded.

Moreover, a control sample that includes galaxies in clusters and in the field with no optical sign of gas removal was selected in order to contrast the properties of stripping galaxies.

The GASP sample counts 114 disk galaxies (94 primary targets, 20 control-galaxies) that have a broad range of stellar mass ($10^{9.2} - 10^{11.5}$ $M_\odot$) and environment with dark matter halos of $10^{11} - 10^{15}$ $M_\odot$.

The observations are currently ongoing and carried out in service mode with the MUSE (Multi Unit Spectroscopic Explorer; Bacon et al., 2010) spectrograph mounted at the Nasmyth focus of the UT4 Very Large Telescope (VLT), at Cerro Paranal in Chile. MUSE is composed of 24 IFU modules equipped with a 4 k $\times$ 4 k CCD each. The spectra range between 4800 and 9300 Å with a resolution of $\sim$2.6 Å ($R = 1770$ at 4800 Å and 3590 at 9300 Å) and a sampling of 1.25 Å pixel^{-1}. The MUSE wide-field mode covers approximately a $1' \times 1'$ field of view with $0.2''$ per pixel, thus each datacube consists of approximately 90.000 spectra.

The combination of a large field of view and the sensitivity of MUSE at the GASP redshifts allows to observe galaxies out to large radii while maintaining a good spatially resolution.

The majority of GASP galaxies is observed with four exposures of 675 each, each rotated by 90° and slightly offset with respect to previous one to minimize the cosmetics. Some galaxies require two or three further offset pointings to cover the eventual long tails extended beyond the field of view. An internal illumination flat field is taken at the beginning and at the end of each 675 s exposure, in addition the spectroscopic standard stars are observed right after the science targets for the flux calibration. Daytime calibrations such as arcs, biases, darks, and flats are also taken.

2.2 Data reduction and analysis methods

This section presents the data reduction and the standard analysis performed for all galaxies. While in Chapter 4, a further and addressed method of analysis is developed for the sample of galaxies selected for this thesis and presented in Chapter 3.

The analysis in GASP adopts a standard concordance cosmology with $H_0 = 70\ \mathrm{km\,s^{-1}\,Mpc^{-1}}$, $\Omega_\mathrm{M} = 0.3$, and $\Omega_\Lambda = 0.7$ and a Chabrier (2003) Initial Mass Function (IMF).

The raw data are reduced using the latest version of the MUSE pipeline (Bacon et al., 2010), following the standard GASP reduction procedures described in Poggianti et al. (2017a). The data and the standard star frames are flat-fielded, corrected for differential atmospheric refraction, and wavelength-calibrated using arc lamp exposure. As the data have sufficient sky coverage, the sky is modelled directly and subtracted from individual frames using the 20% pixels with the lowest counts. The final flux-calibrated datacube is generated by lining up and combining the individual frames using the sources in the white-light images.

The reduced datacube is corrected for extinction due to our own Galaxy, using the extinction value estimated at the galaxy position (Schlafly & Finkbeiner, 2011) and assuming the extinction law from Cardelli, Clayton, & Mathis (1989).

The main emission lines in the spectrum are analyzed using the IDL publicly available software KUBEVIZ (Fossati et al., 2016). The available lines in the procedure are listed in Table 2.1. KUBEVIZ uses the MPFit (Markwardt, 2009) package to fit gaussian line profiles in order to derive the gas velocity, velocity dispersion and emission line fluxes of each spectra. The software uses combinations of 1D Gaussian functions to simultaneously fit a determined group of lines keeping the velocity separation of the lines fixed according to the line wavelengths. The flux ratios of the two [NII] and [OIII] lines are kept constant in the fit assuming the ratios given in Storey & Zeippen (2000). Before proceeding to the fits, the datacube is smoothed with a 5 pixel wide boxcar filter in the spatial direction. KUBEVIZ can also attempt a double component fit when the case requires it. The continuum is calculated between 80 and 200 Å redwards and bluewards of each line, omitting regions with other emission lines and using only values between the 40th and 60th percentiles.

The spatially resolved properties of the stellar populations were obtained using the spectral fitting code SINOPSIS (SImulatiNg OPtical Spectra wIth Stellar population models; Fritz et al., 2017). It is a spectrophotometric fitting code that reproduces the main features of galaxy spectra in the ultra–violet to near–infrared spectral range.

SINOPSIS searches the combination of Single Stellar Population (SSP) spectra that best fits both the average value of the observed spectrum flux in a pre–defined

set of spectral bands and the equivalent width values of the main lines in absorption and emission.

The code uses a new set of SSP models by S. Charlot & G. Bruzal (in preparation), which has higher spectral and age resolution than previous versions, and a larger number of metallicity values from $Z = 0.0001$ to $Z = 0.04$. This new models dataset includes the most recent version of the PADOVA evolutionary tracks from PARSEC (Bressan et al., 2012). Furthermore, SINOPSIS uses the SSP models including the effect of nebular gas emission.

Starting from a set of ~ 200 mono–metallicities SSP spectra with ages from 10^4 and 14×10^9 years, SINOPSIS bins the models with respect to the SSP's age, obtaining a new set of 12 theoretical spectra for any given metallicity value. Each spectrum is multiplied by a given stellar mass value according to a Chabrier (2003) IMF, reddened by selective extinction effect (Calzetti, Kinney, & Storchi-Bergmann, 1994), reshifted according to the observed redshifts of the gaseous and stellar components, finally it is compared with the observed spectrum.

As SINOPSIS produces the best-fit model cube, it provides the stellar-only model cube that is subtracted from the observed data cube to obtain an emission-only cube. In addition, SINOPSIS provides the spatially resolved estimates of the stellar population properties, such as the map of stellar mass.

KUBEVIZ is run on the emission-only cube to measure the emission-line fluxes and the associated errors corrected for stellar absorption. These fluxes are corrected for the dust internal extinction by the Balmer decrement at each spatial element location, assuming an intrinsic H_α/H_β ratio equal to 2.86 and adopting the Cardelli, Clayton, & Mathis (1989) extinction law.

Table 2.1: Emission lines fitted with KUBEVIZ for GASP.

line	λ (Å)	line	λ (Å)
H_β	4861.33	[NII]	6548.05
[OIII]	4958.91	H_α	6562.82
[OIII]	5006.84	[NII]	6583.45
[OI]	6300.30	[SII]	6716.44
[OI]	6363.78	[SII]	6730.81

Chapter 3

Galaxy sample

The galaxies analyzed in this thesis are selected from the GASP sample. In order to investigate the metallicity properties in normal and stripped galaxies, my works focuses on two galaxy sub-samples.

The first one collects the most spectacular cases of jellyfish galaxies with strong and evident gas debris and long tails of stripped material.

The second one is a control-sample that includes galaxies having neither sign of disturbed or lopsided morphology nor unilateral gas. A fundamental requirement is the presence of gas with strong emission lines, therefore eventual quenched galaxies are not considered. The control-sample includes both cluster galaxies and field galaxies. Moreover, some jellyfish candidates in the atlas of Poggianti et al. (2016) are inserted in this sample because an in-depth analysis of the gas hasn't shown sign of stripping or disturbed morphology.

The control-sample is studied in detail to fully test the methods of analysis described in Chapter 4, then these procedures are applied also to the jellyfish sample to compare the results of two samples.

The final sample consists of 10 control-galaxies and 12 jellyfish galaxies with stellar masses in the range $10^{10} - 10^{11.5}$ $M_{\odot}$. The Table 3.1 lists the location and the stellar mass of each target. Figures 3.1 and 3.2 show the H_{α} emission (corresponding to the ionized gas) over the continuum underlying H_{α} (approximating the stellar component) for each galaxy. In the control-galaxies (Figure 3.1) the emission of gas perfectly overlaps with the stellar continuum of the main galaxy body, while for the jellyfish galaxies (Figure 3.2) the H_{α} emission reveals the extraordinary structures produced by the ram-pressure stripping.

Table 3.1: Position and redshift of the galaxies analyzed in this work.

Control-Galaxies

galaxy	RA [h:m:s]	dec [d:m:s]	membership	redshift*	$\log(M_\star/M_\odot)$
A3376B0261	06 : 00 : 13.7	−39 : 34 : 49.2	A3376	0.0463	10.62
A3128B0148	03 : 27 : 31.1	−52 : 59 : 07.7	A3128	0.0603	9.99
A3266B0257	04 : 27 : 52.6	−60 : 54 : 11.6	A3266	0.0596	10.02
JO5	10 : 41 : 20.4	−08 : 53 : 45.6	A1069	0.0651	10.12
JO17	01 : 08 : 35.3	+01 : 56 : 37.0	A147	0.0447	10.06
JO68	21 : 56 : 22.0	−07 : 54 : 29.0	A2399	0.0577	10.06
P669	10 : 02 : 00.6	+00 : 10 : 44.3	field	0.0465	10.52
P21734	11 : 31 : 07.9	−00 : 08 : 07.9	field	0.0686	10.81
P25500	11 : 51 : 36.3	+00 : 00 : 01.9	field	0.0605	10.82
P45479	13 : 23 : 34.7	−00 : 07 : 51.7	field	0.0516	10.67

Jellyfish Galaxies

galaxy	RA [h:m:s]	dec [d:m:s]	membership	redshift*	$\log(M_\star/M_\odot)$
JO60	14 : 53 : 51.6	+18 : 39 : 06.4	A1991	0.0584	10.33
JO135	12 : 57 : 04.3	−30 : 22 : 30.3	A3530	0.0548	11.05
JO147	13 : 26 : 49.7	−31 : 23 : 45.5	A3558	0.0486	11.10
JO160	13 : 29 : 28.6	−31 : 39 : 25.3	A3558	0.0486	10.04
JO171	20 : 10 : 14.7	−56 : 38 : 30.6	A3667	0.0558	10.56
JO175	20 : 51 : 17.6	−52 : 49 : 21.8	A3716	0.0457	10.53
JO194	23 : 57 : 00.7	−34 : 40 : 50.1	A4059	0.0490	11.11
JO201	00 : 41 : 30.3	−09 : 15 : 45.9	A85	0.0559	10.65
JO204	10 : 13 : 46.8	−00 : 54 : 51.1	A957x	0.0451	10.74
JO206	21 : 13 : 47.4	+02 : 28 : 34.4	IIZW108	0.0486	10.89
JW39	13 : 04 : 07.7	+19 : 12 : 38.5	A1668	0.0634	11.22
JW100	23 : 36 : 25.1	+21 : 09 : 02.5	A2626	0.0548	11.47

* for the cluster galaxies, the redshift correspond to that of the cluster.

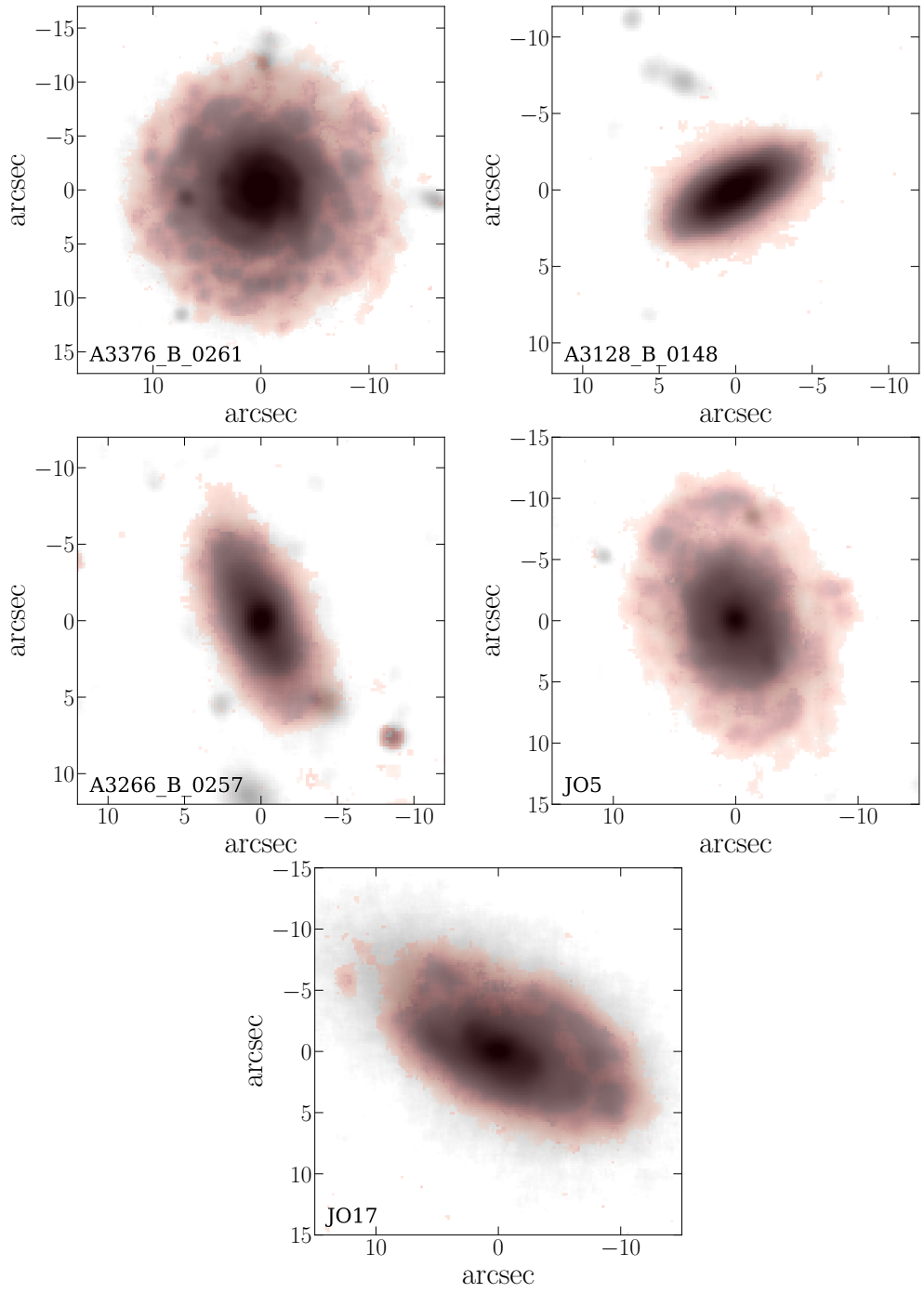

Figure 3.1: Galaxies of the control-sample. H_α emission (shaded pink area) is overlapped on the continuum underlying H_α image (shaded grey area). In these and all maps, (0,0) is the center of the galaxy. North is up and East is left.

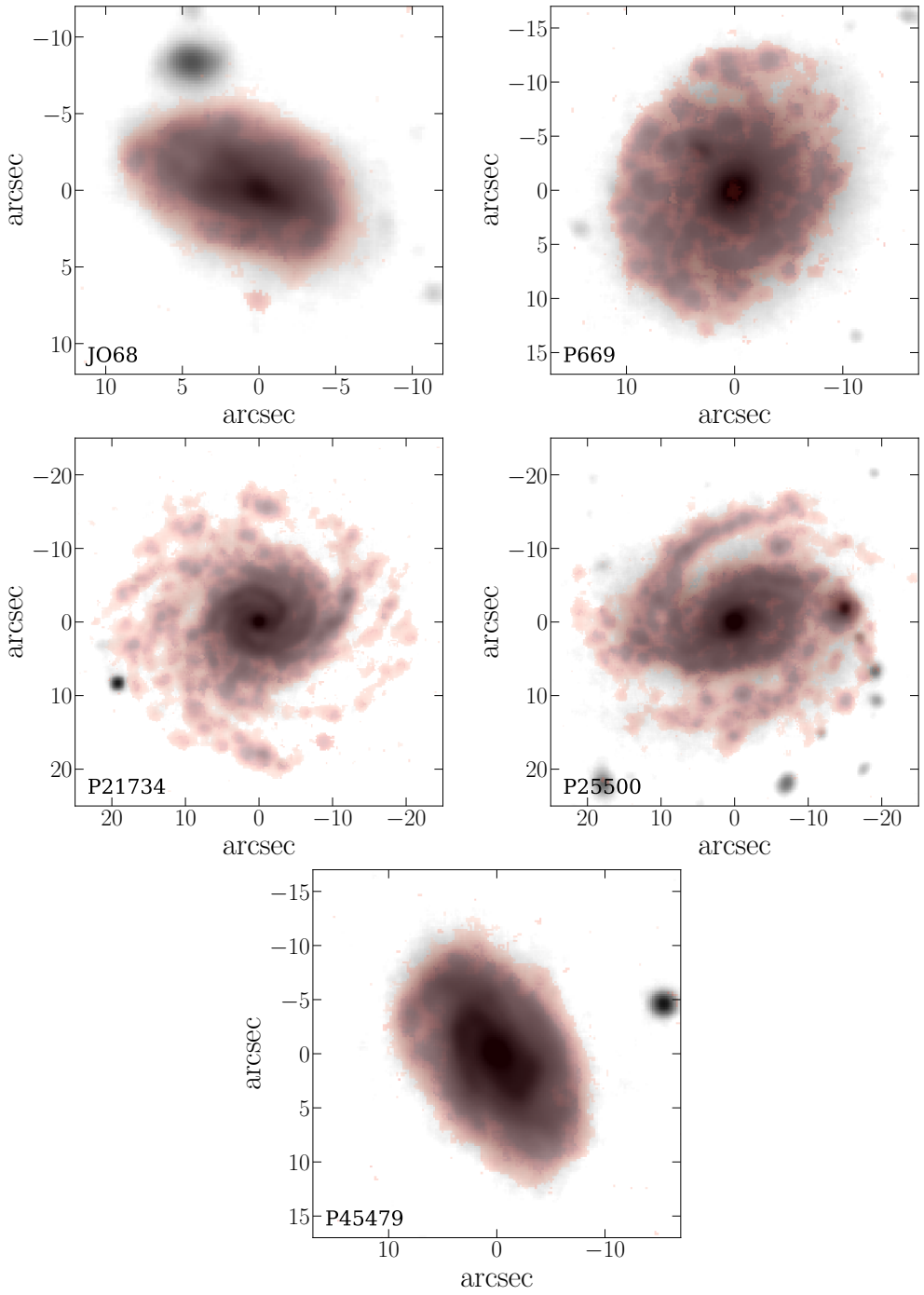

Figure 3.1: (*Continued*)

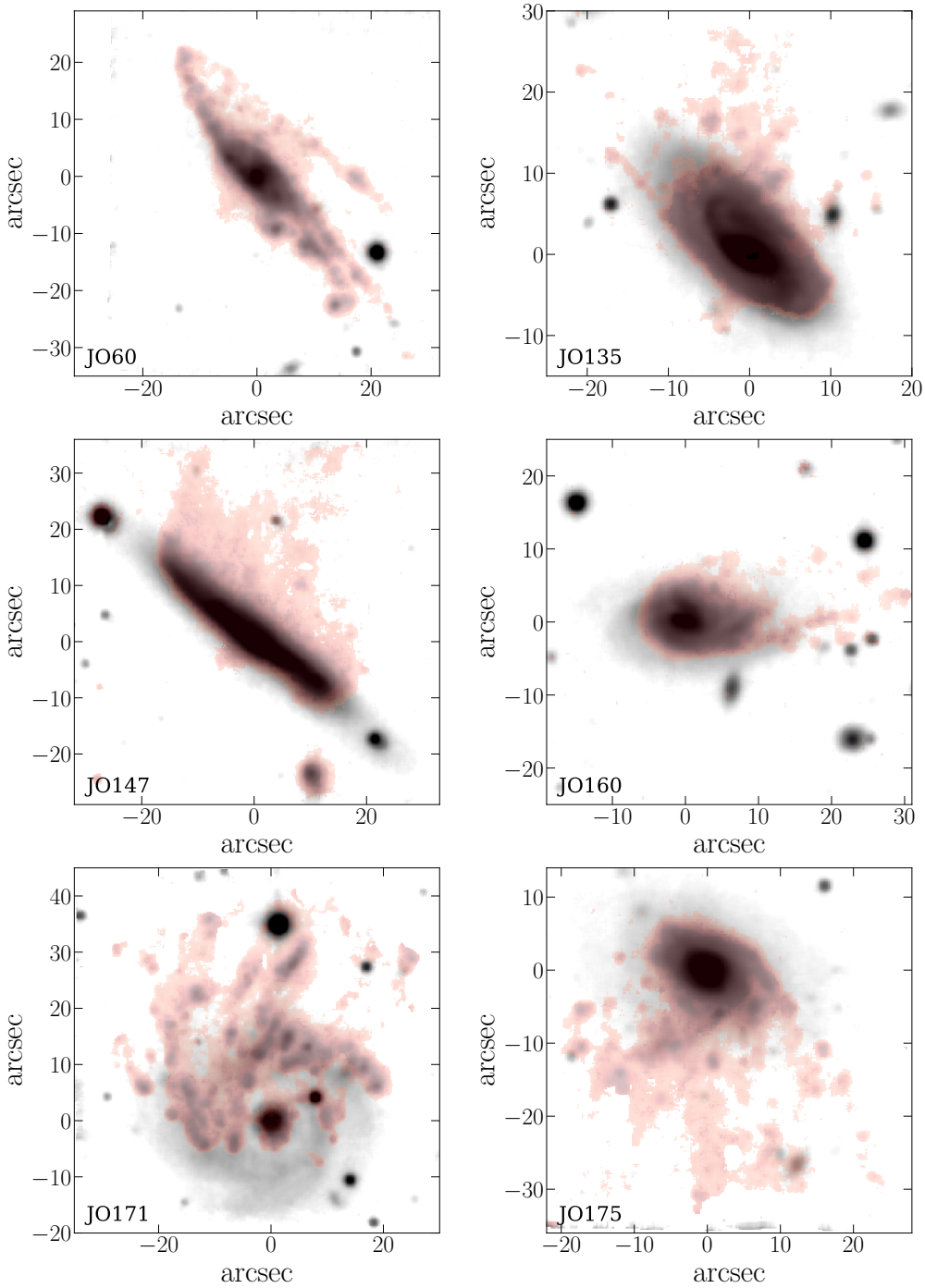

Figure 3.2: Galaxies of the jellyfish sample. H_α emission (shaded pink area) is overlapped on the continuum underlying H_α image (shaded grey area).

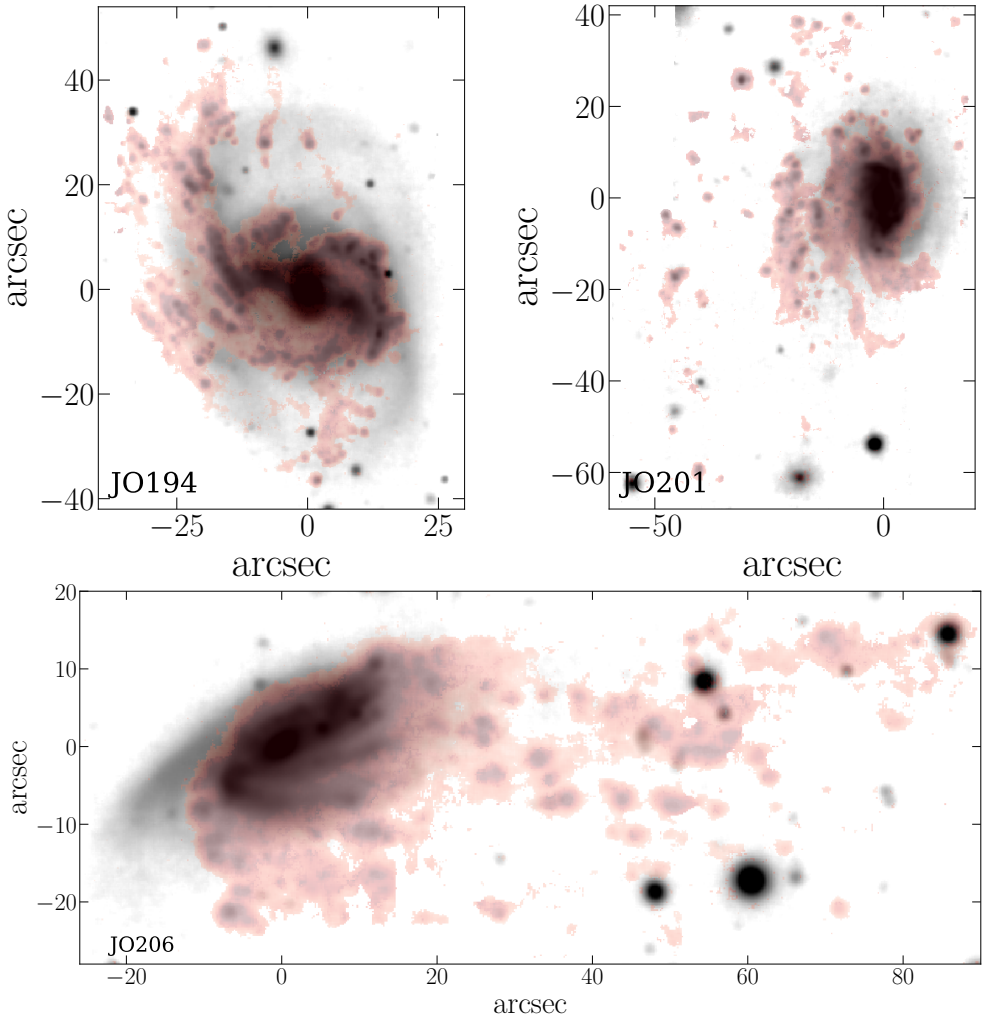

Figure 3.2: (*Continued*)

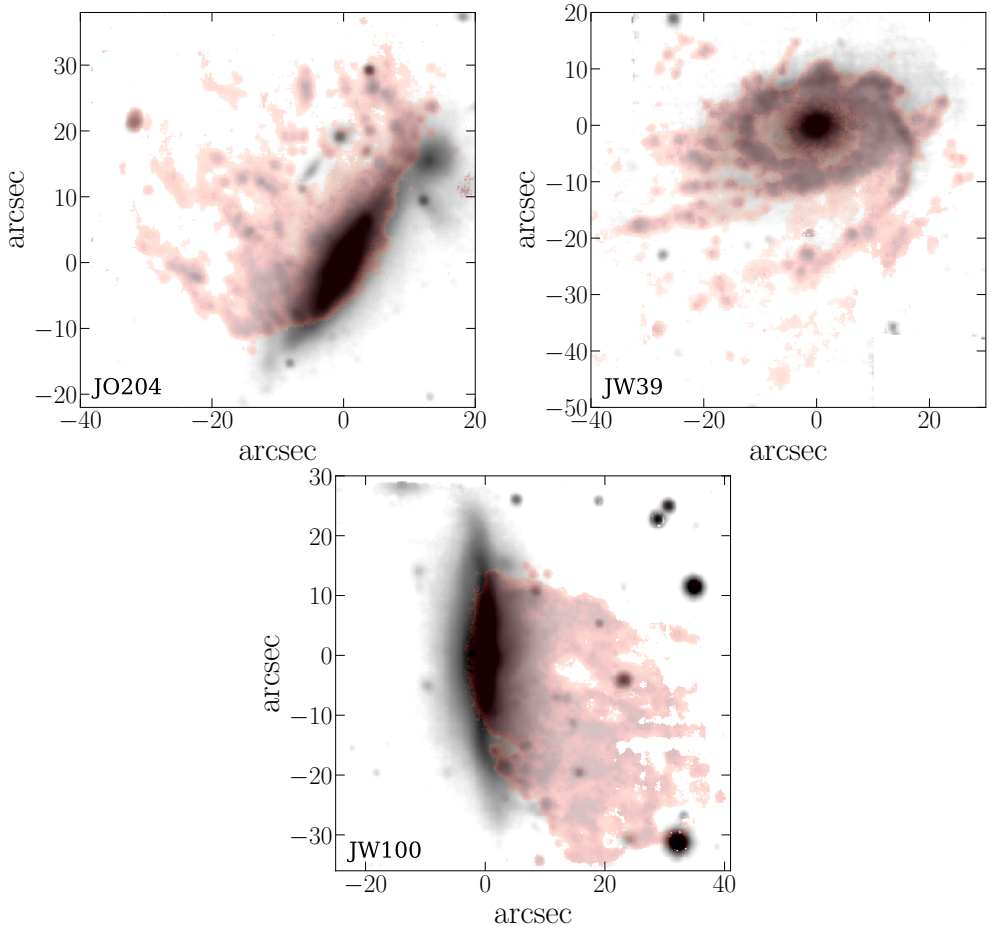

Figure 3.2: (*Continued*)

Chapter 4

Methods

The high quality spectroscopic data provided by MUSE allow to derive an enormous quantity of measurements about the properties of the gas and stellar components. The combination of KUBEVIZ and SINOPSIS, described in the Section 2.1, provides the emission line fluxes of gas and the stellar mass of each spatial element for the analyzed galaxies. The dust-absorption corrected fluxes can be used to estimate the gas metallicity, ongoing star-forming rate, ionized gas mass and involved ionization mechanism.

In this chapter, the Section 4.1 presents the technique of metallicity estimation performed by the `pyqz` code; in Section 4.2 a procedure to identify the H_α regions is explained and the properties of these knots are derived; the ionization mechanisms which power these regions are investigated by diagnostic diagrams in Section 4.3; the total stellar mass of the galaxies is computed in Section 4.4; the Section 4.5 illustrates the procedure to estimate the structural parameters of the control-sample galaxies, while in Section 4.6 a technique to draw the main body boundaries of jellyfish galaxies and their inclination and position angle is described; finally, the equations to deproject the galactocentric distances are shown in Section 4.7.

All quantities derived in this chapter are used to study the global and local relations between the gas-phase metallicity and the properties of galaxy, which are discussed in the next chapters.

4.1 Metallicity measurement by `pyqz`

The choice of the technique to measure the gas-phase metallicity is connected to the available spectroscopic data. The spectra provided by MUSE cover a wavelength range between 4800 and 9300 Å.

The methods for the measurement of the ionized gas metallicity by emission

lines can be divided in three categories: direct method, empirical calibration and theoretical calibration.

The direct method is based on the measurement of the gas electron temperature T_e from the ratio between the auroral line [OIII]λ4363 and a lower excitation line such as [OIII]λ5007. Then, T_e is converted in metallicity correcting for the stages of ionization. This method suffers of several issues, such as the weakness of the line [OIII]λ4363 and the underestimation of electron temperature due to temperature fluctuations (Peimbert & Costero, 1969; Stasińska, 2002, 2005), in addition the MUSE spectral range doesn't include the line [OIII]λ4363.

The empirical methods are developed by fitting the relationship between accurate measurements of metallicity based on the direct method and the strong-line ratios in HII regions (Díaz & Pérez-Montero, 2000; Pilyugin, 2001; Oey et al., 2002; Pettini & Pagel, 2004; Pilyugin & Thuan, 2005). Their advantage is the simple use, but they often suffer of a large scatter around the relation that is cause of uncertainties.

The theoretical methods are based on photodissociation models (Pagel et al., 1979; McGaugh, 1991; Zaritsky, Kennicutt, & Huchra, 1994; Kewley & Dopita, 2002; Kobulnicky & Kewley, 2004). The enormous advantage of these calibrators is the availability of a wide set of predicted emission lines from various input gas metallicities and different stages of ionization. Although these methods are limited by the assumptions and simplifications at the base of the models, they are powerful tools to obtain a consistent measurement of metallicity.

Theoretical and empirical calibrations often don't consider the uncertainty on the derived strong line abundances in those cases where the ionization parameter is not explicitly solved as a separate variable. Although many bright HII regions present similar ionization degrees, the observed scatter of ionization parameter introduces significant errors into the abundances estimates.

In this thesis the gas metallicity is estimated using the `pyqz` code (Dopita et al., 2013) version 0.8.2. This theoretical calibrator is a Python module able to simultaneously compute the values of the ionization parameter ($\log q$) and chemical abundance ($12 + \log(\mathrm{O/H})$) for a given set of strong emission line fluxes. These quantities are measured interpolating a set of diagnostic line-ratio grids computed with the MAPPINGS code (Sutherland & Dopita, 1993; Groves, Dopita, & Sutherland, 2004, 2006; Allen et al., 2008). MAPPINGS is a general purpose astrophysical plasma modelling code. It is principally intended to calculate the thermal balance through a dusty spherical or plane parallel nebula and to predict the emission line spectra of HII regions with different levels of photoionization.

The MAPPINGS V grids in `pyqz` version 0.8.2 cover a limited range of abundances ($8.11 \leq 12 + \log(\mathrm{O/H}) \leq 8.985$); therefore the `pyqz` code employed for the GASP project is a modified version that implements the MAPPINGS IV

grids tested in the range $7.39 \leq 12 + \log(\mathrm{O/H}) \leq 9.39$ (F. Vogt, private communication; see Poggianti et al. 2017a).

The diagnostic grids used by `pyqz` are chosen to be flat, without wraps, to decouple the influence of $\log q$ and $12 + \log(\mathrm{O/H})$ on the emission line ratios. In the spectral range of MUSE, the available emission lines allow to use the calibratios based on [OIII]/[SII] *vs.* [NII]/[SII] and [OIII]/H_β *vs.* [NII]/[SII] (in detail [OIII]λ5007, [NII]λ6583, [SII]λ6716 + 6731), which provide an excellent discrimination between $12 + \log(\mathrm{O/H})$ and $\log q$, as highlighted by Dopita et al. (2013).

The core of the module `pyqz` is its routine enveloped to interpolate a given pair of observed line ratios between the nodes of the respective MAPPINGS model grid. This function perform a two-dimensional fit and returns the corresponding values of chemical abundance and ionization parameter.

The `pyqz` code provides four possible modes to measure:

SINGLE DIRECT ESTIMATION: this mode returns the most straightforward measurements computed by the basic function of `pyqz` for a given diagnostic diagram. These estimates haven't associated errors.

GLOBAL DIRECT ESTIMATION: its estimates are the mean of the individual direct estimates for a given set of diagnostic grids. Since all line ratio diagnostic grids are constructed from the same set of MAPPINGS simulations, the direct estimates from different grids are likely consistent. This function allows to provide values with the associated standard deviations.

SINGLE KERNEL DENSITY ESTIMATION (KDE): this function takes the errors associated with the line fluxes into account. A given (by user) number of line flux values are generated in such way to sample a given (by user) probability density function. Each pseudo-set of line fluxes is used to compute the direct estimates for a given diagnostic grid. From the distribution of these estimates, the peak value and the error within the 61th percentile are derived.

GLOBAL KDE: the estimates are the mean of the single KDE estimates for a set of diagnostic grids.

In this work, the measurements of the metallicity and ionization parameter are computed with the `pyqz` single KDE using the [OIII]/[SII] *vs.* [NII]/[SII] grid. This grid is slightly more sensitive at high ionization than the [OIII]/H_β *vs.* [NII]/[SII] grid. However this latter is used to compare and to check the consistency of results.

The task is set to derive the quantities from a set of 1000 simulated fluxes distributed like a gaussian function and assuming a plane parallel geometry for

the emitted nebulae. Only the spatial elements with S/N $\geq$ 3 for all involved emission lines are considered.

4.2 Identification of the star-forming knots and knot properties

The galaxies in the sample present bright knots, characterized by strong emission lines often associated to star-forming processes. These regions have a high S/N ratio, therefore they represent the ideal targets for a focused analysis.

The identification of these knots are achieved by a purposely devised shell script that includes IRAF and FORTRAN calls developed and implemented by G. Fasano (private communication), described in detail in Poggianti et al. (2017a). The knots are assumed circular and their center are detected as local minima in the laplace+median filtered H_α image derived from the MUSE data cube.

The extent of each knot is estimated by an iterative procedure in which the radius of knots is increased of one pixel at a time. The iteration proceeds until at least one of following circumstances occurs for the outermost shell:

a) the counts of at least one pixel exceed those of the central pixel;

b) the fraction of the pixels with counts greater than the average counts of the preceding shell exceeds one third;

c) the average counts of pixel with counts below the aforementioned threshold are lower than a level set for the diffuse emission;

d) the image edge is reached by at least one pixel.

The emission line integrated fluxes of each knots are derived from emission-only datacubes running KUBEVIZ on the circular masks identifying the knots. These fluxes are corrected for dust extinction (as described in Section 2.2) and then used to derive the gas metallicities and the ionization parameters with associated errors by `pyqz` (as described in previous section), diagnostic diagrams (Section 4.3), the stellar and gas masses and the star formation rates.

The stellar mass of each knot is obtained integrating over the knot masks the spatially resolved stellar mass map of each galaxy returned from SINOPSIS.

The star formation rate (SFR) is computed from the integrating H_α luminosity adopting the Kennicutt (1998)'s relation

$$\mathrm{SFR} = 4.6 \times 10^{-42} L_{\mathrm{H}\alpha} \tag{4.1}$$

where SFR is in solar masses per year and the H_α luminosity is in erg per sec using a Chabrier IMF.

The gas mass is computed as the mass of the hydrogen atom ($m_{\rm H}$) times the number of hydrogen atoms ($N_{\rm H}$). This latter reasonably corresponds to the number of protons ($N_{\rm p}$) that is equal to the proton density ($n_{\rm p}$) times the volume (V) times the filling factor (f). In fully ionized gas the electron density is assumed equal to proton density ($n_{\rm e} = n_{\rm p} = n$) (Boselli et al., 2016; Fossati et al., 2016), therefore the number of protons can be estimated by equation 13.7 in Osterbrock & Ferland (2006)

$$L_{\rm H\alpha} = n_{\rm e}\, n_{\rm p}\, V\, f\, \alpha_{\rm H\alpha}\, h\, \nu_{\rm H\alpha} = n\, N_{\rm p}\, \alpha_{\rm H\alpha}\, h\, \nu_{\rm H\alpha} \tag{4.2}$$

where $\alpha_{\rm H\alpha}$ is the effective $\rm H_\alpha$ recombination coefficient and $h\,\nu_{\rm H\alpha}$ is the energy of the $\rm H_\alpha$ photon for case B recombination. Therefore the gas mass can be estimated as

$$M_{\rm gas} = N_{\rm p} \times m_{\rm H} = \frac{L_{\rm H\alpha} \times m_{\rm H}}{n\, \alpha_{\rm H\alpha}\, h\, \nu_{\rm H\alpha}}. \tag{4.3}$$

The density n is derived from the ratio $R = $ [SII]λ6716/[SII]λ6731, using the calibration of Proxauf, Öttl, & Kimeswenger (2014) valid in the range $R = 0.4 - 1.435$.

4.3 Diagnostic diagrams

The methods applied for the correction of the intrinsic dust absorption and to the measurements of gas metallicity, ionization parameter, star formation rate and gas mass are valid only for the spectra of gas elements powered by stellar photoionization sources. To prevent contamination of the results, the data coming from regions subjected by AGNs or LINERs (Low-Ionization Nuclear Emission-line Regions) must be removed.

The diagnostic diagrams are an important tool to this aim. They were initially proposed to identify the active galaxies (Heckman, 1980; Baldwin, Phillips, & Terlevich, 1981; Ho, Filippenko, & Sargent, 1997) and subsequently to classify the ionization mechanisms which are responsible of the observed emission lines.

The diagnostic diagrams are based on the comparison between observed line ratios with those expected by theoretical models of stellar population synthesis and photoionization (Kewley et al., 2001) or with those already observed from HII regions and galactic nuclei (Kewley et al., 2006).

In this thesis, the classification of the knots is achieved by the line ratios [OIII]λ5007/$\rm H_\beta$ *vs.* [NII]λ6583/$\rm H_\alpha$ diagram providing a separation in four categories: star-forming systems, AGNs, LINERs and composite regions, which are powered by a combination of photoionization and AGNs/LINERs.

Analytically, the different categories are divided using the following equations:

$$\log([\mathrm{O\,III}]/\mathrm{H}_\beta) = \frac{0.61}{\log([\mathrm{N\,II}]/\mathrm{H}_\alpha) - 0.05} + 1.30 \tag{4.4}$$

$$\log([\mathrm{O\,III}]/\mathrm{H}_\beta) = \frac{0.61}{\log([\mathrm{N\,II}]/\mathrm{H}_\alpha) - 0.47} + 1.19 \tag{4.5}$$

$$\log([\mathrm{O\,III}]/\mathrm{H}_\beta) = 1.79\ \log([\mathrm{N\,II}]/\mathrm{H}_\alpha) + 0.33 \tag{4.6}$$

derived respectively from Kauffmann et al. (2003), Kewley et al. (2001), Sharp & Bland-Hawthorn (2010). The star-forming systems are located below Eq. 4.4; the composite regions are between Eq.s 4.4 and 4.5; the AGNs are defined above Eq.s 4.5 and 4.6; while the LINERs are located above Eq. 4.5 and below Eq. 4.6.

Figure 4.1 shows the diagnostic diagrams (left panels) for the knots of the galaxies A3376B0261 (control-sample) and JO135 (jellyfish sample). The right panels illustrate the spatial distribution of the knots and their ionization sources. A3376B0261 presents no knots powered by AGN or LINERs, as the entire sample of control-galaxies, while JO135 is characterized by some regions affected by AGNs and LINERs in the center and in the tails. The diagnostic diagrams of all galaxies are in Figure A.1 in Appendix.

The same diagnostic checks can be also performed spaxel by spaxel. In this case the analysis is limited only to those spaxels that present a high S/N ratio (usually S/N ≥ 3) for all involved emission line fluxes.

All knots and spaxels for which the emission is not due to photoionization or composite sources are removed from the study.

4.4 Total stellar mass

The stellar mass of the galaxies is derived by SINOPSIS from the integrated spectrum of the galaxy main body, as described in Poggianti et al. (2017a). The continuum underlying H_α image is sliced in different count levels. The isophote enclosing the spaxels with surface brightness $\sim 1\,\sigma$ above the background level, is assumed to represent the galaxy main body. The galaxy spectrum is integrated within this isophote and the SINOPSIS is run on this integrated spectrum to derive the global stellar mass.

The total stellar mass of the control-galaxies and jellyfish galaxies are reported in Tables 4.1 and 4.2 respectively.

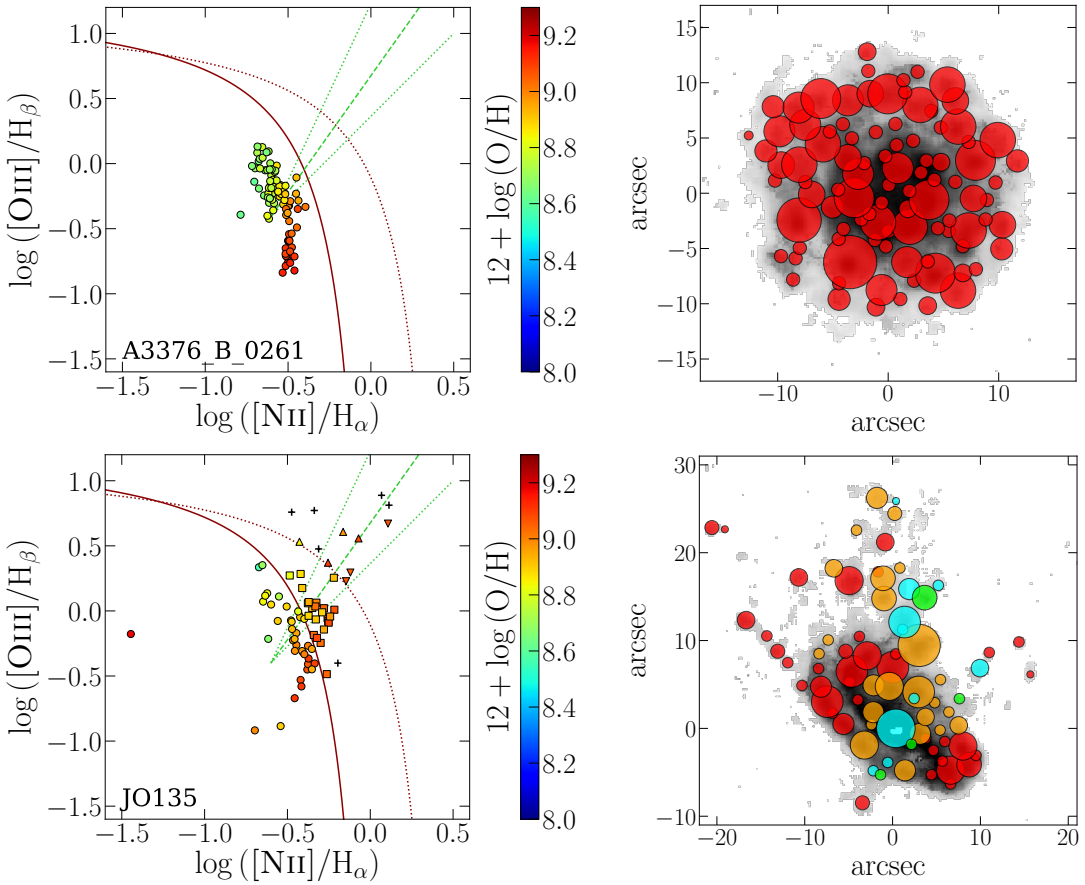

Figure 4.1: *Left*: Diagnostic diagrams for the control-galaxy A3376B0261 (*top*) and jellyfish galaxy JO135 (*bottom*). The lines correspond to the Eq. 4.4 (*solid red*), Eq. 4.5 (*dotted red*) and Eq. 4.6 (*dashed green*). The dots indicate the knots powered by stellar photoionization (*circle*), composite source (*square*), AGN (*triangle up*) or LINER (*triangle down*). The color-code indicate the metallicity of the knot. The crosses indicate the knots without metallicity estimate. *Right*: Distribution of the knots in A3376B0261 and JO135. The colors correspond to ionization mechanisms of stellar photoionization (*red*), composite source (*orange*), AGN (*cyan*), LINER (*green*). The dimension of each knot corresponds to the radius estimated in Section 4.2. The grey shaded area represents the H_α image. In these and all maps, (0,0) is the center of the galaxy.

4.5 Structural parameters by photometric analysis

To estimate the metallicity gradients of control-sample galaxies, I performed a surface brightness and morphological analysis to derive the mean position angle, inclination and effective radius of the disk for each control-sample galaxy. With this information I will deproject and rescale the position of each spaxel and knot.

The first step consists in the extraction of surface brightness profile (SBP) of each galaxy by an isophotal analysis of the *g*-band images. These images are produced integrating the MUSE datacube over the *g*-band of the Sloan Digital Sky Survey (SDSS).

The galaxy isophotes are fitted using the `ellipse` tool included in IRAF (Jedrzejewski, 1987). This task allows to perform an elliptical segmentation of the surface brightness starting from a guess intermediate isophote defined by a custom set of initial parameters. This set has to include the approximate values of center coordinates (x_c, y_c) in the image, semi-major axis length (a) in pixel units, ellipticity (e) and position angle (PA) measured anti-clockwise from North direction. The task fits the isophotes starting from the guess ellipse outward, then from the guess ellipse inward. Each ellipse fitted to the isophotes is determined by a definite semi-major axis length.

In general, the isophotes aren't perfectly elliptical, so the algorithm works out a minimization of deviations from the perfect ellipse shape.

In this analysis the fitting procedure is regulated by the following setting:

i) the center coordinates (x_c, y_c) are re-measured;

ii) the center of each fitted isophote is kept fixed at the new center position;

iii) the position angle and the ellipticity of each ellipse are unconstrained;

iv) the semi-major axis update is set to geometric growing mode with step = 0.1. So the semi-major axis length of each next ellipse is increased by a factor of 1.1.

The setting *iv*) yields a closer sampling of the inner region of galaxy, where the surface brightness is due to the bulge.

Before proceeding to the elliptical segmentation, all extragalactic sources and the galactic regions not due to the bulge or disk are masked out. This forethought is important for the second step, because the surface brightness of arms can have repercussions on the estimates of the effective radius and so on the metallicity gradients. In particular, the presence of the arms in the SBP tends to underestimate the effective radius and to produce slopes less steep on the metallicity profile expressed in r_e units.

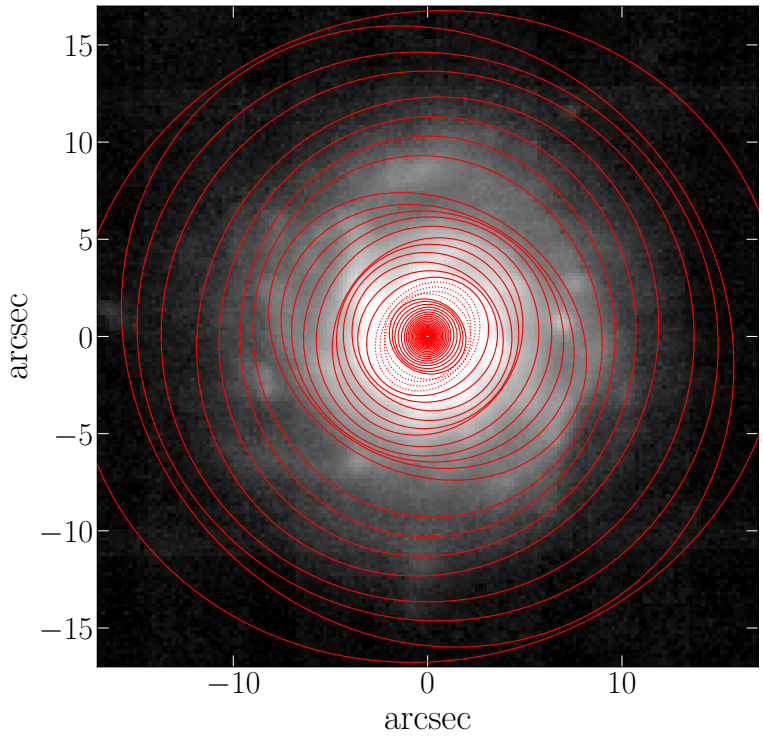

Figure 4.2: Elliptical segmentation of surface brightness performed by `ellipse` on the g-band image of control-galaxy A3376B0261. The dotted ellipses indicate the invalid isophotes.

During the procedure `ellipse` builds up a series of concentric elliptical isophotes and at the end, it provides a table that includes the semi-major axis length, the area, the luminosity intensity integrated into the area, the ellipticity, the position angle, the Fourier coefficients which summarize the deviations from perfect ellipticity and a stop-condition code that describes the success of the minimization procedure convergency for each isophote.

Figure 4.2 illustrates an example of the elliptical segmentation obtained for the control-galaxy A3376B0261.

The second step consists in the morphological analysis based on the profile of the surface brightness averaged over the isophotes in order to derived the effective radius of the disk, the mean ellipticity and the position angle.

The disk surface brightness is classically described by the exponential law

$$I(r) = I_0 \, \mathrm{e}^{-\frac{r}{r_\mathrm{d}}} \tag{4.7}$$

where I_0 is the central intensity and r_d is the disk scalelength (Freeman, 1970). This formula is equivalent to the Sérsic law (Sérsic, 1968) setting the Sérsic index (n) equal to 1

$$I(r) = I_\mathrm{e} \, \mathrm{e}^{b_n[(r/r_\mathrm{e})^{1/n}-1]} \tag{4.8}$$

where $r_{\rm e}$ is the effective radius, $I_{\rm e}$ is the intensity at $r = r_{\rm e}$ and b_n is a function of n.

In this way the effective radius in the Sérsic law corresponds to the effective radius of the disk, defined as the radius that includes half of the total integrated flux of the disk component, and it is proportional to the disk scalelength by the relation

$$r_{\rm e} = 1.67835\, r_{\rm d}. \tag{4.9}$$

In many cases, the presence of the bulge prevents to directly fit the entire SBP with the exponential law. For this reason the disk effective radius is derived by an iterative procedure similar to that carried out in Sánchez et al. (2014).

First, the isophotes for which `ellipse` has failed the convergency are excluded, then the SBP expressed in magnitude units is fitted with a linear regression.

As in Sánchez et al. (2014), in each stage of iteration the brightest value of the SBP is removed and a new linear fit is computed. The iteration stops when a quarter of the original values remains in the surface brightness profile.

From the series of linear regressions (one for iteration), the linear fit with the best Pearson correlation coefficient is put equal at the exponential law expressed in magnitude units,

$$\mu(r) = \mu_0 + 1.086 \left(\frac{r}{r_{\rm d}}\right) = \mu_0 + m\, r \quad \Longrightarrow \quad r_{\rm d} = \frac{1.086}{m}, \tag{4.10}$$

in this way the disk scalelength is inversely proportional to the angular coefficient (m) of the linear equation. Finally, the disk effective radius is obtained using the relation 4.9.

The parameters of isophotes that present the best correlation between surface brightness and semi-major axis length are used to estimate the ellipticity and position angle averages of the disk.

The surface brightness, ellipticity and position angle profiles of each control-sample galaxy are shown in Figure A.2 in Appendix.

Assuming an intrinsic ellipticity for galaxies of $q = 0.13$ (Giovanelli et al., 1995), the inclination of disk is derived by equation

$$\cos^2 i = \frac{(1-\varepsilon)^2 - q^2}{1 - q^2} \tag{4.11}$$

where ε is the mean ellipticity of disk.

Another parameter that can be derived by a different photometric analysis is the radius r_{25}, defined as the semi-major axis length of the elliptical isophote with surface brightness in B-band $\mu_B = 25$ mag arcsec^{-2}. The estimation of this quantity is performed by G. Fasano (private communication) using the B-band images of the surveys WINGS, OMEGAWINGS and PMC2GC. Knowing

the zero-point magnitude of each image, the value c_{25} of the counts per pixel corresponding to the surface brightness $\mu_B = 25$ mag arcsec^{-2} is computed. The images are smoothed with a two-dimensional gaussian filter ($\sigma = 1 \times 1$) and then, they are slicing at the count level c_{25}. In this way, the isophote results more definite allowing to measure the lengths of its major and minor axes.

Table 4.1 collects the parameter values for each control-sample galaxy.

4.6 Definition of the main galaxy body

Jellyfish galaxies are characterized by a disturbed morphology that prevents to perform the same photometric analysis carried out for the control-sample galaxies. In the cluster environment, the action of the ram-pressure stripping produces unilateral debris and long tails of gas from galaxy body with stars forming in situ. These tails are likely extended along the opposite direction of the velocity vector of galaxy. Therefore, the stripped gas is usually extraplanar with respect to the galactic plane.

To estimate the metallicity gradients of jellyfish galaxies, there are several cautions to be taken. It's necessary to distinguish the knots belonging to the galaxy main body and those belonging to tails and to define what "main body" is (M. Gullieuszik et al., in preparation).

The procedure uses the map of the continuum underlying H_α, because it represents a good proxy of the distribution of the stellar component. The starting point is the isophote corresponding to $1\,\sigma$ above the background surface brightness. After masking out all contaminating sources, an ellipse is fitted to the isophote on the undisturbed side of the galaxy. From the disturbed side, all regions beyond the ellipse are excluded to symmetrise the shape of the galaxy main body.

Figure 4.3 offers a clear example of the main body boundary drawn from the jellyfish galaxy JO206.

The position angle and ellipticity of the ellipse are considered representative of the structural parameter of the disk and used to derived the inclination (Eq. 4.11) of the galactic plane and to deproject the position of knots inside the boundary of the galaxy body. The position angle PA and inclination i of each jellyfish galaxy are reported in Table 4.2.

4.7 Deprojection of the galactocentric distances

The position angle PA and inclination i of the control-sample galaxies (see Section 4.5) and jellyfish galaxies (see Section 4.6) are listed in Tables 4.1 and 4.2, respectively.

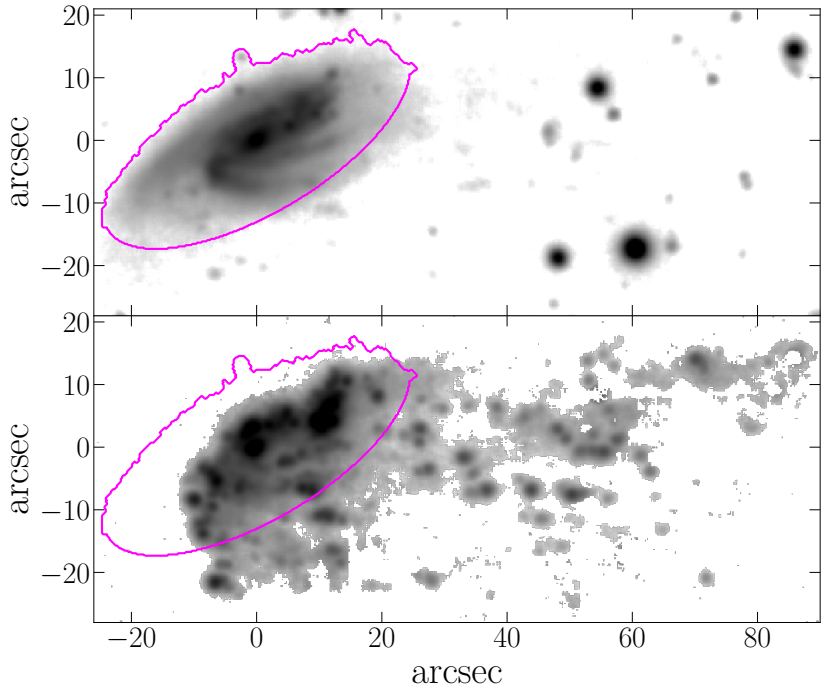

Figure 4.3: Continuum underlying H_α (*top panel*) and H_α (*bottom panel*) images of jellyfish galaxy JO206. The magenta line indicates the main body boundary.

These quantities allow to deproject the position of each spaxel and knot from the sky plane to the galaxy disk plane, and to derive the galactocentric distances. The center of each galaxy is defined on the map of the continuum underlying H_α.

At first, the coordinates (x, y) of the image are reported in the reference system centered in the galaxy center (x_0, y_0) and rotated as much as the position angle by the equations

$$\begin{cases} x' = (x - x_0)\sin PA - (y - y_0)\cos PA \\ y' = (y - y_0)\sin PA + (x - x_0)\cos PA \end{cases} . \tag{4.12}$$

Finally, the positions are deprojected and the galactocentric distances are measured by

$$d^2 = x'^2 + \left(\frac{y'}{\cos i}\right)^2 . \tag{4.13}$$

Table 4.1: Structural parameters and total stellar mass of the control-sample galaxies.

galaxy	r_e[a] [arcsec]	r_{25} [arcsec]	ε	i	PA^*	$\log(M_\star/M_\odot)$
A3376B0261	5.53	11.97	0.06	20.3°	118.5°	10.62
A3128B0148	1.97	8.99	0.56	65.0°	119.2°	9.99
A3266B0257	3.23	4.62	0.59	66.8°	23.0°	10.02
JO5	4.52	15.17	0.27	43.4°	29.7°	10.12
JO17	7.41	9.50	0.47	59.0°	69.2°	10.06
JO68	4.21	7.09	0.46	58.2°	68.3°	10.06
P669	7.12	23.51	0.17	34.4°	145.6°	10.52
P21734	8.83	22.65	0.17	34.4°	95.6°	10.82
P25500	10.46	30.09	0.29	45.0°	114.3°	10.81
P45479	6.01	17.94	0.28	44.4°	33.8°	10.67

* anti-clockwise from North direction

Table 4.2: Inclination, position angle and total stellar mass of the jellyfish galaxies.

galaxy	i	PA^*	$\log(M_\star/M_\odot)$
JO60	77.4°	37.1°	10.33
JO135	51.4°	45.7°	11.05
JO147	79.3°	50.0°	11.10
JO160	48.2°	92.7°	10.04
JO171	34.6°	86.2°	10.56
JO175	55.5°	68.6°	10.53
JO194	47.6°	89.1°	11.11
JO201	43.7°	4.9°	10.65
JO204	65.6°	144.2°	10.74
JO206	66.6°	120.7°	10.89
JW39	57.7°	101.3°	11.22
JW100	65.5°	6.1°	11.47

* anti-clockwise from North direction

Chapter 5

Results for the control-sample

This section presents the main results for the control-sample galaxies obtained by the procedure described in the previous section. At first, in Section 5.1 a spaxel by spaxel analysis is performed to appreciate the spatial distribution of the metallicity and its radial profile. Then, in Section 5.2 the study of chemical abundance profile focuses on the H_α knots, inasmuch they are physically meaningful regions and they have a higher S/N ratio. Finally, in Section 5.3 the local and global relations between gas metallicity, SFR, gas and stellar mass are analyzed.

Throughout this chapter, I will use the galaxy A3376B0261 as an example to illustrate the analysis performed and discuss the main trends. I will, however, show also all main plots for all galaxies in my control-sample, obtained by the same analysis.

5.1 Spaxels

My study of chemical abundance distributions begins focusing on the analysis of spatially resolved maps -spaxel by spaxel- of metallicity and ionization parameter.

The galaxy A3376B0261 is a face-on galaxy and represents an ideal object for getting an insight on distributions of metallicity and ionization parameter and their errors.

In the top-left panel of Figure 5.1, the metallicity map of A3376B0261 shows a metal-rich inner region and a metallicity decreasing outward. In the top-right panel, the chemical abundance profile allows to better appreciate this negative trend. The same plot also shows a positive gradient that extends up to ~ 2 kpc from the center and a broad scatter with a possible flattening beyond 8 kpc. The measured metallicity distribution is narrower in the central region, while it is broader moving toward larger radii, where the S/N ratio is lower. Simultaneously, outside 6 kpc, the associated errors increase.

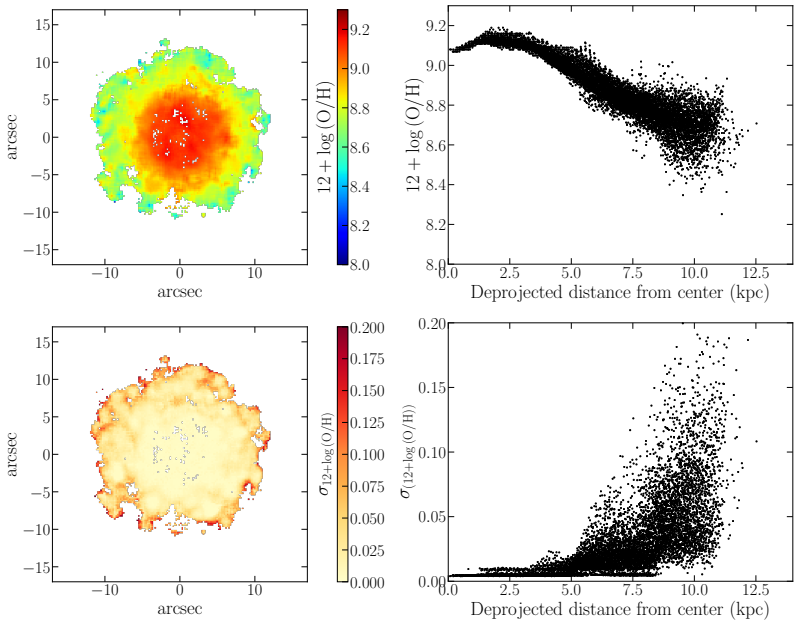

Figure 5.1: Maps (*left panels*) and radial profiles (*right panels*) -spaxel by spaxel- of metallicity (*top*) and its error (*bottom*) of A3376B0261. The errors are computed from a set of 1000 simulated line fluxes, as described in Section 4.1. In these and all maps, (0,0) is the center of the galaxy.

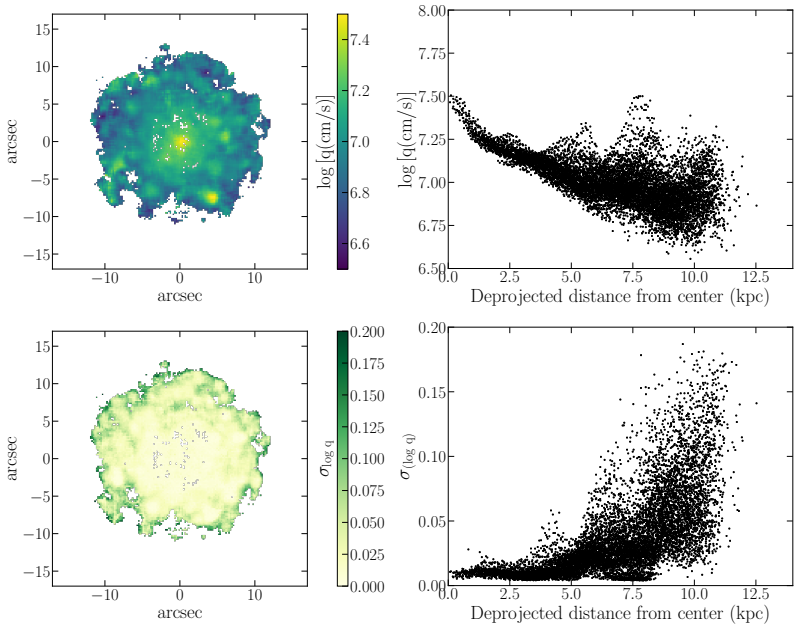

Figure 5.2: Maps (*left panels*) and radial profiles (*right panels*) -spaxel by spaxel- of ionization parameter (*top*) and its error (*bottom*) of A3376B0261, as in the Figure 5.1.

In the top-right panel of Figure 5.2 the ionization parameter profile manifests a general decreasing trend although it's characterized by some fluctuations. It's notable that below 2 kpc the gradient is steeper.

As shown in the bottom panels of Figures 5.1 and 5.2, the metallicity errors and ionization parameter errors remain below 0.025 dex up to 5 kpc.

All metallicity maps and radial profiles of control-sample galaxies are shown in Figures A.3, A.4 and A.5. For the entire sample, chemical abundance maps show the metal-rich in the central region and a decreasing toward the outskirts. The estimates of position angle and inclination obtained as described in Section 4.5 allow to deproject the galactocentric distance of each spaxel and to analyze the radial profiles of chemical abundance. For all galaxies there is an anti-correlation between the radial distance and the chemical abundance.

Some galaxies manifest particular features in the metallicity profile: A3128B0148, P25500, P21734 and P45479 present a flattening in the inner region; the metallicity decline of JO5 becomes steeper beyond 6 kpc, while JO68 shows a slightly steeper slope within 2 kpc. Some galaxies (e.g. P21734) show signs of flattening in the outer regions of the metallicity gradients. In other case (e.g. A3376B0261, JO5, P45479) only a possible hint of this feature can be suggested, because the metallicity is larger outwards.

5.2 Knots

For each galaxy, H_α knots are identified as described in Section 4.2. The line fluxes are measured from the integrated emission-only spectrum of each knot and are corrected for dust extinction. These fluxes are used to derive diagnostic diagrams, the metallicity and ionization parameter with associated errors, the star formation rate and the gas mass for each knot. The output of SINOPSIS is also integrated on the mask identifying the knots to estimate the stellar mass for each knot.

The analysis of diagnostic diagrams, performed in the previous chapter, reveals that the gas ionization in these regions is mainly produced by mechanisms of photoionization from young and bright stars. No knot emission in the control-sample galaxies is consistent with ionization due to AGNs or LINERs.

Figure 5.3 shows the distribution of knots in A3376B0261. The colour-coding indicates the metallicity and ionization parameter values for each knot.

To derive the radial distribution of the knot chemical abundance for each galaxy, the galactocentric distance of each knot is deprojected by the inclination and position angle determined as described in Section 4.7. Following Sánchez et al. (2014), no deprojection is done for galaxies with inclination $i < 35°$ to prevent that the correction increases the uncertainties on the knot distribution.

In order to compare the metallicity profiles and their gradients between different

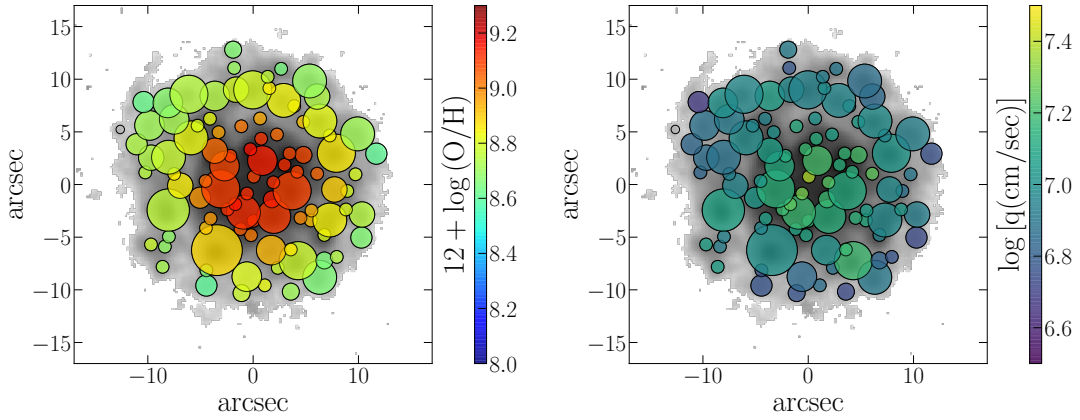

Figure 5.3: Maps of metallicity (*left*) and ionization parameter (*rigth*) of knots for A3376B0261. The dimension of each knot corresponds to the radius estimated in Section 4.2. The grey shaded area represents the H_α image.

galaxies in the sample and with literature data, it's necessary to express the slopes in physically meaningful units. For this reason the distances are given in three units: rescaling with the disk effective radius (r_e) and with r_{25} derived in Section 4.5, and converting in physical units (kpc) based on the redshift of host cluster -for cluster galaxies- or on proper redshift -for field galaxies- (see Table 3.1).

However, some important caveats concern the comparison with the literature data. A direct comparison is tricky because there are differences of data between different studies and the measurement of the metallicity gradient depends on the chemical abundance calibrator used (Sánchez-Menguiano et al., 2017).

The metallicity gradient is estimated by an error-weighted linear fit of knot chemical abundances. Since some galaxies present an inner and outer flattening in chemical abundance distribution, as showed from the spaxel by spaxel analysis, the linear fit is performed in a given range in order to prevent underestimating of the gradient. For r_e-rescaled profiles the slope is commonly derived between 0.5 and 2.0 r_e (Sánchez et al., 2014; Sánchez-Menguiano et al., 2016). In the following, I will derive the slopes between 0.5 e 1.5 r_e because some galaxies of my sample present deviations in the outer regions before 2.0 r_e, as shown in the r_e-rescaled profiles of knot metallicity in Figure 5.4. Even if in this way, the statistical number of knots is smaller, the Pearson correlation coefficients in the chosen radial range is always greater than 0.70 and the mean value is 0.88.

Table 5.1 summarizes the estimates of slopes for each control-sample galaxy.

The r_e-rescaled slopes range between -0.12 dex/r_e and -0.68 dex/r_e with a mean value $\alpha^{r_e}_{O/H} = -0.28 \pm 0.17$ dex/r_e. Figure 5.5 collects the linear fits of the profiles shown in Figure 5.4. The mean gradient is consistent with that measured by Sánchez-Menguiano et al. (2017) who find a distribution of slopes peaked at

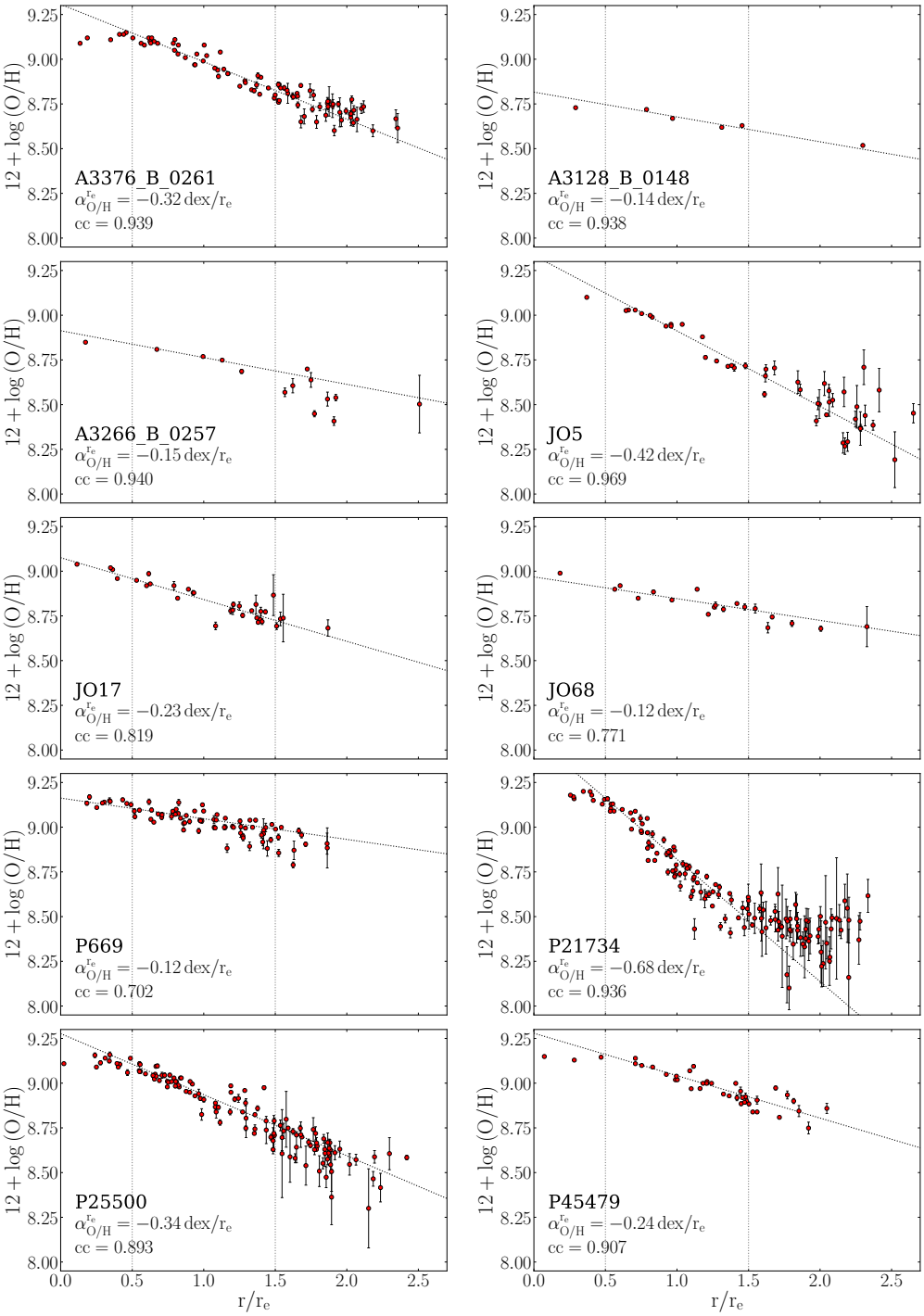

Figure 5.4: Knot metallicity profiles of all control-sample galaxies with radial distance in r_e units. All plots share the same x-axis. The black dotted line represents the linear fit performed in the radial range indicated by vertical dotted lines. The Pearson correlation coefficient and the mean slope are shown in each panel.

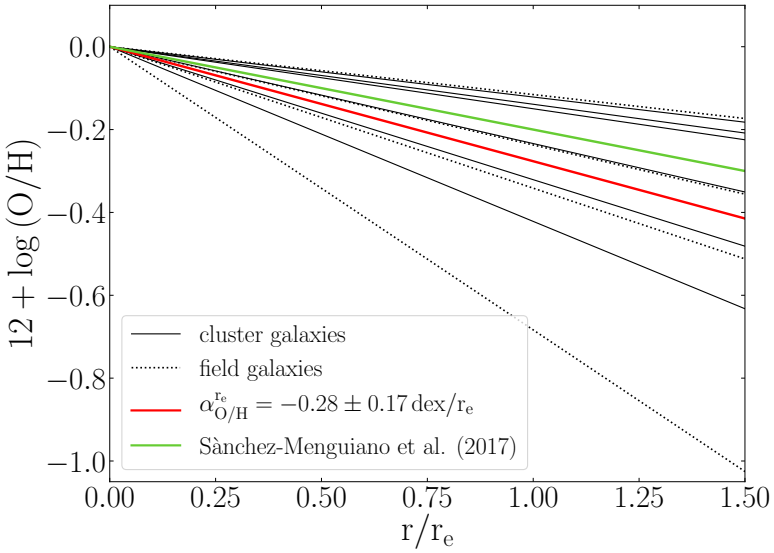

Figure 5.5: Linear fits of r_e-rescaled metallicity gradient of all control-sample galaxies. The solid black lines represent the cluster galaxies. The dashed lines indicate the field galaxies. The solid red line is the mean gradient of the sample. The solid green line is the mean slope found in Sánchez-Menguiano et al. (2017). The zero-point of each linear equation is fixed at zero.

-0.23 dex/r_e with a standard deviation of 0.07 dex/r_e, using MUSE data and the calibrator of Dopita et al. (2016).

In the r_{25}-rescaled profiles, it is not possible to find a common radial range between the inner and outer flattening present in some galaxies, as shown in the knot metallicity profile in Figure 5.6. Therefore, for r_{25} rescaled profiles, the slopes are measured only excluding chemical abundances of knots within 0.1 r_{25} from center. The metallicity associated errors of knots in outer region are always larger than in the inner region, so a possible outer flattening would not affect the error-weighted linear fit significantly. This decision is also supported by Pearson correlation coefficient that, in the considered radial range, is always greater than 0.80 for all distributions.

With this analysis the slopes range between -0.28 dex/r_{25} and -1.81 dex/r_{25} demonstrating a wide spread with a mean value $\alpha^{r_{25}}_{O/H} = -0.87 \pm 0.53$ dex/r_{25}.

The gradients are compared with those estimated by Pilyugin, Grebel, & Kniazev (2014), who have analyzed 3740 published spectra of HII regions in 130 nearby late-type galaxies with an empirical calibrator.

Figure 5.7 collects the linear fits of the profiles presented in Figure 5.6 and it shows that metallicity gradients are consistent with those measured by Pilyugin, Grebel, & Kniazev (2014), although the slopes in my work tend to be slightly steeper.

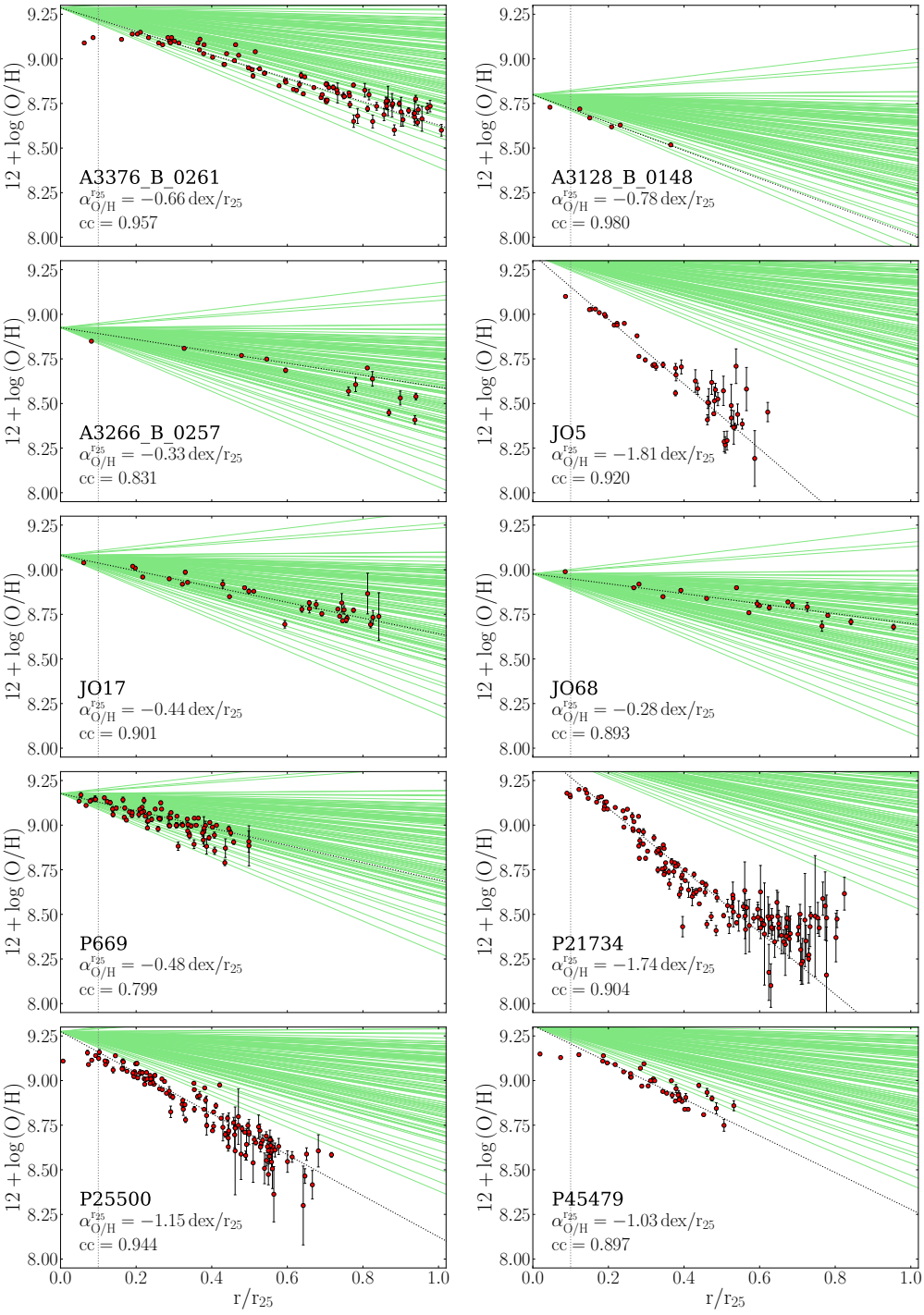

Figure 5.6: Knot metallicity profiles of all control-sample galaxies with radial distance in r_{25} units. All plots share the same x-axis. The black dotted line represents the linear fit performed excluding data within the vertical dotted line. The green lines are gradient slopes estimated by Pilyugin, Grebel, & Kniazev (2014) and their zero-points are fixed at the zero-point of the linear fit. The Pearson correlation coefficient and the mean slope are shown in each panel.

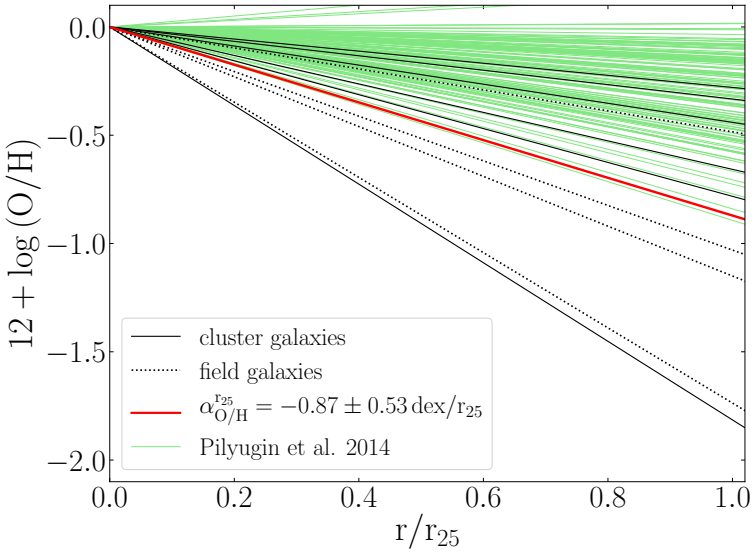

Figure 5.7: Linear fits of r_{25}-rescaled metallicity gradient of all control-sample galaxies. The solid black lines represent the cluster galaxies. The dashed lines indicate the field galaxies. The solid red line is the mean gradient of the sample. The solid green line is the mean slope found in Sánchez-Menguiano et al. (2017). The green lines are gradient slopes estimated by Pilyugin, Grebel, & Kniazev (2014). The zero-point of each linear equation is fixed at zero.

The comparison between the r_e-rescaled profiles and the r_{25}-rescaled profiles shows that r_{25} is less suitable to normalize the radial coordinates than r_e which is instead linked with the disk scale-length. The disk effective radius results physically more meaningful suggesting that the metallicity gradient and the surface brightness profile of the disk are the product of same physical mechanisms.

Finally, the gradient analysis is performed expressing the radial distances in physical units (kpc). In this case, the gradients are measured from 1.8 kpc outwards. The results are reported in Table 5.1, while the metallicity distributions are in Figure A.6 in Appendix.

All metallicity profiles show a clear negative gradient. The low number of galaxies doesn't allow for now to perform a full statistical analysis but the comparison with the literature data is comforting, though the studies based on empirical calibrators provide less steep gradients. The GASP survey is still ongoing and, when completed, it will achieve an adequate statistics with twice the number of control-galaxies.

It is worth noting that the slopes are sensitive, not only to calibrators, but also to the estimates of effective radius, r_{25}, galactic inclination and position angle used to deproject and rescal the radial distance.

However, some considerations about the shape of metallicity radial

distributions are relevant. Some metallicity profiles in this work exhibit a clear flattening or even a drop in the inner region. This behaviour is already highlighted in several studies (Rosales-Ortega et al., 2011; Sánchez et al., 2012b, 2014). Although the origin of this feature is still not clear, some authors notice that $\sim$60% of galaxies showing the inner flattening have a bar or a star-forming ring. Sánchez-Menguiano et al. (2017) find a correspondence between the presence of an inner drop or flattening and slightly steeper gradients. In addition, they argue that this behaviour is more common in more massive galaxies.

The control-sample galaxy P21734 seems to support this last hypothesis. This object is a late-type spiral with the largest stellar mass in the control-sample ($\log(M_\star/M_\odot) = 10.82$). A visual inspection doesn't detect any bar or stellar ring and its radial profile manifests a definite inner and outer flattening and a very steep metallicity gradient (-0.68 dex/$\mathrm{r_e}$).

A3376B0261 and P25500 exhibit a similar behaviour: both galaxies have a inner flattening and beyond 1.5 $\mathrm{r_e}$ their knot metallicity distributions show a wide scatter. Both are massive ($\log(M_\star/M_\odot) = 10.62$ and 10.81 respectively) and their metallicity slopes are steeper than the mean (-0.32 and -0.34 dex/$\mathrm{r_e}$ respectively).

Although JO5 isn't one of the most massive objects in the control-sample ($\log(M_\star/M_\odot) = 10.12$), it shows several analogies with the aforementioned massive galaxies: an outer flattening with a wide knot metallicity scatter, a deviation of the metallicity gradient in the inner region and the second steepest slope of the control-sample (-0.42 dex/$\mathrm{r_e}$).

Table 5.1: Metallicity slope estimates for the control-sample galaxies.

galaxy	$\alpha^{\mathrm{r_e}}_{\mathrm{O/H}}$ [dex/$\mathrm{r_e}$]	$\alpha^{\mathrm{r_{25}}}_{\mathrm{O/H}}$ [dex/$\mathrm{r_{25}}$]	$\alpha^{\mathrm{kpc}}_{\mathrm{O/H}}$ [dex/kpc]	$\log(M_\star/M_\odot)$
A3376B0261	-0.32	-0.66	-0.062	10.62
A3128B0148	-0.14	-0.78	-0.053	9.99
A3266B0257	-0.15	-0.33	-0.039	10.02
JO5	-0.42	-1.81	-0.069	10.12
JO17	-0.23	-0.44	-0.037	10.06
JO68	-0.12	-0.28	-0.028	10.06
P669	-0.12	-0.48	-0.020	10.52
P21734	-0.68	-1.74	-0.049	10.82
P25500	-0.34	-1.15	-0.027	10.81
P45479	-0.24	-1.03	-0.045	10.67

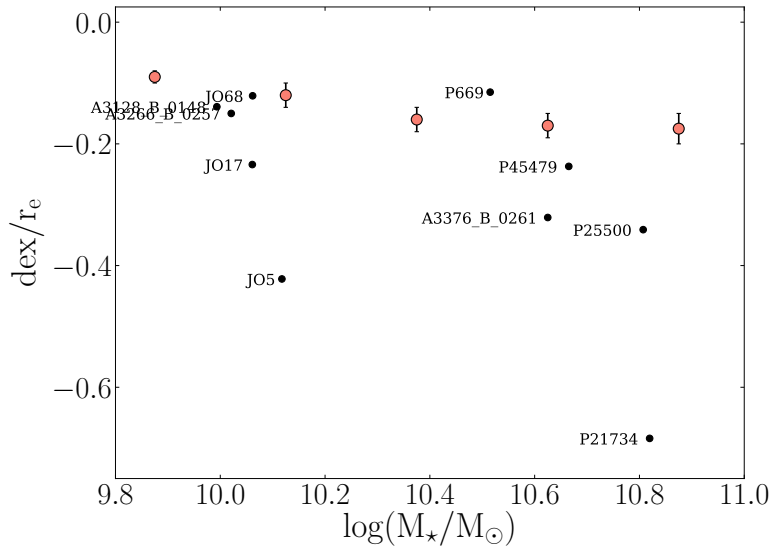

Figure 5.8: r_e metallicity gradient *vs.* stellar mass of galaxies. The red dots are the median values with corresponding errors of Figure 9 in Belfiore et al. (2017).

5.3 Metallicity dependence on global and local galaxy properties

In this section, the dependence of the gas-phase metallicity on the local and global properties of the galaxy is explored. The gradients derived in the previous section are compared with the total stellar mass of galaxies in Figure 5.8, see also Table 5.1. The number of galaxies in my sample is too small to draw final conclusions. However, my results shows rather interesting general trends that can be used to suggest some general properties. In Figure 5.8 my results are compared with the median measurements derived by Belfiore et al. (2017) that used a calibrator based on R_{23} on MaNGA data. The results are consistent considering that the authors also find outliers with steeper gradients, until 0.4 dex from the median.

The much better known dependence is between stellar mass and metallicity both for galaxy-integrated values (Tremonti et al., 2004; Kewley & Ellison, 2008; Hirschauer et al., 2018) and spatially-resolved values (Sánchez et al., 2017; Belfiore et al., 2017). This relation is investigated for galaxies in my sample. For this analysis the total stellar mass is compared both with the central metallicity and with the metallicity at $r = r_e$ in Figure 5.9. The first one is estimated as the mean spaxel abundance within 1 kpc from the center, while the latter is computed from the metallicity gradient for each galaxy.

The left panel in Figure 5.9 illustrates a good correlation (Spearman correlation coefficient is 0.90, Pearson correlation coefficient is 0.71) between the central

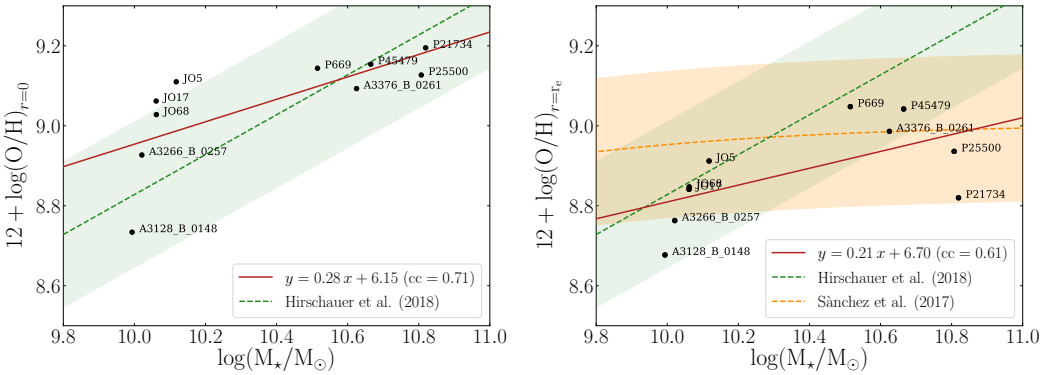

Figure 5.9: Total stellar mass-metallicity distribution. *Left*: The chemical abundance along y-axis is the central metallicity, the green dashed line and the area are the relation in Hirschauer et al. (2018) and its standard deviation, the red solid line is the linear fit in the legend with the Pearson correlation coefficient equal to 0.71. *Right*: r_e metallicity *vs.* the total stellar mass. The green line is as in the left panel, the orange dashed line and the area are the relation found in Sánchez et al. (2017) and its standard deviation. The red solid line is the linear fit in the legend with the Pearson correlation coefficient equal to 0.61.

metallicity and stellar mass. My results show a quite good agreement with Hirschauer et al. (2018), although theirs are integrated metallicities derived from the galactic spectra of KISS (KPNO International Spectroscopic Survey; Salzer et al., 2000) using a $O3N2$ calibrator. Instead, in the right panel, the r_e metallicity *vs.* stellar mass plot doesn't show a clear relation (Spearman correlation coefficient is 0.55, Pearson correlation coefficient is 0.61). The small number of targets in my study may affect the statistical significance of this result. However it is compatible with the relation from Sánchez et al. (2017) within the standard deviation of the distribution of their abundances using `pyqz`.

Many studies have highlighted that this relation is valid also considering the local stellar surface mass density. Previous insights on HII regions have documented that more metal-rich regions have larger stellar mass densities than less metal-rich ones (Vila-Costas & Edmunds, 1992; Edmunds & Pagel, 1984). Later, Moran et al. (2012) found a trend between the surface mass density and the metallicity using long-slit spectroscopy. Recently, using IFS data Rosales-Ortega et al. (2012) and Barrera-Ballesteros et al. (2016) argue that the presence of a global mass-metallicity relation is a reflection of a local relation and that this is an explanation of metallicity gradient inasmuch they have a common origin.

The analysis carried out on the sample of control-galaxies confirms these results. The top-left panel of Figure 5.10 shows that the knot metallicity *vs.* knot stellar mass reproduces the same shape observed in the chemical abundance profile, although there are two main sequences (the Spearman correlation coefficient is 0.65). The top-right panel illustrates the profile of the local

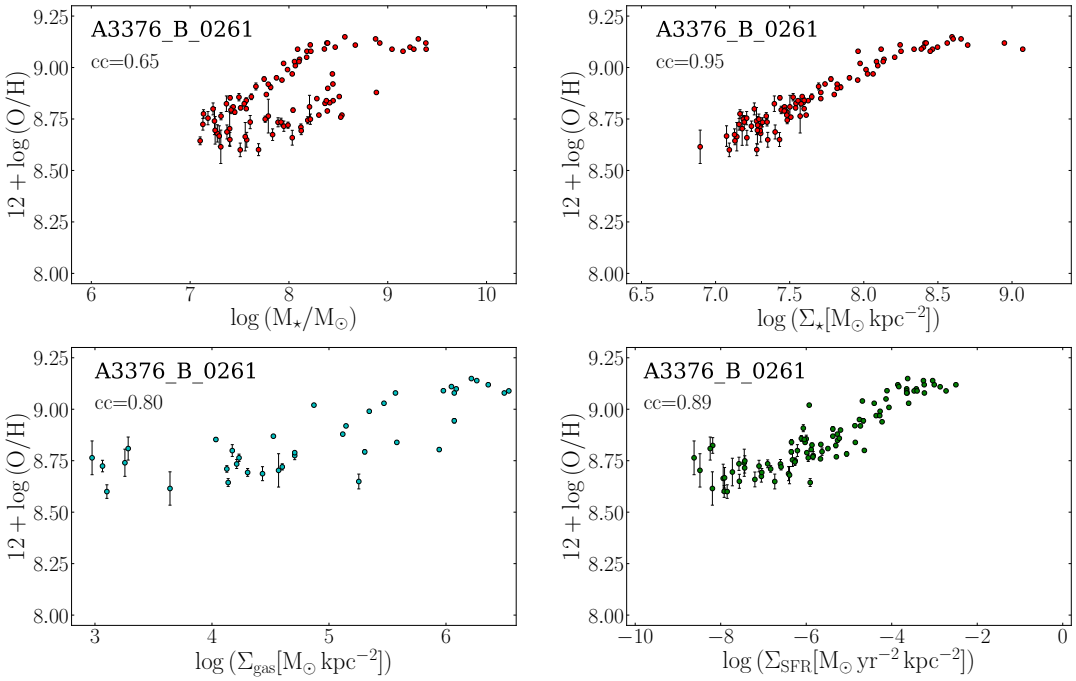

Figure 5.10: Relation between the knot metallicity and local properties for A3376B0261. *Top left*: metallicity *vs.* knot stellar mass profile. *Top right*: metallicity *vs.* surface stellar mass density profile. *Bottom left*: metallicity *vs.* surface gas mass density profile. *Bottom right*: metallicity *vs.* SFR density profile. The Spearman correlation coefficient of each profile is reported in the respective legend.

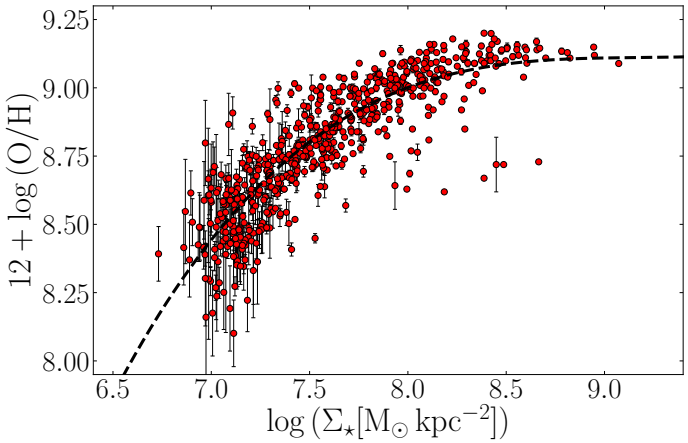

Figure 5.11: Metallicity *vs.* surface stellar mass density profile considering all knots of control-sample galaxies. The dashed line is the error-weight 3rd-order fit.

metallicity *vs.* the stellar mass density, obtained dividing the stellar mass of each knot with its dimension. This produces a single and more definite sequence with a higher Spearman correlation coefficient (0.95). A similar relation appears in the bottom-right panel, comparing the knot metallicity with the surface star formation rate density. Instead, the dependence with average gas mass density results less tight and the distribution presents a larger scatter, as shown in the bottom-left panel.

The extraordinary correlation emerged in the metallicity *vs.*stellar mass density profile stimulates a more in-depth investigation. If all knots of control-sample galaxies are considered, the total profile, showed in Figure 5.11, is characterized by a common correlation with a Spearman correlation coefficient equal to 0.88. This distribution is fitted by an error-weighted 3rd-order polynomial and the coefficients are reported in Table 5.2.

Figure 5.12 shows the metallicity *vs.* surface stellar density relations for each galaxy. At a given mass, the metallicity of the blobs in the galaxies with the lowest mass in our sample (A3128B0148, A3266B0257, JO17, and JO68) are systematically more metal-poor than the average value obtained from the best-fit relation derived from Figure 5.11 (dashed line in each panel in Figure 5.12). Moreover, the blobs in the most massive galaxies (P21734 and P25500), and in particular those with the highest mass density, are more metal rich than the average value. To conclude, the data presented in this chapter show that the total stellar mass of the galaxy has a second-order effect on the local metallicity *vs.* stellar-mass-density relation. This link between global and local properties of galaxies is very likely connected with the galactic chemical enrichment history. A detailed study of this effect and of the astrophysical mechanisms involved in the

Table 5.2: Polynomial coefficients of the error-weight 3rd-order fit in Figure 5.11. The relation is of the form $y = ax^3 + bx^2 + cx + d$ where $y = 12 + \log(\mathrm{O/H})$ and $x = \log(\Sigma_\star)$.

a	b	c	d
0.064	−1.769	16.223	−40.490

process would require a detailed comparison with chemical evolution models; this is beyond the scope of this thesis and will be developed as prosecution of this work.

To summarize, this chapter focuses on the relationships between the gas-phase metallicity, its distribution and the global and local properties of the control-sample galaxies. I have verified that these objects are characterized by a negative metallicity gradient that results connected to the disk effective radius, finding a mean slope $\alpha^{\mathrm{r_e}}_{\mathrm{O/H}} = -0.28\,\mathrm{dex/r_e}$ in the radial range $0.5 - 1.5\,\mathrm{r_e}$.

The mass-metallicity relation was analyzed, noticing a good agreement between the central metallicity and the total stellar mass of the galaxy. Less strict relations arise when the total galaxy stellar mass was compare with metallicity slope and metallicity at $r = \mathrm{r_e}$.

The investigation of the local properties has highlighted a clear correlation between the knot metallicity and the stellar mass density. There is not an universal relation for all galaxies in the control-sample, but it depend on the total galaxy stellar mass.

In the next chapter, the jellyfish galaxies will be subjected at a similar analysis to study the metallicity distribution in the main body and in the tails. The results of the control-galaxies will be compared with the properties of the jellyfish sample, in order to verify the eventual effect of the ram-pressure stripping.

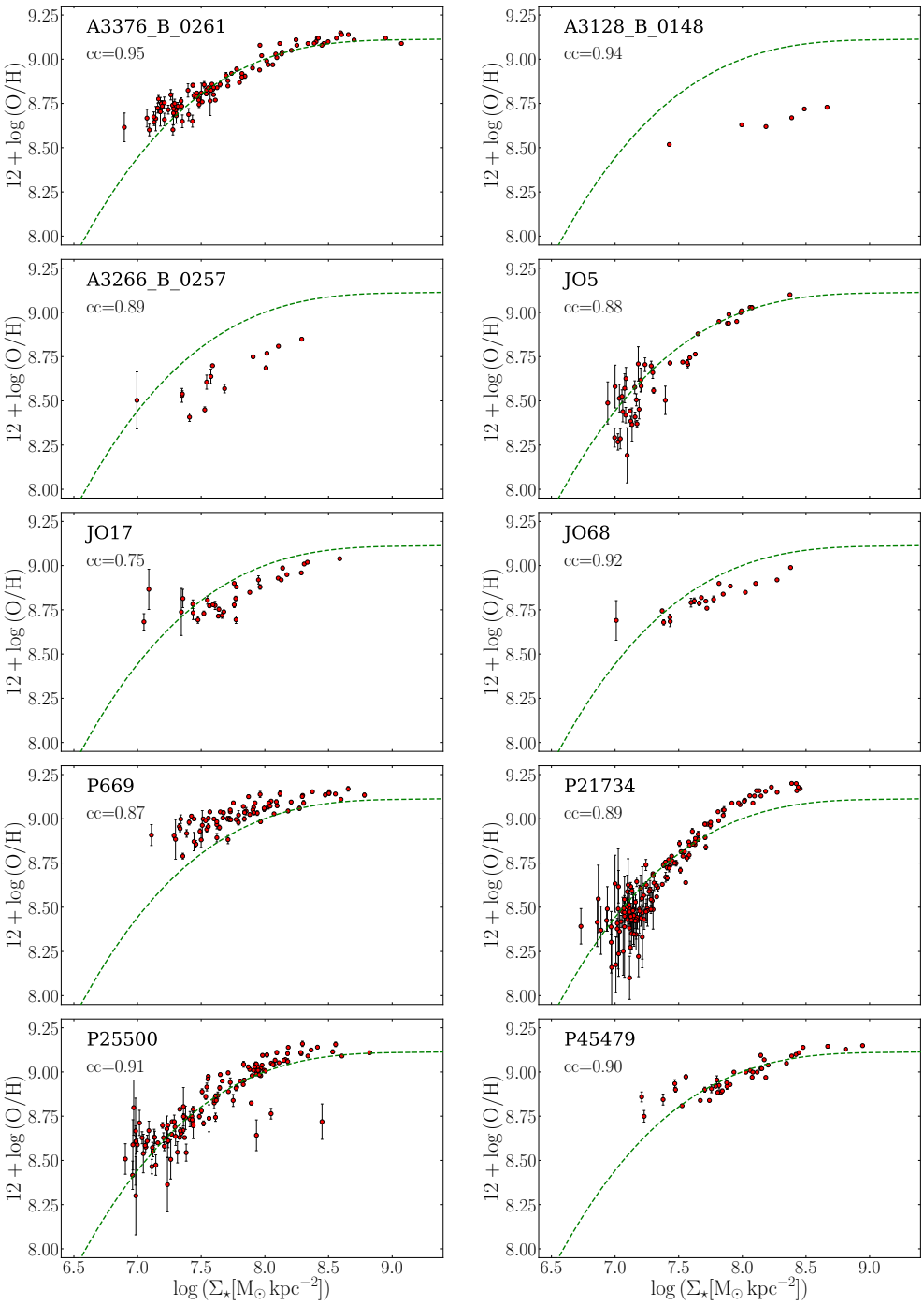

Figure 5.12: Metallicity *vs.* surface stellar mass density profile of all control-galaxies. All plots share the same x-axis. The green dashed line is the same in Figure 5.11. The Spearman correlation coefficient of each profile is shown in panels.

Chapter 6

Results for the jellyfish sample

The scope of this chapter is to understand what the metallicity can testify about the history of ram-pressure stripping.

In the previous chapter, the metallicity distribution in the control-galaxies and some relations between the chemical abundance and the galaxy properties were derived. This chapter aims to compare those results with the characteristics of the jellyfish galaxies to test the similarity or the differences with the galaxies of the control-sample.

The jellyfish galaxies are particular galaxies that present disturbed morphology with evident gas tails and debris extending out of the main galaxy body. For this reason an analysis identical to the one performed for the control-galaxies can not be applied at the sample of jellyfish galaxies. The study of the metallicity distribution is carried out in various steps. First, (Section 6.1), I present the deprojected radial profile of the chemical abundance for only the knots belonging to the main body of galaxy. In the second step (Section 6.2), I compare the chemical abundance of all knots with their projected distance from the galaxy center. Then, in Section 6.3, one of these distributions is analyzed in detail.

Unlike the metallicity distribution derived for the control-galaxies, in this chapter the radial distance of each knot (in particular the deprojected distance) is not rescaled with the effective radius of the disk, because the peculiarity of the jellyfish galaxies prevents to carry out the photometric analysis described in Section 4.5 and so to derive this quantity. The rescaling with r_{25} is not considered because this radius results less meaningful than r_e. Therefore, for the analysis of the metallicity distribution in the jellyfish galaxies the distances are converted only in physical units (kpc).

In Section 6.4, the metallicity *vs.* stellar mass density profiles are shown and compared with the relation found in Section 5.3.

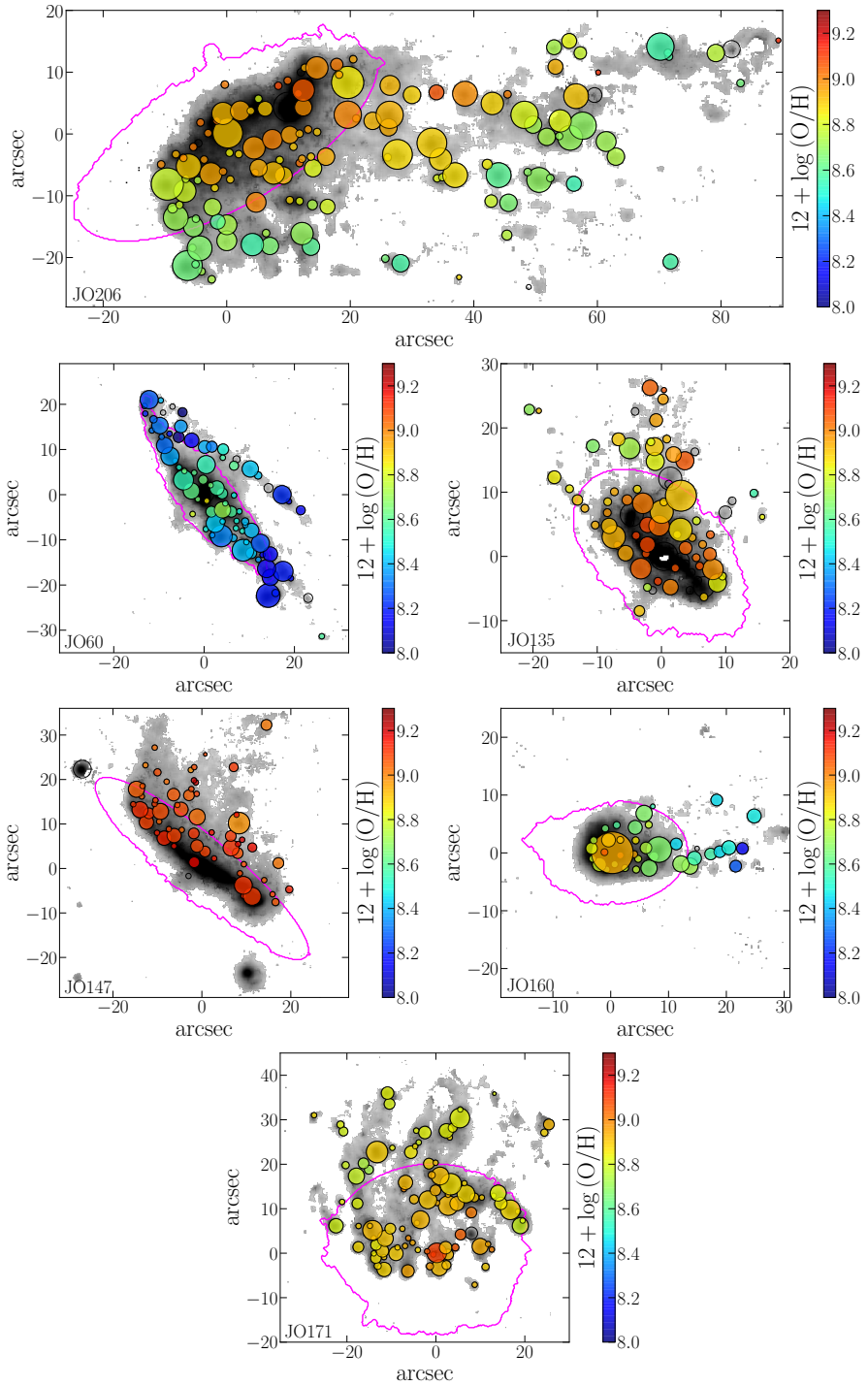

Figure 6.1: Maps of knot metallicity for the jellyfish sample. The name of each galaxy is in the plot. The dimension of each knot corresponds to the radius estimated in Section 4.2. The grey shaded area represents the H_α flux map. The magenta contour is the main galaxy body derived in Section 4.6. In these and all maps, (0,0) is the center of the galaxy.

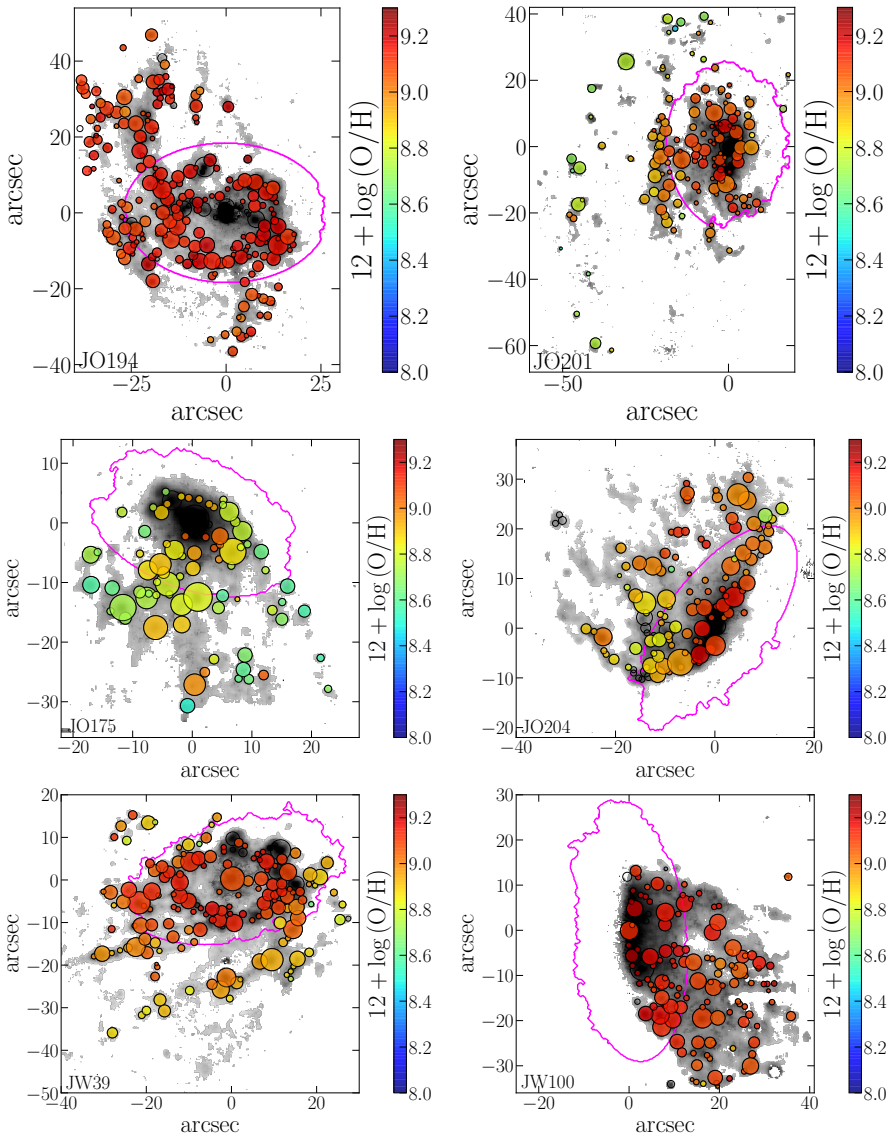

Figure 6.1: (*Continued*)

6.1 Metallicity distribution in the main galaxy body

Figure 6.1 illustrates the map of knots for each jellyfish galaxy with color-code indicating their metallicity. The knots powered by AGNs or LINERs are removed and the chemical abundance of each knots is estimated as described in Section 4.1.

The issue of the jellyfish galaxies is their disturbed morphology. Using the boundary of the main galaxy body described in Section 4.6, it is possible to discriminate the knots belonging to the stripped tails from those in the galaxy main body. These latter are selected and the analysis of the metallicity distribution inside the galaxy is performed. The galactocentric distance of each knot inside the main body is deprojected using the inclination and the position angle obtained in the same section.

Figure 6.2 illustrates the plots of the knot metallicity distribution for all jellyfish galaxies. In all profiles it is possible to note the anti-correlation between the chemical abundance and the deprojected galactocentric distance.

In some cases the scatter around the linear fit is large, but it is not clear if this is due to a scatter in metallicity or if it is an effect of uncertainties in the parameters used to deproject the galactocentric distances. In the first case it would be linked to physical processes (e.g. kinematics, chemical enrichment). In the second case, some systematic errors could be present. For example, the inclination error can under/overestimate the galactocentric distance of knots especially along the minor axis. In addition, the outline that indicates the boundary of the main galaxy body is not a definite limit; a part of extraplanar stripped gas can overlap the galaxy body along the line of sight, so the eventual extraplanar knots can be wrongly classified as belonging to the galaxy plane. In this case, the deprojection of the galactocentric distance for these knots would be meaningless.

To correctly compare the distributions it would be necessary to rescale the galactocentric distance with the effective radius, but this quantity is not available for the jellyfish galaxies. Although the slopes expressed in kpc are less meaningful and so the eventual comparisons must be taken with caution, it is worth making some considerations. The least massive galaxies (JO160, $\log(M_\star/M_\odot) = 10.04$; JO60, $\log(M_\star/M_\odot) = 10.33$; JO175, $\log(M_\star/M_\odot) = 10.53$) in the jellyfish sample present the largest metallicity range ($\sim$0.7 dex) with the lowest knot metallicities, especially JO60. Instead the most massive ones (JW100, $\log(M_\star/M_\odot) = 11.47$; JW39, $\log(M_\star/M_\odot) = 11.22$; JO194, $\log(M_\star/M_\odot) = 11.11$; JO147, $\log(M_\star/M_\odot) = 11.10$) have high knot metallicities and the chemical abundance range is only 0.1 dex.

As already explained, the comparisons can be tricky, but it is curious that there is a systematic difference between the gradients of control-galaxies (steeper) and

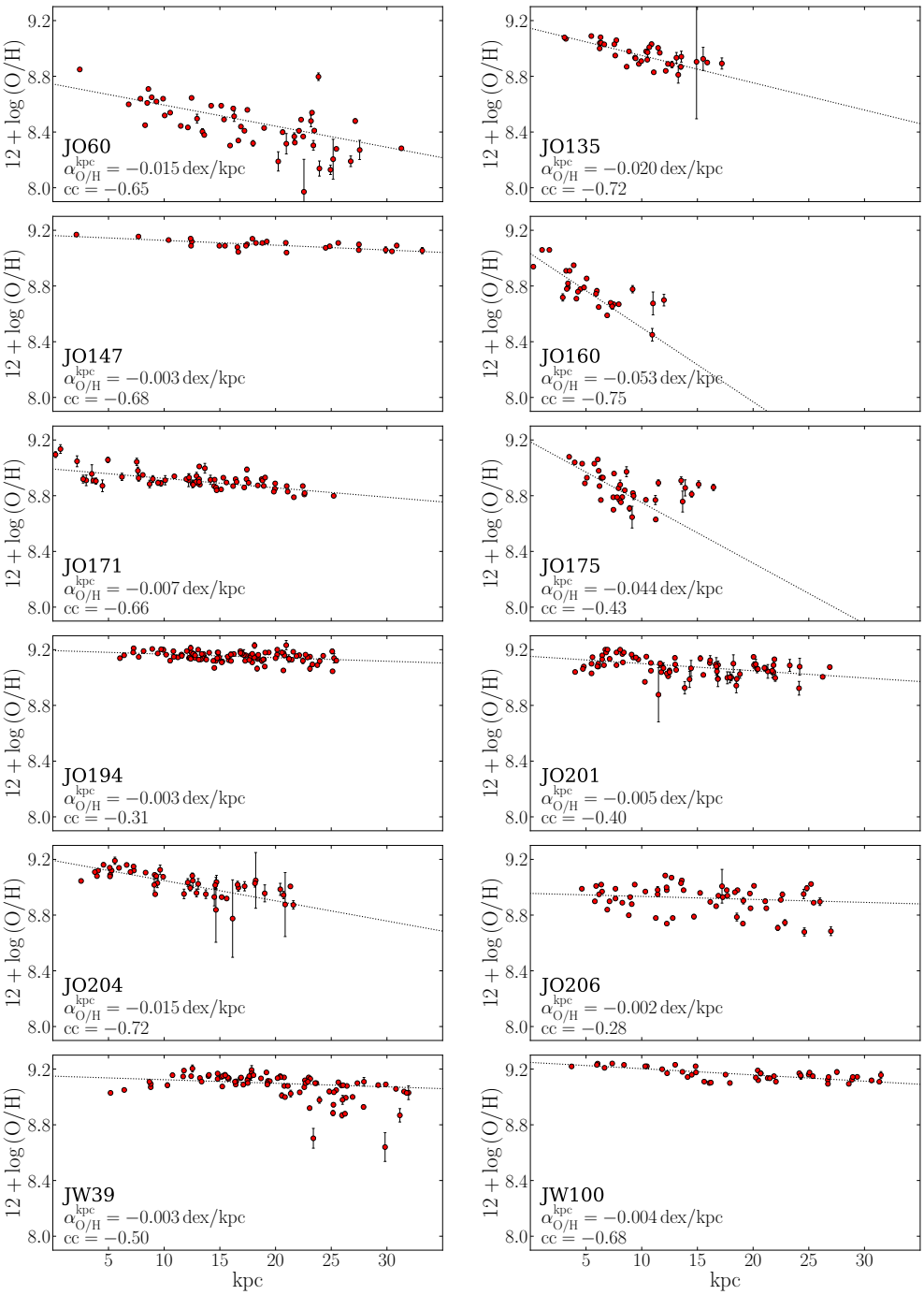

Figure 6.2: Deprojected knot metallicity distribution in the main galaxy body for the whole jellyfish sample.

those of jellyfish galaxies (flatter). It would be interesting to understand if the consequences of the ram-pressure stripping is to "spread" the gas still bound to galaxy and so to "stretch" the metallicity gradient.

A complete study of the metallicity distribution requires to analyze the chemical abundance of the gas tails.

6.2 Metallicity distribution along the tails

The study of the knot metallicity distribution including the tails and the gas debris is more complex, because the three-dimensional geometry of the problem prevents to suitably measure the distances. The knot metallicity is simply compared with the galactocentric distance projected on the sky plane, so without deprojection. Therefore, some distances can be underestimated.

Figure 6.3 shows the profiles of knot metallicity *vs.* projected distance from the center for each jellyfish galaxy. In these plots the knots located in the tails are indicated with empty dots, while those in the galaxy body are in red. To simplify the discussion I will indicate the knots belonging to the main body with the notation "knot$_{\rm in}$", and the knots belonging to the tails with "knot$_{\rm out}$". The situation is very heterogeneous because the combination of different galaxy inclinations and different directions of ram-pressure action produces unique and peculiar configurations. Therefore it is more sensible to individually discuss each galaxy.

JO60 : This galaxy is a high inclination (77.4°) spiral with a galactic warp and a gas tail nearly parallel to the major-axis. The metallicity distribution in Figure 6.3 shows that the knot metallicity spreads over 0.8 dex and the chemical abundance of knots$_{\rm out}$ is similar to that of knots$_{\rm in}$. In general, the gas removal mechanism has altered the morphology of this object, but the degree of this phenomenon is not clear.

JO135 : It presents some tails along the North direction. The knots of the main tail are powered by various ionization mechanisms, most by composite source, as shown in Figure 4.1. This is maybe the reason for the fluctuations in the knot$_{\rm out}$ metallicity distribution with a spread of 0.5 dex. However most knots$_{\rm out}$ have lower metallicity than the inner knots$_{\rm in}$.

JO147 : It is an edge-on galaxy with the highest inclination in the jellyfish sample (79.3°), analyzed also in Merluzzi et al. (2013). It presents a wide crest of gas toward the North-West direction with knots dominated by composite sources. The metallicity distribution ranges between 9.0 and 9.2 dex. The chemical abundances of the knots$_{\rm out}$ result similar to those of the knots$_{\rm in}$, but the former

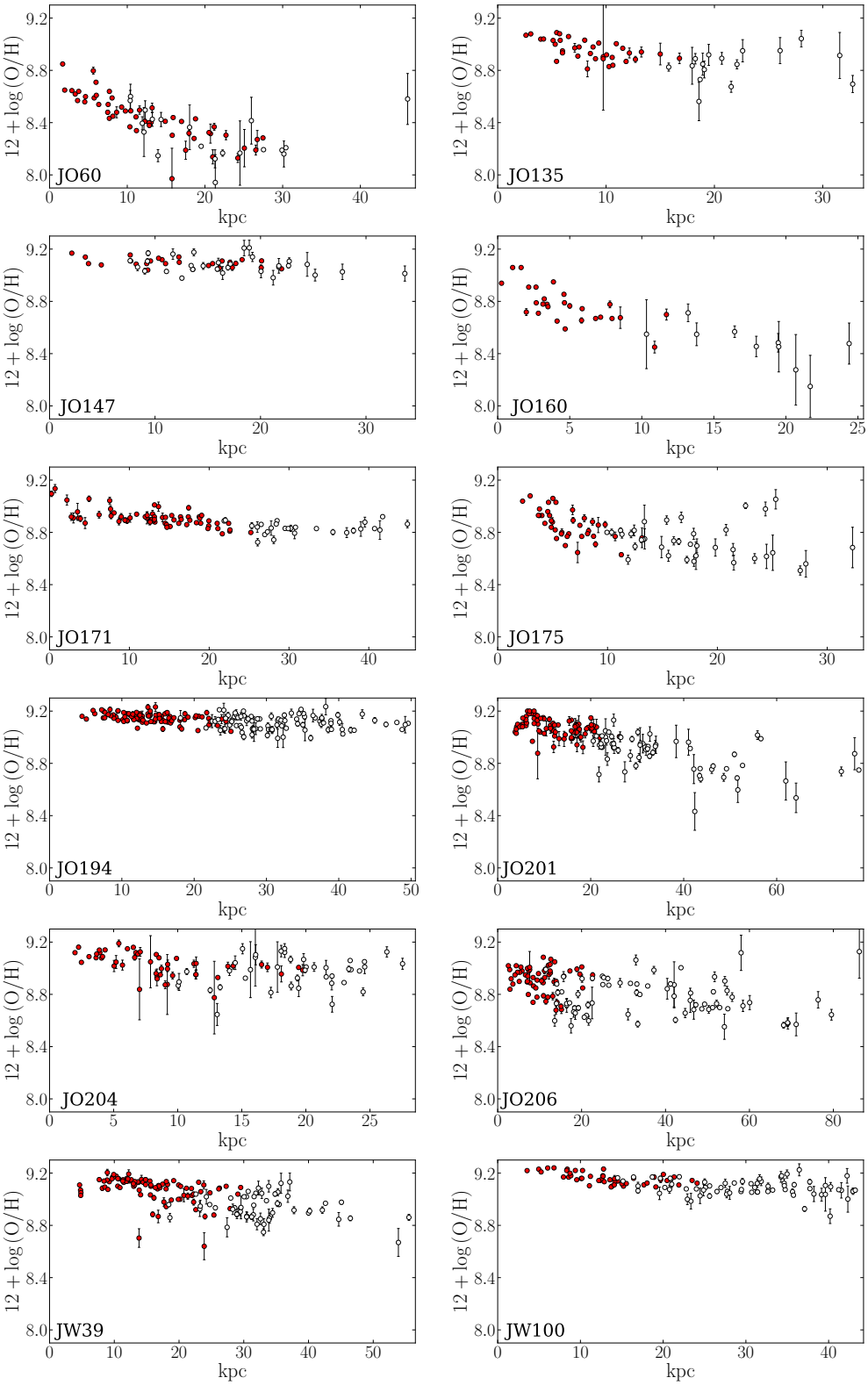

Figure 6.3: Metallicity distribution of all knots (not deprojected). Red filled dots are the knots$_{\rm in}$, the empty dots are the knots$_{\rm out}$.

present a larger scatter. In general, the galaxy is characterized by a high metallicity for all its knots, probably linked to its large mass ($\log(M_\star/M_\odot) = 11.10$).

JO160 : This galaxy has gas debris along the West direction with star-forming knots. Its metallicity profile in Figure 6.3 shows a clear negative gradient with metallicity ranging between 9.0 and 8.6 for the knots_{in} and between 8.6 and 8.2 for the $\text{knots}_{\text{out}}$.

JO171 : This low inclination galaxy, characterized by a ring of young stars, is described in detail by Moretti et al. (2018). It is devoid of gas in the South-side, while along the North-direction it presents some gas tails. The knots are mainly powered by star-forming emission. The negative gradient inside the main galaxy body is confirmed also in the tails. The knot_{out} metallicity is lower than knot_{in} metallicity with a difference of 0.1 dex.

JO175 : It is characterized by a wide tail of gas toward the South direction, that branches out into multiple tails. The knots are dominated by stellar photoionization and composite sources. The metallicity profile shows a general negative gradient, but there are some outliers toward high metallicities and double or even triple trends. It is not clear if the stripped gas belonged only to the outer region of galaxy or also to the inner one.

JO194 : This object is a massive ($\log(M_\star/M_\odot) = 11.11$) spiral with evident gas tails and debris both in the North and South directions. The knots are mainly ionized by star-forming emission and composite sources. This galaxy is metal-rich in all its extent. The metallicity distribution ranges between 9.0 and 9.2 dex with a nearly flat, but negative trend.

JO201 : This galaxy, studied in detail in Bellhouse et al. (2017), is a low inclination spiral with frontal ram-pressure stripping. It presents some gas debris on the East, North and South-East sides. Most of knots are powered by stellar and composite radiation. The chemical abundance distribution shows a clear negative trend. The metallicity knot_{in} spreads from 9.2 down to 8.9 dex, while that of $\text{knots}_{\text{out}}$ results lower down to 8.5 dex.

JO204 : This galaxy, described in detail in Gullieuszik et al. (2017), is an highly-inclined galaxy with a gas crest toward the North-East direction. It presents a group of knots dominated by AGN emission, likely due to the ionization cone of the central AGN. The rest of the knots are powered by stellar photoionization and composite sources. The chemical abundance distribution shows that the profile of the knot_{in} metallicity presents a negative trend, while the distribution of the knot_{out} metallicity is characterized by scatter.

JO206 : This object is presented in Poggianti et al. (2017a), and it is a galaxy with a series of very long gas tails. Excluding a central knot powered by an AGN, the rest of the knots are dominated by star-forming and composite emission. The spectacular morphology allows to obtain a quite faithful trend of the chemical abundance into the tails. The knot_{out} metallicity distribution shows a clear negative gradient with two main sequences.

JW39 : This galaxy presents some spiral arms that open toward the North direction. It presents only a central knot ionized by LINERs and no AGN. The metallicity distribution is characterized by a general negative trend that branches in two or three sequences.

JW100 : This highly-inclined galaxy is the most massive galaxy ($\log(M_\star/M_\odot) = 11.47$) in the sample. It presents an extensive gas crest toward the South-West direction. The knots are characterized by high metallicity that ranges between 9.0 and 9.2 dex. However, the chemical abundances of the $\text{knots}_{\text{out}}$ are lower than those of the knots_{in}.

To summarize, the metallicity distribution of the galaxies with high inclination shows knots_{in} and $\text{knots}_{\text{out}}$ at the same projected distances: $\text{knots}_{\text{out}}$ of JO206 are metal-poor than the knots belonging to the main body; for JO60 and JW100, the chemical abundance of the $\text{knots}_{\text{out}}$ is comparable with ones of the knots_{in}; the same behaviour is manifested in JO147, but in this case the $\text{knots}_{\text{out}}$ present a larger metallicity scatter than the knots_{in} and for JO204 this scatter results more evident.

The galaxies with low inclination or with long gas tails present $\text{knots}_{\text{out}}$ at greater distances than the knots_{in}: in most of the cases the chemical abundance of the knots in the tails follows the trends toward lower metallicity than the knots_{in} (JO160, JO175, JO201, JO206, JW39) with some outliers toward high metallicity for JO175, JO206 and JW39; in other cases the metallicity distribution of the $\text{knots}_{\text{out}}$ results quite flat (JO135, JO171, JO194, JO204, JW100) and for JO135 and JO204 the metallicity distribution presents evident fluctuations.

6.3 An emblematic case: JO206

When the metallicity distribution shows particular features, a more in-depth analysis can provide interesting results. This is the case of the galaxy JO206. Its knot metallicity distribution in Figure 6.3 presents two distinct trends. Both of them cover a metallicity range of 0.4 dex, but one extends from the center up to 20 kpc, while the other up to 80 kpc. In Figure 6.4 (top panel), these two trends are selected and separated with two different colors. Checking the position of the

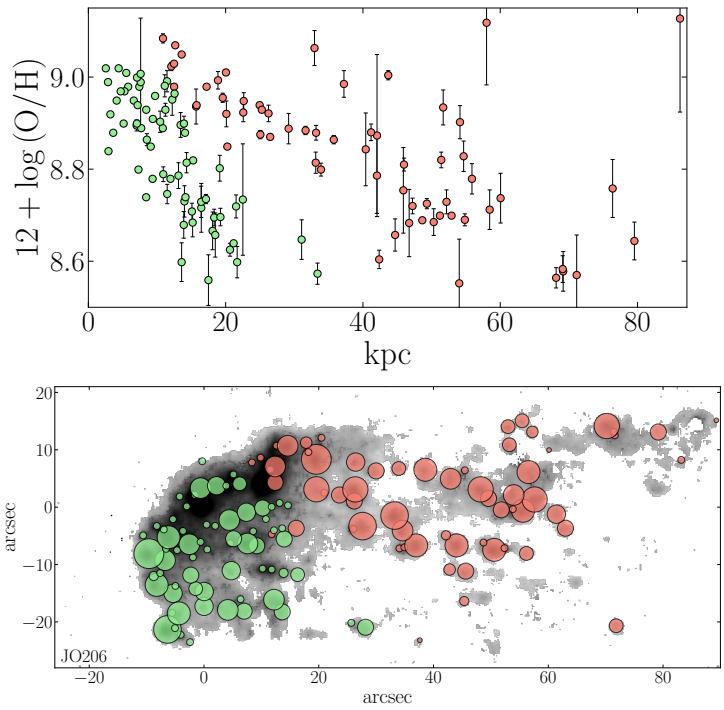

Figure 6.4: Individual analysis of the galaxy JO206. *Top*: knots metallicity distribution, as in Figure 6.3. The data tracing the two main trends are selected and marked with two different colors. *Bottom*: map of knots with the corresponding color of the top panel. The shaded area is the H_α image.

selected knots in the maps of the galaxy (bottom panel), the data of the steeper trend correspond to the South gas tail and the data of the less steep one coincides with the knots of the North tail. This is a remarkable result because it testifies on the gas removal mechanism. The ram-pressure stripping is more effective for the red tail, that is more extended than green one.

In Chapter 5, I showed that normal galaxies (galaxies without signs of disturbed morphology) are characterized by a clear negative metallicity gradient. The study of the metallicity of JO206 reveals the same negative gradient in its gas tail, proving that the ram-pressure strips the gas of the galaxy initially from the outer and metal-poor regions and then gradually from the inner and metal-rich regions.

In the light of these results, I conclude that the metallicity traces the ram-pressure stripping history and the chemical abundance study is an optimal method of analysis for obtaining insight into the jellyfish galaxies and gas removal phenomena.

Given the peculiarity of the jellyfish galaxies, a future work would focus on individual analysis of metallicity for each objects with eventual use of chemical evolution and ram-pressure stripping models.

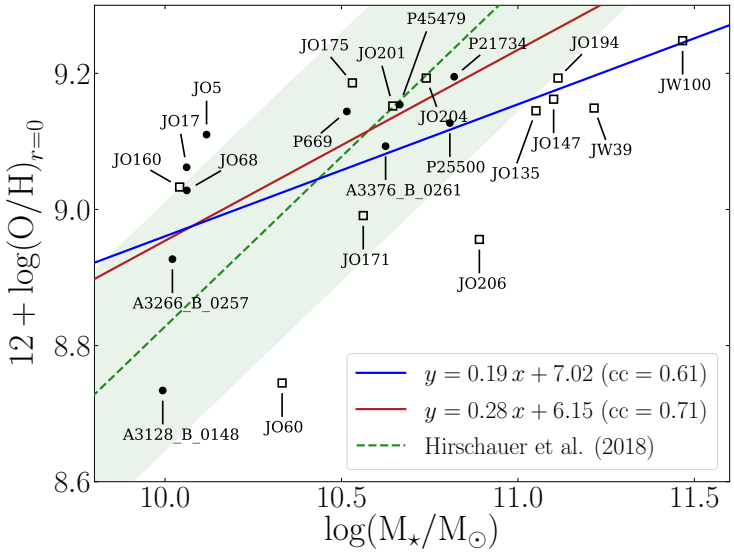

Figure 6.5: Central metallicity *vs.* total stellar mass. The black dots indicate the control-galaxies and the empty squares correspond to the jellyfish galaxies. The green dashed line and the area are the relation in Hirschauer et al. (2018) and its standard deviation. The blue line is the linear fit considering all galaxies with the Pearson correlation coefficient equal to 0.61, while the red line is the linear fit considering only the control-galaxies (see Figure 5.9), with the Pearson correlation coefficient equal to 0.71.

6.4 Metallicity dependence on galaxy properties

As in Section 5.3, in this section an analysis about the metallicity dependence on the global and local properties (total stellar mass, stellar and gas mass density, star formation rate) is presented.

To compare the central metallicity of the jellyfish galaxies with the total stellar mass, some caveats must be kept in mind. Most jellyfish galaxies present an AGN or regions dominated by LINERs. Since the method used to estimate the chemical abundance can be applied only for the star-forming regions, the zero-point of the linear fit performed on the deprojected knot metallicity distributions in Figure 6.2 is assumed to represent the central chemical abundance, though in some case that is not fully guaranteed.

In Figure 6.5, the total stellar mass of each galaxy in the whole sample (control-sample and jellyfish sample) is compared with its central metallicity.

It is possible to note a good positive correlation and most of the data are consistent with the relation of Hirschauer et al. (2018) within its standard deviation, even if toward high masses, my data are located at lower metallicity than the relation. Some authors (Tremonti et al., 2004) found the same flattening of chemical abundance trend at high stellar mass. Tremonti et al. (2004) interpret

this characteristic as a physical limit of the metal enrichment produced by stellar system. Hirschauer et al. (2018) found a similar flattening, in fact all their data with stellar mass $\log(M_\star/M_\odot) > 10.8$ have lower metallicities than their relation.

To complete the analysis, the metallicity dependence on local galaxy properties in jellyfish galaxies is investigated. In Section 5.3, a strong relation between the knot metallicity and the stellar mass density was discovered. In this section, I will compare it with the data coming from the jellyfish galaxies.

Figure 6.6 illustrates the local mass-metallicity plots for the jellyfish sample, where the line is the relation found in Figure 5.11 for the control-galaxies. In these panels, the correlation results less strong and the average Spearman correlation coefficient is lower than that found for the control-galaxies.

Only in a few galaxies (JO135, JO147, JO175), the data of knots_{in}, especially those with higher mass density, follow the relation. In most cases, the knots in the most massive galaxies (JO194, JW39, JW100) are systematically more metal-rich than the relation. In contrast, the knots_{in} of the least massive galaxies in the jellyfish sample (JO160, JO60) are located at lower metallicities than the average value for that mass (dashed line).

Regarding the knots in the tails, their metallicities are often similar to those of knots of the main galaxy body, but the $\text{knots}_{\text{out}}$ have systematically lower stellar mass densities. If all these distributions are compared, as in Figure 6.7, it is notable that $\text{knots}_{\text{out}}$ and a part of knots_{in} don't shows a common relation and they are distributed on a wide area above the line.

The stellar mass density of the $\text{knots}_{\text{out}}$ is due to only the young stars born in situ by recent star-forming events. While the metal enrichment occurred by evolution of the stellar component in the original position of removed gas, even if self-enrichment of knots by the stars in situ or mixing with ICM could be not negligible. However, the metallicity of the knots represents an upper limit of the enrichment occurred in the galaxy disk. This mismatch between the relation found for the control-galaxies and the data of the jellyfish galaxies is a further proof of the action of ram-pressure stripping. This mechanism eradicates the gas from the galaxy, keeping unchanged the stellar component.

The comparison between the knot metallicity and the other local galaxy properties (gas mass density and ongoing star formation rate density) are shown in Figures A.7, A.8 and A.9 in Appendix. Both SFR density and mass gas density are on average lower in the $\text{knots}_{\text{out}}$ with respect to the knots_{in}, even if there is overlapping between the ranges of the knots_{in} and those of the $\text{knots}_{\text{out}}$. Like in Figure 6.7, Figure A.9 doesn't show a clear metallicity trend with the two quantities, common for all jellyfish galaxies.

To summarize, this chapter has presented an overview on the metallicity properties of the jellyfish galaxies. All them show a negative chemical abundance

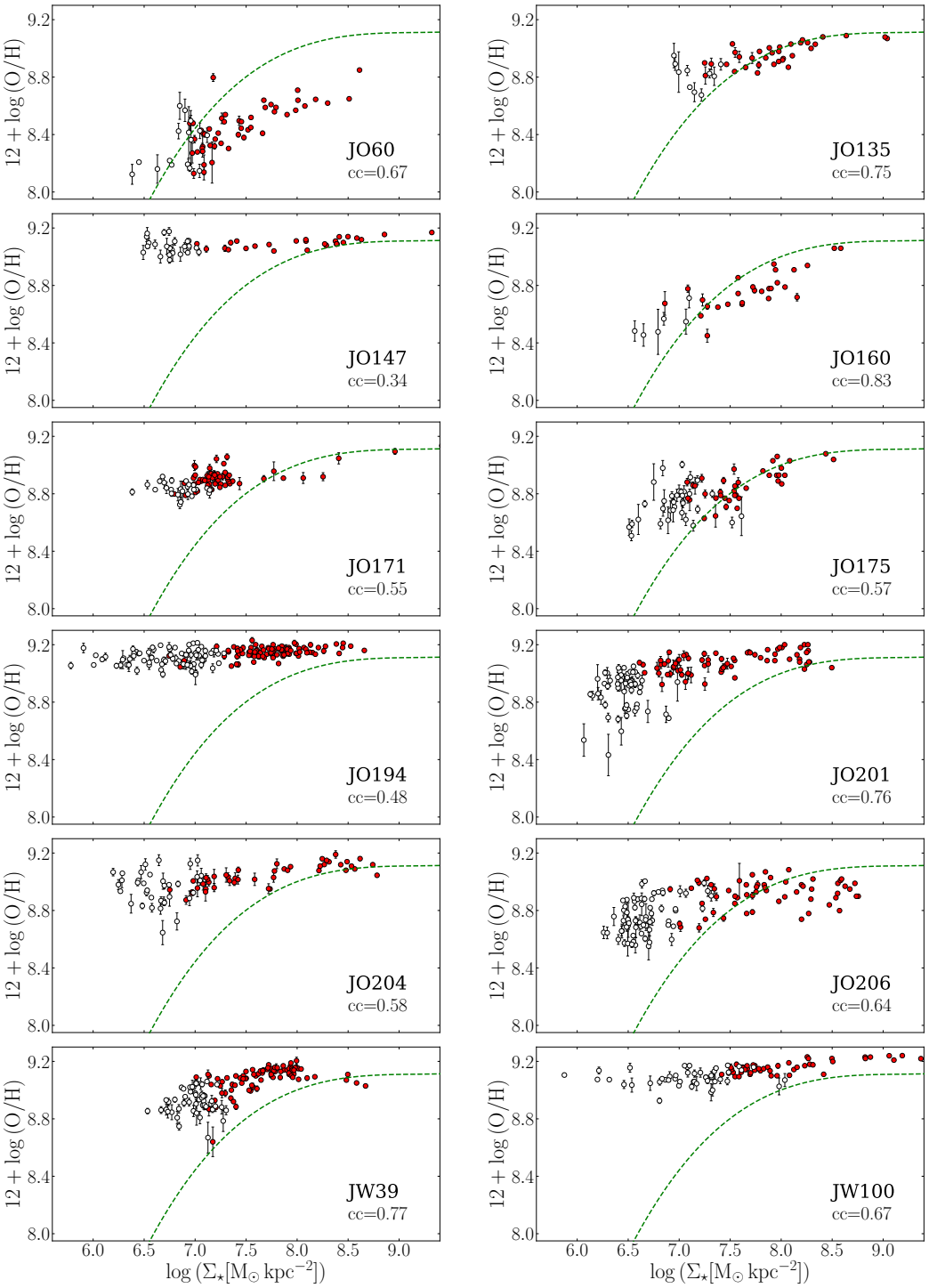

Figure 6.6: Metallicity *vs.* surface stellar mass density profile of all jellyfish galaxies. All plots share the same x-axis. Red filled dots are the knots$_{\rm in}$, the empty dots are the knots$_{\rm out}$. The green dashed line is the same as in Figure 5.11. The Spearman correlation coefficient of each profile is shown in panels.

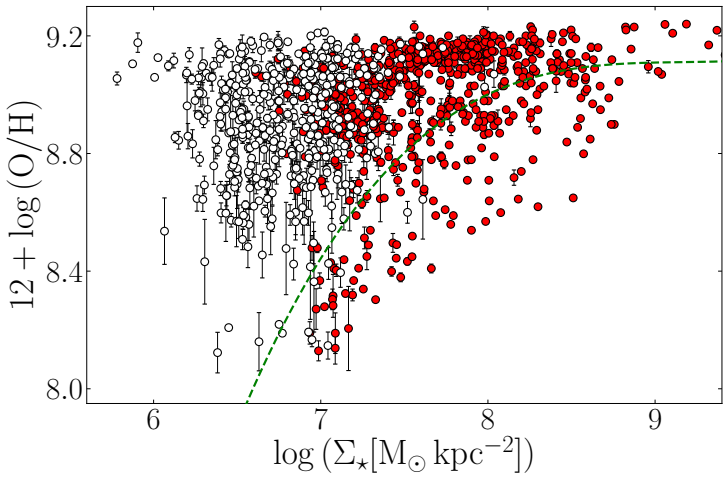

Figure 6.7: Metallicity *vs.* surface stellar mass density profile considering all knots of jellyfish sample galaxies. Red filled dots are the knots$_{\rm in}$, the empty dots are the knots$_{\rm out}$. The green dashed line is the same in Figure 5.11.

gradient within the main galaxy body and in most cases this trend continue also in the gas tails. This demonstrates that the ram-pressure stripping doesn't upset the metallicity gradient characteristic of the disk galaxies and that this mechanism removes the gas proceeding outside-in. However, the morphology and the metallicity distribution depends to the galaxy mass, the ICM density and the direction of the ram-pressure with respect to the galaxy plane, therefore each jellyfish galaxy represents a stand-alone case that it is worth to analyze individually. Finally, I have shown the disconnection between the metallicity of the knots and their stellar mass density. These results indicate that the ram-pressure removes only the gas from the galaxy, leaving intact the stellar component, but the gas stripped knots conserve the memory of the stellar evolution responsible to their metal-enrichment, at less than self-enrichment.

Chapter 7

Summary and future outlook

In this thesis, the metallicity properties of 10 disk galaxies with undisturbed morphology and 12 jellyfish galaxies were investigated. The work was performed in the context of the GASP project with the integral field spectroscopic provided by MUSE. The analysis of the emission line fluxes of the ionized gas in H_α knots has allowed to study the spatially resolved gas-phase metallicity across the whole extension of the target galaxies.

The photometric analysis carried out for the normal galaxies has derived the effective radius of the disk, that was used to rescale the metallicity distribution of these galaxies. All them exhibt a clear negative gradient in the radial range $0.5 - 1.5$ r_e with the mean slope $\alpha^{r_e}_{O/H} = -0.28 \pm 0.17$ dex/r_e consistent with the result of Sánchez-Menguiano et al. (2017). This rescaling has allowed to reveal common deviations from the negative gradient of some galaxies, such as outer flattening beyond 1.5 r_e and inner flattening within 0.5 r_e. The galaxies with inner metallicity flattening are the most massive ones of the control-sample according to Belfiore et al. (2017). The rescaling with the radius r_{25} has produced slopes spanning a wider spread and has prevented to find a common radial range between the inner and outer flattening. The effective radius resulted physically more meaningful than r_{25} indicating that the metallicity gradient and the surface brightness profile of the disk are the product of same physical mechanisms.

The jellyfish galaxies were analyzed separating the H_α knots belonging to the main galaxy body from those belonging to the stripped gas tails. The metallicity distribution in these galaxies shows negative gradients, both in the main galaxy body and in the tails, even if in some of the most massive galaxies quite flat gradients were observed. The result indicates that the ram-pressure stripping proceeds outside-in, removing the gas from the outer regions and then from the inner ones, and that the trace of the chemical enrichment history is still clearly visible in the gas tails.

This work has also focused on the mass-metallicity relation comparing the total

stellar mass of galaxies with their central metallicity. Galaxies with masses up to 10^{11} $M_{\odot}$ follow the linear correlation found by Hirschauer et al. (2018). At more high masses, the trend observed in my sample is less steep, but this flattening is still consistent with the observations found in the literature (Tremonti et al., 2004).

The analysis of the stellar mass density and local metallicity has found a good relation for the galaxies of the control-sample, though such relation has a second order dependence on the total stellar mass. The jellyfish galaxies manifest different behaviours; most knots belonging to the main galaxy body and all knots in the gas tails are more metal-rich than the average value found for the control-galaxies. The metallicity of the knots in the tails covers a range of 1 dex and their stellar mass density spans an order of magnitude with no evidence of a common relation between the two quantities. This result is consistent with the hypothesis that the stellar mass density of the knots in the stripped gas is due to the young stars born in situ, while the metallicity is connected with the whole stellar evolutionary history occurred in the disk (plus the eventual self-enrichment and mixing with the ICM).

This work is a first step into the systematical study of the global and local properties of the gas-stripped galaxies. In order to improve the study, the logical way to proceed will be to increase the sample of galaxies to analyze, focusing especially on the jellyfish galaxies. Only with the recent spectroscopic data provided by MUSE, the properties of these spectacular and complex objects can be explored with a level of detail that was never reached so far.

Most of the future work will focus on the search of physical interpretations capable to explain the observed global and local relations, both for the normal and gas-stripped galaxies. This scope requires to perform specific, detailed and individual studies of all jellyfish galaxies because many factors, such as the galaxy stellar mass, the environment, the orbits into the cluster, the galaxy plane inclination with respect to the velocity direction, make each one a stand-alone case.

To verify the interpretations that will come out from these in-depth observational studies, the comparison with models could be decisive. Models of galaxy evolution and chemical evolution could provide the counterpart of the observed properties of the normal galaxies, while hydrodynamical models of ram-pressure stripping could give a contribution to the understanding of jellyfish galaxy features.

Bibliography

Abadi M. G., Moore B., Bower R. G., 1999, MNRAS, 308, 947

Allen M. G., Groves B. A., Dopita M. A., Sutherland R. S., Kewley L. J., 2008, ApJS, 178, 20-55

Bacon R., et al., 2010, SPIE, 7735, 773508

Baldwin J. A., Phillips M. M., Terlevich R., 1981, PASP, 93, 5

Barnes J. E., Hernquist L., 1992, ARA&A, 30, 705

Barrera-Ballesteros J. K., et al., 2016, MNRAS, 463, 2513

Belfiore F., et al., 2017, MNRAS, 469, 151

Bellhouse C., et al., 2017, ApJ, 844, 49

Boissier S., Prantzos N., 1999, MNRAS, 307, 857

Boselli A., et al., 2016, A&A, 587, A68

Bresolin F., Ryan-Weber E., Kennicutt R. C., Goddard Q., 2009, ApJ, 695, 580

Bressan A., Marigo P., Girardi L., Salasnich B., Dal Cero C., Rubele S., Nanni A., 2012, MNRAS, 427, 127

Bundy K., et al., 2015, ApJ, 798, 7

Calvi R., Poggianti B. M., Vulcani B., 2011, MNRAS, 416, 727

Calzetti D., Kinney A. L., Storchi-Bergmann T., 1994, ApJ, 429, 582

Cardelli J. A., Clayton G. C., Mathis J. S., 1989, ApJ, 345, 245

Chabrier G., 2003, PASP, 115, 763

Cortese L., et al., 2007, MNRAS, 376, 157

Cowie L. L., Songaila A., 1977, Natur, 266, 501

Díaz A. I., Pérez-Montero E., 2000, MNRAS, 312, 130

Dopita M. A., Sutherland R. S., Nicholls D. C., Kewley L. J., Vogt F. P. A., 2013, ApJS, 208, 10

Dopita M. A., Kewley L. J., Sutherland R. S., Nicholls D. C., 2016, Ap&SS, 361, 61

Drory N., et al., 2015, AJ, 149, 77

Ebeling H., Stephenson L. N., Edge A. C., 2014, ApJ, 781, L40

Edmunds M. G., Pagel B. E. J., 1984, MNRAS, 211, 507

Fasano G., et al., 2006, A&A, 445, 805

Freeman K. C., 1970, ApJ, 160, 811

Fossati M., Fumagalli M., Boselli A., Gavazzi G., Sun M., Wilman D. J., 2016, MNRAS, 455, 2028

Fritz J., et al., 2017, ApJ, 848, 132

Fumagalli M., Fossati M., Hau G. K. T., Gavazzi G., Bower R., Sun M., Boselli A., 2014, MNRAS, 445, 4335

García-Benito R., et al., 2015, A&A, 576, A135

Gavazzi G., Bonfanti C., Sanvito G., Boselli A., Scodeggio M., 2002, ApJ, 576, 135

Giovanelli R., Haynes M. P., Salzer J. J., Wegner G., da Costa L. N., Freudling W., 1995, AJ, 110, 1059

Goetz M., Koeppen J., 1992, A&A, 262, 455

Groves B. A., Dopita M. A., Sutherland R. S., 2004, ApJS, 153, 75

Groves B., Dopita M., Sutherland R., 2006, A&A, 458, 405

Gullieuszik M., et al., 2015, A&A, 581, A41

Gullieuszik M., et al., 2017, ApJ, 846, 27

Gunn J. E., Gott J. R., III, 1972, ApJ, 176, 1

Gunn J. E., et al., 2006, AJ, 131, 2332

Gusev A. S., Pilyugin L. S., Sakhibov F., Dodonov S. N., Ezhkova O. V., Khramtsova M. S., 2012, MNRAS, 424, 1930

Haynes M. P., Giovanelli R., Chincarini G. L., 1984, ARA&A, 22, 445

Heckman T. M., 1980, A&A, 87, 152

Hirschauer A. S., Salzer J. J., Janowiecki S., Wegner G. A., 2018, arXiv, arXiv:1801.01133

Ho L. C., Filippenko A. V., Sargent W. L. W., 1997, ApJS, 112, 315

Husemann B., et al., 2013, A&A, 549, A87

Jaffe' Y. L., et al., 2018, arXiv, arXiv:1802.07297

Jedrzejewski R. I., 1987, IAUS, 127, 37

Kauffmann G., et al., 2003, MNRAS, 346, 1055

Kelz A., et al., 2006, PASP, 118, 129

Kennicutt R. C., Jr., 1998, ARA&A, 36, 189

Kepner J. V., 1999, ApJ, 520, 59

Kewley L. J., Heisler C. A., Dopita M. A., Lumsden S., 2001, ApJS, 132, 37

Kewley L. J., Dopita M. A., 2002, ApJS, 142, 35

Kewley L. J., Groves B., Kauffmann G., Heckman T., 2006, MNRAS, 372, 961

Kewley L. J., Ellison S. L., 2008, ApJ, 681, 1183-1204

Kewley L. J., Rupke D., Zahid H. J., Geller M. J., Barton E. J., 2010, ApJ, 721, L48

Kobulnicky H. A., Kewley L. J., 2004, ApJ, 617, 240

Larson R. B., Tinsley B. M., Caldwell C. N., 1980, ApJ, 237, 692

López-Sánchez Á. R., Dopita M. A., Kewley L. J., Zahid H. J., Nicholls D. C., Scharwächter J., 2012, MNRAS, 426, 2630

Magrini L., Vílchez J. M., Mampaso A., Corradi R. L. M., Leisy P., 2007, A&A, 470, 865

Marino R. A., et al., 2012, ApJ, 754, 61

Markwardt C. B., 2009, ASPC, 411, 251

Martin P., Roy J.-R., 1992, ApJ, 397, 463

Matteucci F., Francois P., 1989, MNRAS, 239, 885

McGaugh S. S., 1991, ApJ, 380, 140

McPartland C., Ebeling H., Roediger E., Blumenthal K., 2016, MNRAS, 455, 2994

Merluzzi P., et al., 2013, MNRAS, 429, 1747

Molla M., Diaz A., Ferrini F., 1996, ASPC, 98, 551

Moore B., Katz N., Lake G., Dressler A., Oemler A., 1996, Natur, 379, 613

Moretti A., et al., 2014, A&A, 564, A138

Moretti A., et al., 2017, A&A, 599, A81

Moretti A., et al., 2018, MNRAS,

Nulsen P. E. J., 1982, MNRAS, 198, 1007

Oey M. S., Kennicutt R. C., Jr., 1993, ApJ, 411, 137

Oey, M. S., Shields, J. C., Dopita, M. A., & Smith, R. C. 2002, Revista Mexicana de Astronomia y Astrofisica Conference Series, 12, 77

Osterbrock D. E., Ferland G. J., 2006, Astrophysics of gaseous nebulae and active galactic nuclei. Sausalito, CA: University Science Books

Pagel B. E. J., Edmunds M. G., Blackwell D. E., Chun M. S., Smith G., 1979, MNRAS, 189, 95

Peimbert, M., & Costero, R. 1969, Boletin de los Observatorios Tonantzintla y Tacubaya, 5, 3

Peimbert M., Rayo J. F., Torres-Peimbert S., 1978, ApJ, 220, 516

Pérez-Montero E., et al., 2016, A&A, 595, A62

Pettini M., Pagel B. E. J., 2004, MNRAS, 348, L59

Pilyugin L. S., 2001, A&A, 374, 412

Pilyugin L. S., Thuan T. X., 2005, ApJ, 631, 231

Pilyugin L. S., Grebel E. K., Kniazev A. Y., 2014, AJ, 147, 131

Poggianti B. M., et al., 2016, AJ, 151, 78

Poggianti B. M., et al., 2017, ApJ, 844, 48

Poggianti B. M., et al., 2017, Natur, 548, 304

Proxauf B., Öttl S., Kimeswenger S., 2014, A&A, 561, A10

Rich J. A., Torrey P., Kewley L. J., Dopita M. A., Rupke D. S. N., 2012, ApJ, 753, 5

Rosales-Ortega F. F., Kennicutt R. C., Sánchez S. F., Díaz A. I., Pasquali A., Johnson B. D., Hao C. N., 2010, MNRAS, 405, 735

Rosales-Ortega F. F., Díaz A. I., Kennicutt R. C., Sánchez S. F., 2011, MNRAS, 415, 2439

Rosales-Ortega F. F., Sánchez S. F., Iglesias-Páramo J., Díaz A. I., Vílchez J. M., Bland-Hawthorn J., Husemann B., Mast D., 2012, ApJ, 756, L31

Roth M. M., et al., 2005, PASP, 117, 620

Salzer J. J., et al., 2000, AJ, 120, 80

Sánchez S. F., et al., 2012, A&A, 538, A8

Sánchez S. F., et al., 2012, A&A, 546, A2

Sánchez S. F., et al., 2014, A&A, 563, A49

Sánchez S. F., et al., 2016, A&A, 594, A36

Sánchez S. F., et al., 2017, MNRAS, 469, 2121

Sánchez-Menguiano L., et al., 2016, A&A, 587, A70

Sánchez-Menguiano L., et al., 2017, arXiv, arXiv:1710.01188

Searle L., 1971, ApJ, 168, 327

Sérsic J. L., 1968, Atlas de Galaxias Australes. Observatorio Astronómico, Córdoba, Argentina

Schlafly E. F., Finkbeiner D. P., 2011, ApJ, 737, 103

Sharp R. G., Bland-Hawthorn J., 2010, ApJ, 711, 818

Smee S. A., et al., 2013, AJ, 146, 32

Stasińska G., 2002, Revista Mexicana de Astronomia y Astrofisica Conference Series, 12, 62

Stasińska G., 2005, A&A, 434, 507

Storey P. J., Zeippen C. J., 2000, MNRAS, 312, 813

Sutherland R. S., Dopita M. A., 1993, ApJS, 88, 253

Tremonti C. A., et al., 2004, ApJ, 613, 898

van Zee L., Salzer J. J., Haynes M. P., O'Donoghue A. A., Balonek T. J., 1998, AJ, 116, 2805

Veilleux S., Cecil G., Bland-Hawthorn J., 2005, ARA&A, 43, 769

Verdes-Montenegro L., Yun M. S., Williams B. A., Huchtmeier W. K., Del Olmo A., Perea J., 2001, A&A, 377, 812

Vila-Costas M. B., Edmunds M. G., 1992, MNRAS, 259, 121

Vollmer B., Cayatte V., Balkowski C., Duschl W. J., 2001, ApJ, 561, 708

Vulcani B., et al., 2017, ApJ, 850, 163

Vulcani B., et al., 2018, ApJ, 852, 94

Zaritsky D., Kennicutt R. C., Jr., Huchra J. P., 1994, ApJ, 420, 87

Zinchenko I. A., Pilyugin L. S., Grebel E. K., Sánchez S. F., Vílchez J. M., 2016, MNRAS, 462, 2715

Appendix A

Figures

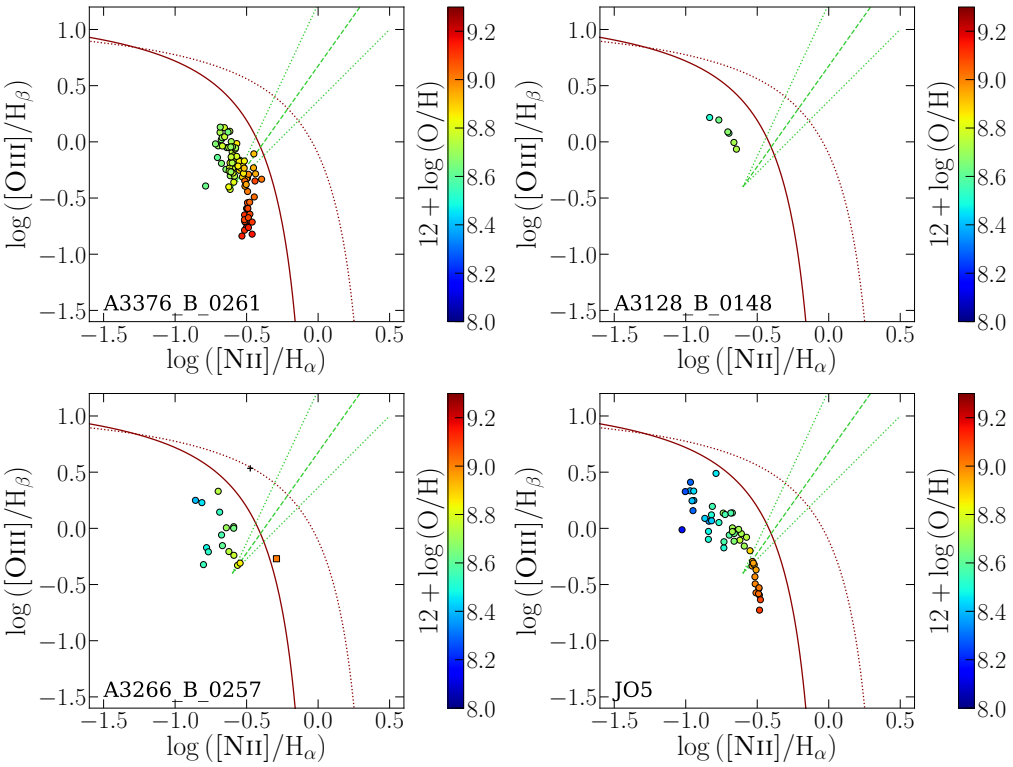

Figure A.1: Diagnostic diagrams described in Section 4.3. The lines correspond to the Eq. 4.4 (*solid red*), Eq. 4.5 (*dotted red*) and Eq. 4.6 (*dashed green*). The dots indicate the knots powered by stellar photoionization (*circle*), composite source (*square*), AGN (*triangle up*) or LINER (*triangle down*). The color-code indicate the metallicity of the knot. The crosses indicate the knots without metallicity estimate.

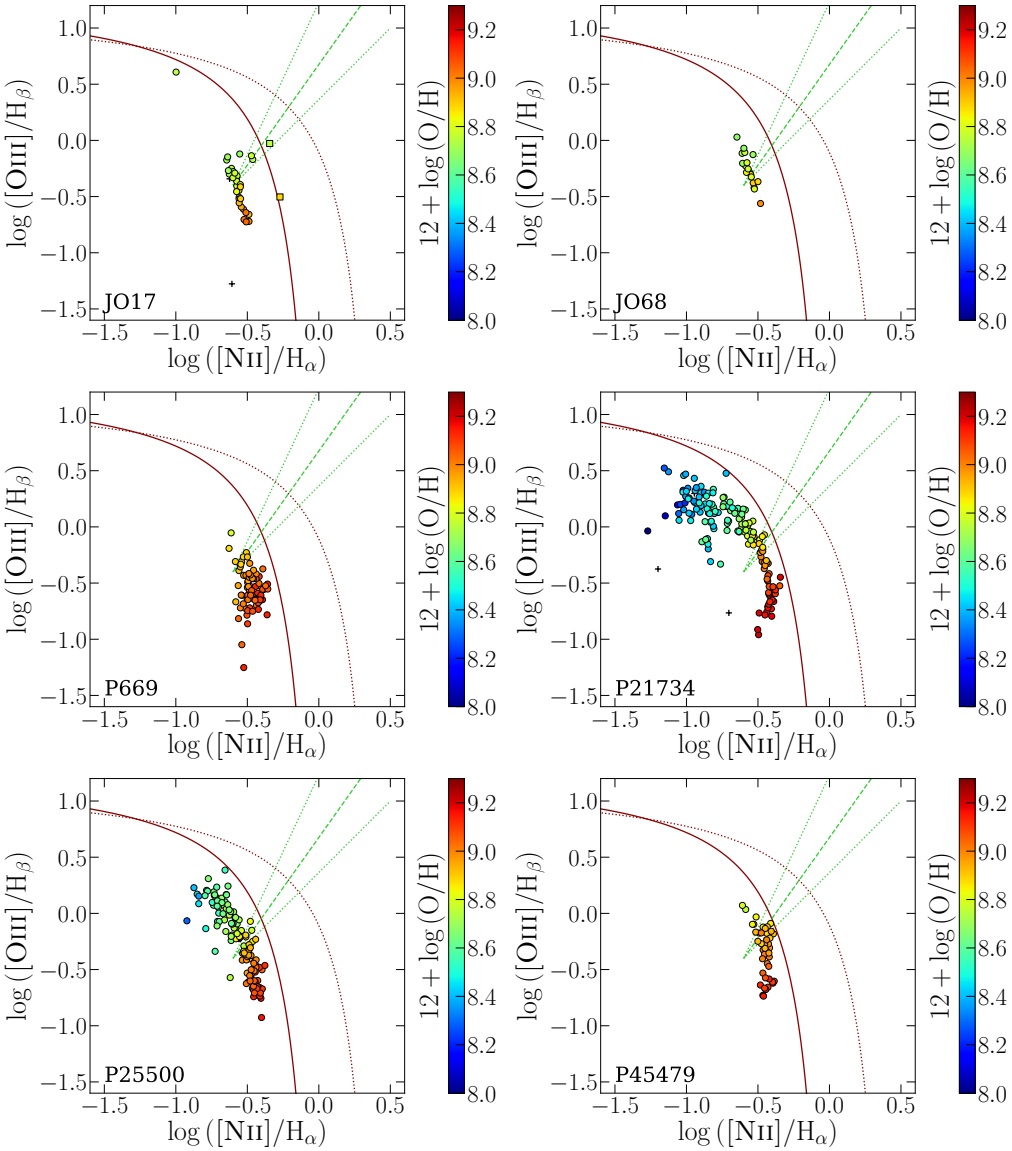

Figure A.1: (*Continued*)

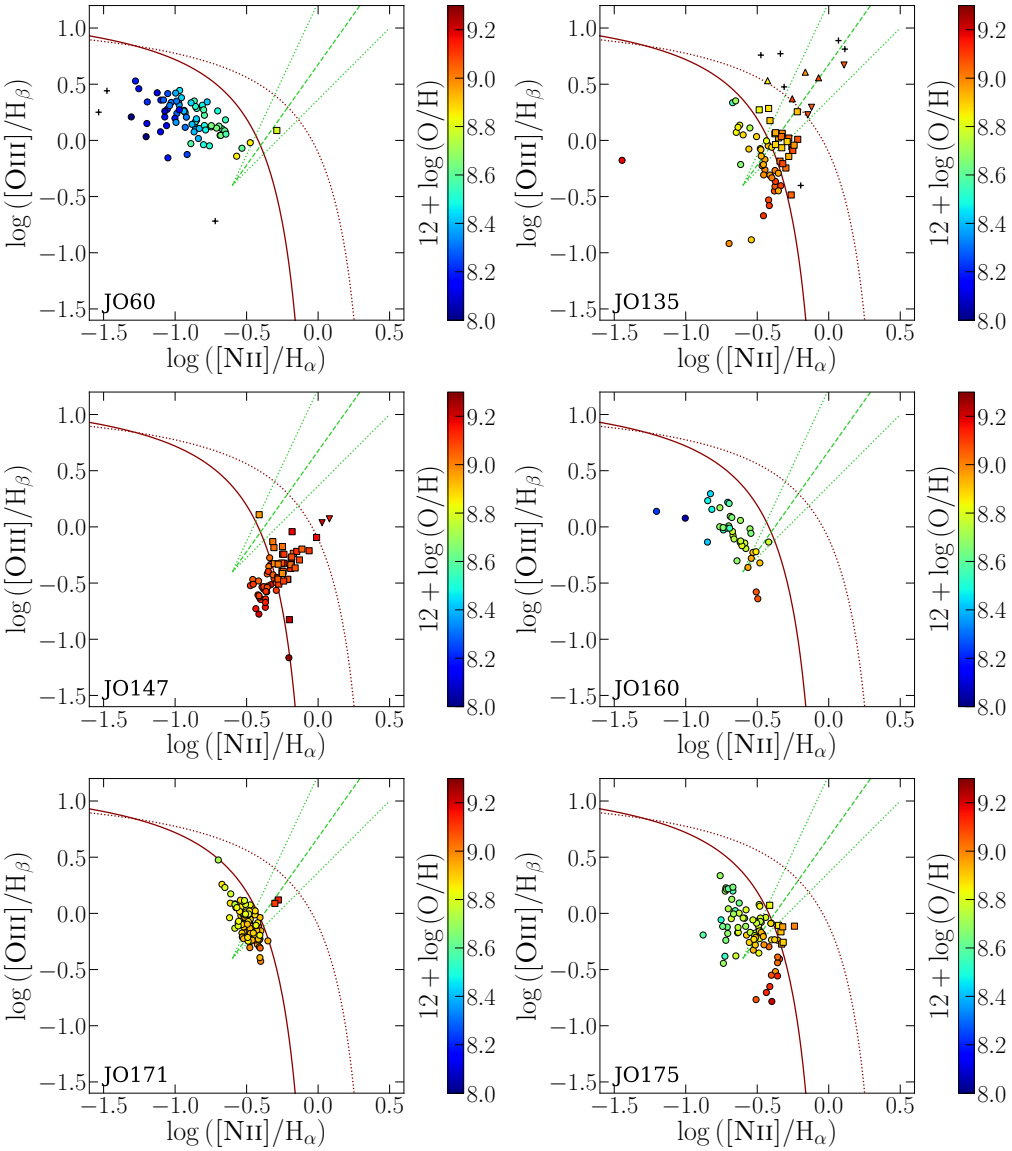

Figure A.1: (*Continued*)

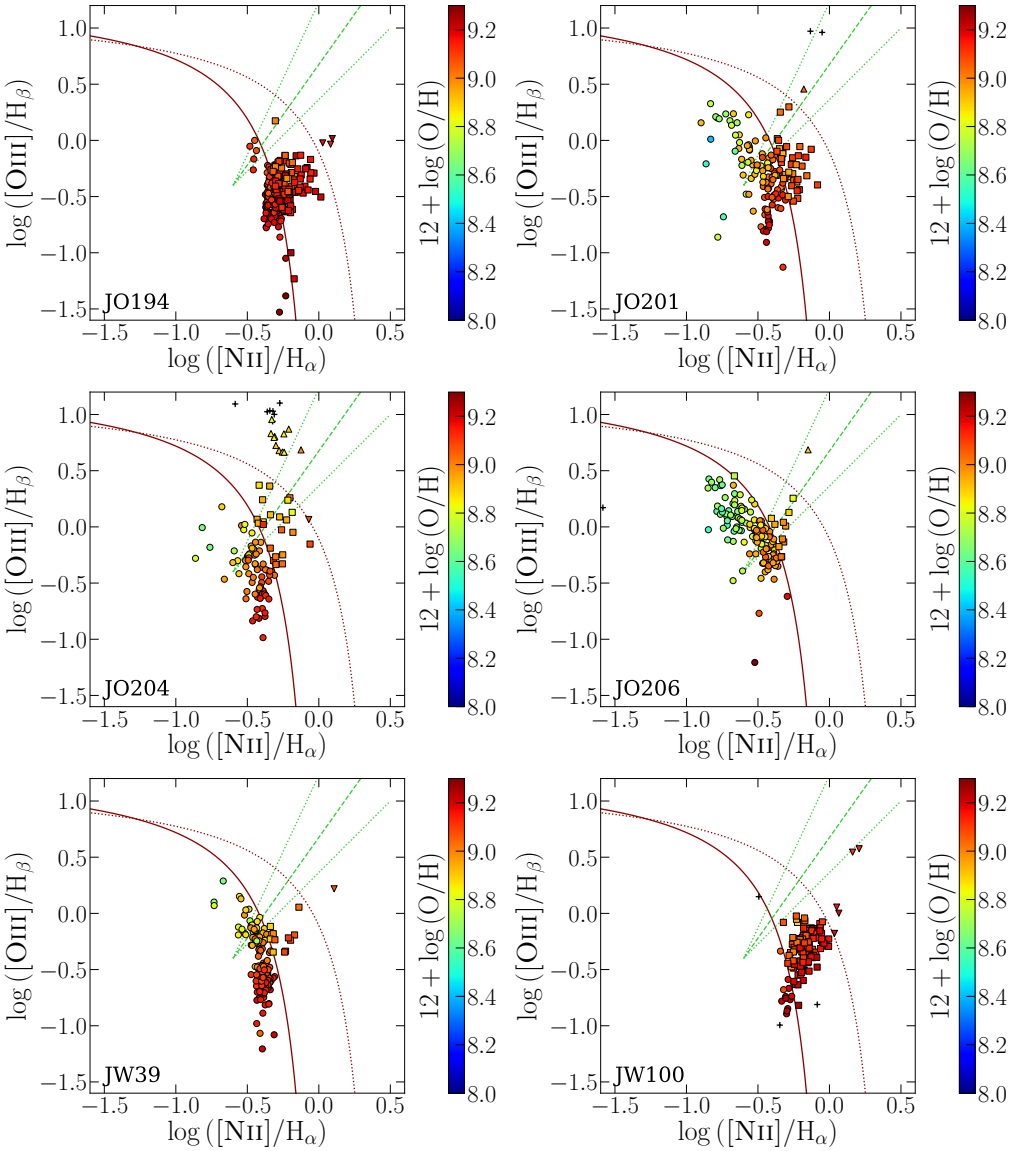

Figure A.1: (*Continued*)

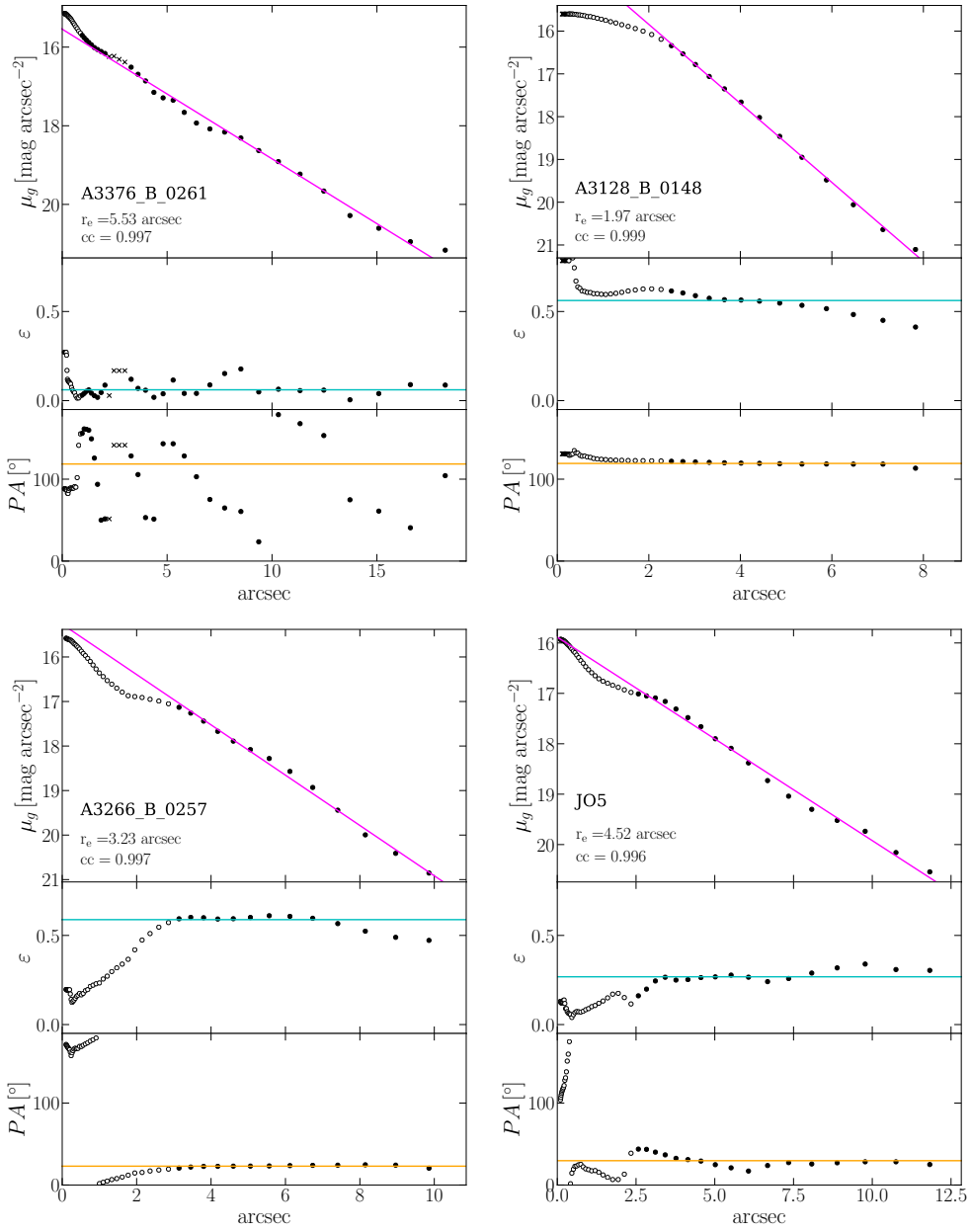

Figure A.2: Surface brightness, ellipticity and position angle profiles for the control-sample galaxies. The black dots are the data that present the best Pearson correlation coefficient (reported in the plot) between brightness surface and semi-major axis length and used to compute the effective radius (reported in the plot), the mean ellipticity and the position angle. The white dots are the data excluded by linear fit and the crosses are the invalid data. See Section 4.5

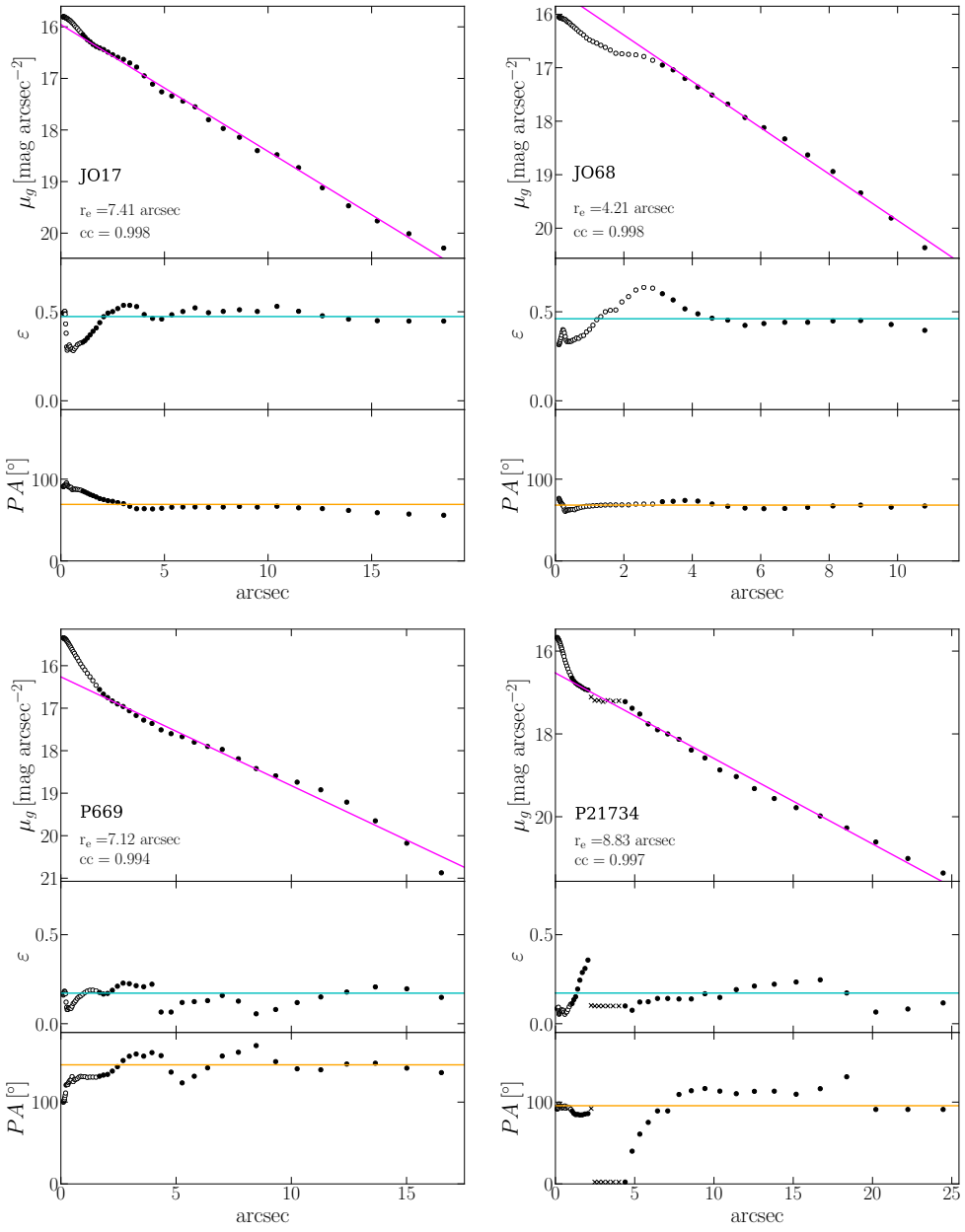

Figure A.2: (*Continued*)

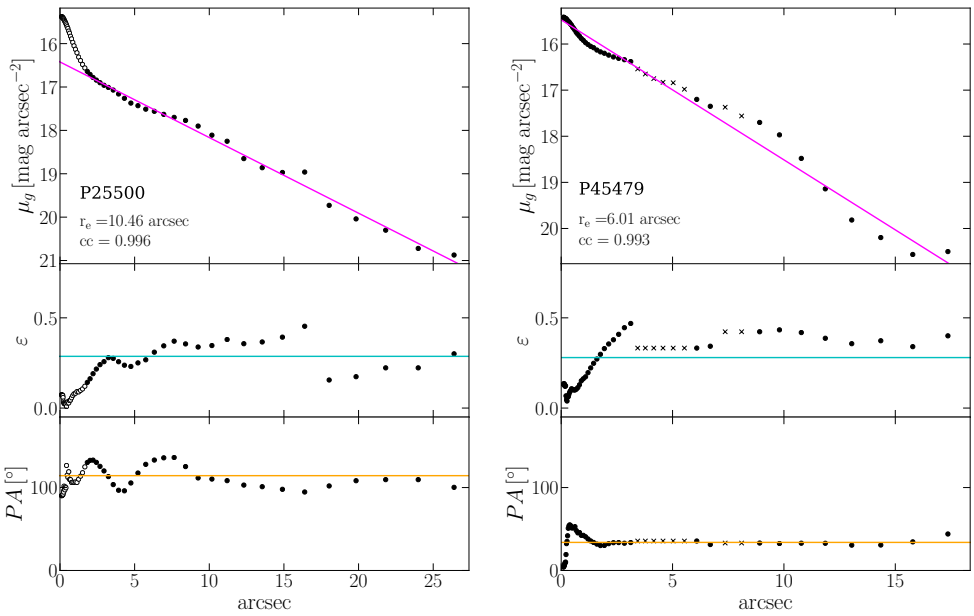

Figure A.2: (*Continued*)

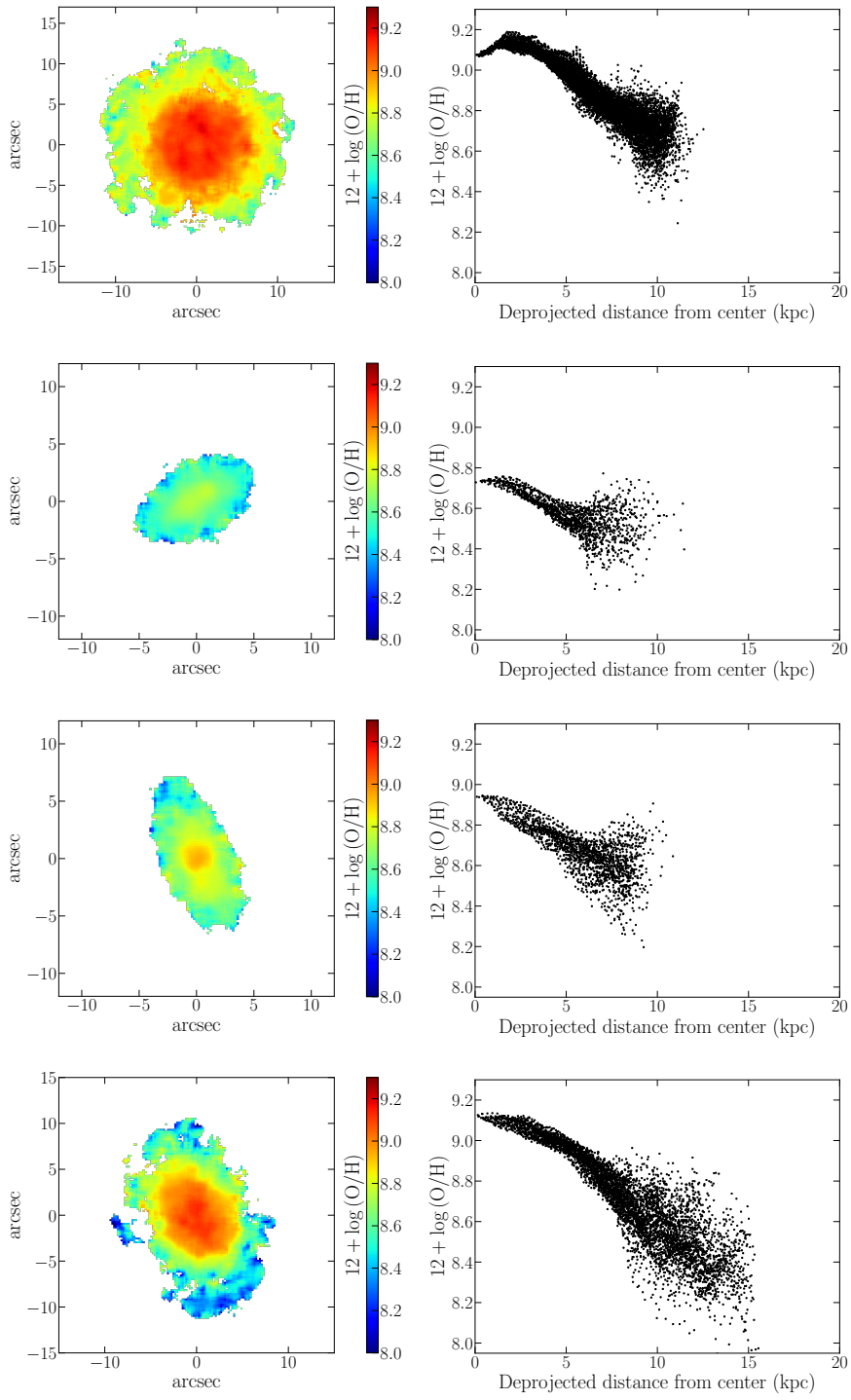

Figure A.3: *From top*: metallicity maps (*left panels*) and radial profile (*right panels*) -spaxel by spaxel- of A3376B0261, A3128B0148, A3266B0257 and JO5. In these and all maps, (0,0) is the center of the galaxy.

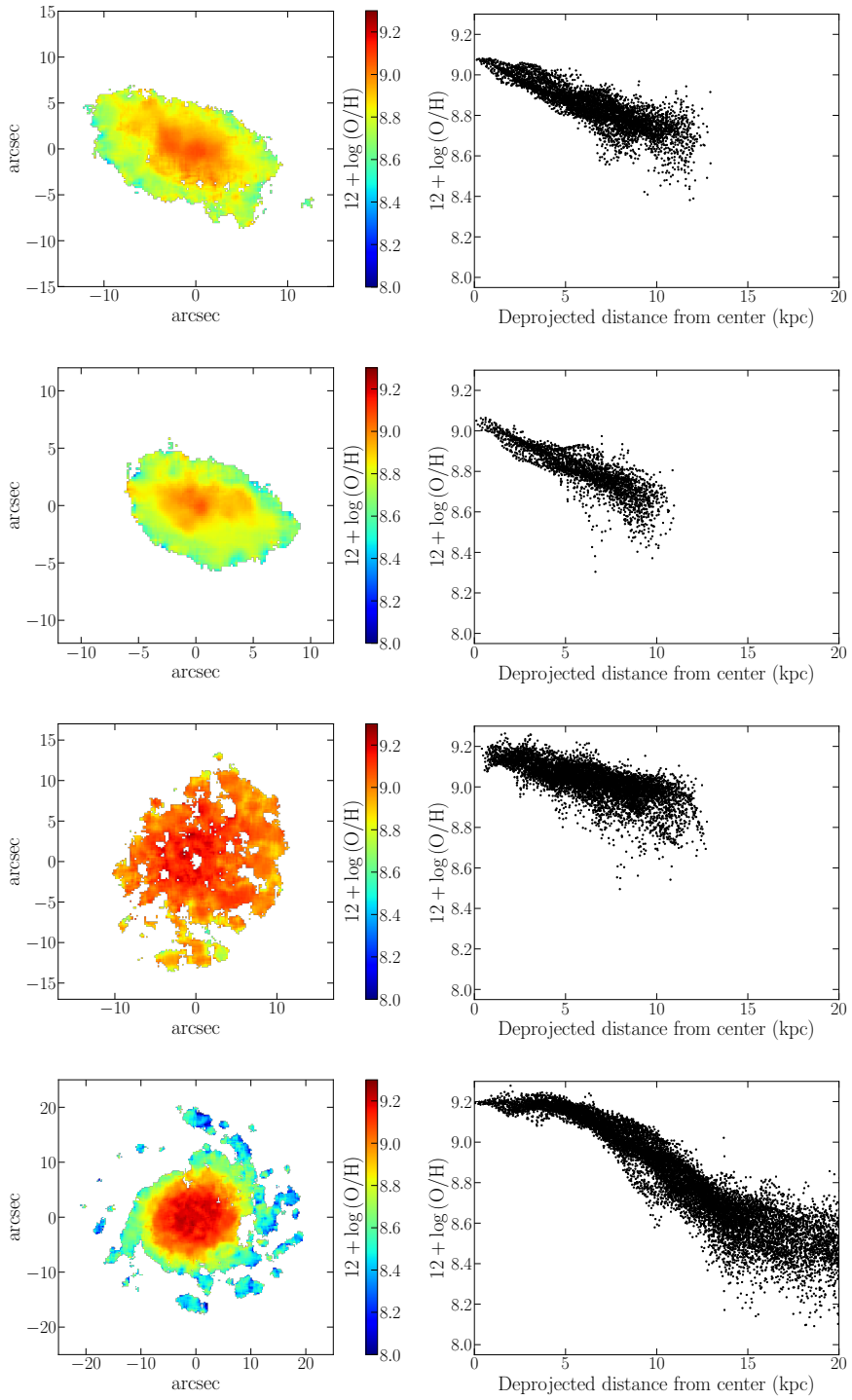

Figure A.4: *From top*: metallicity maps (*left panels*) and radial profile (*right panels*) -spaxel by spaxel- of JO17, JO68, P669 and P21734.

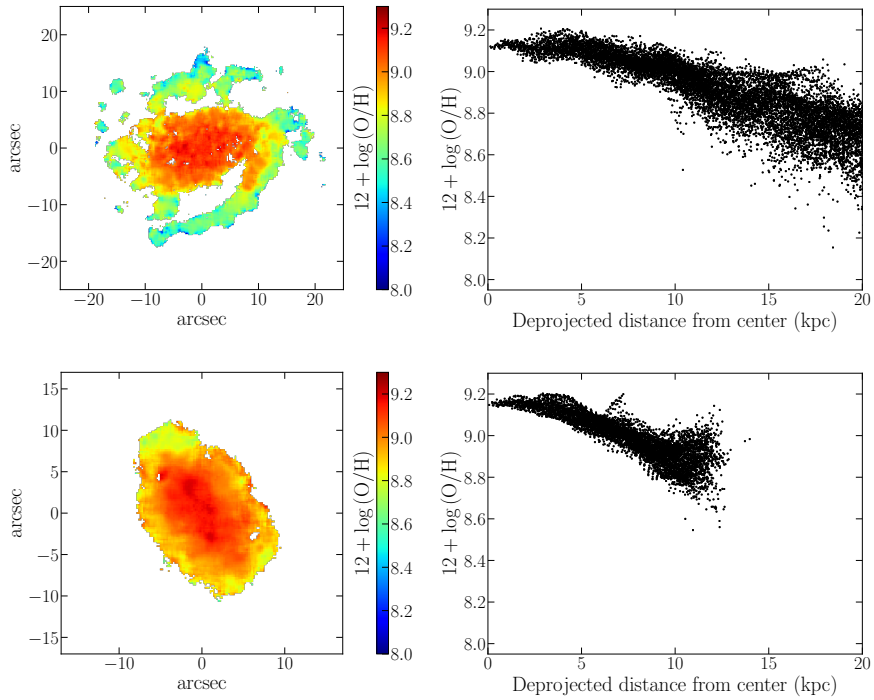

Figure A.5: *From top*: metallicity maps (*left panels*) and radial profile (*right panels*) -spaxel by spaxel- of P25500 and P45479.

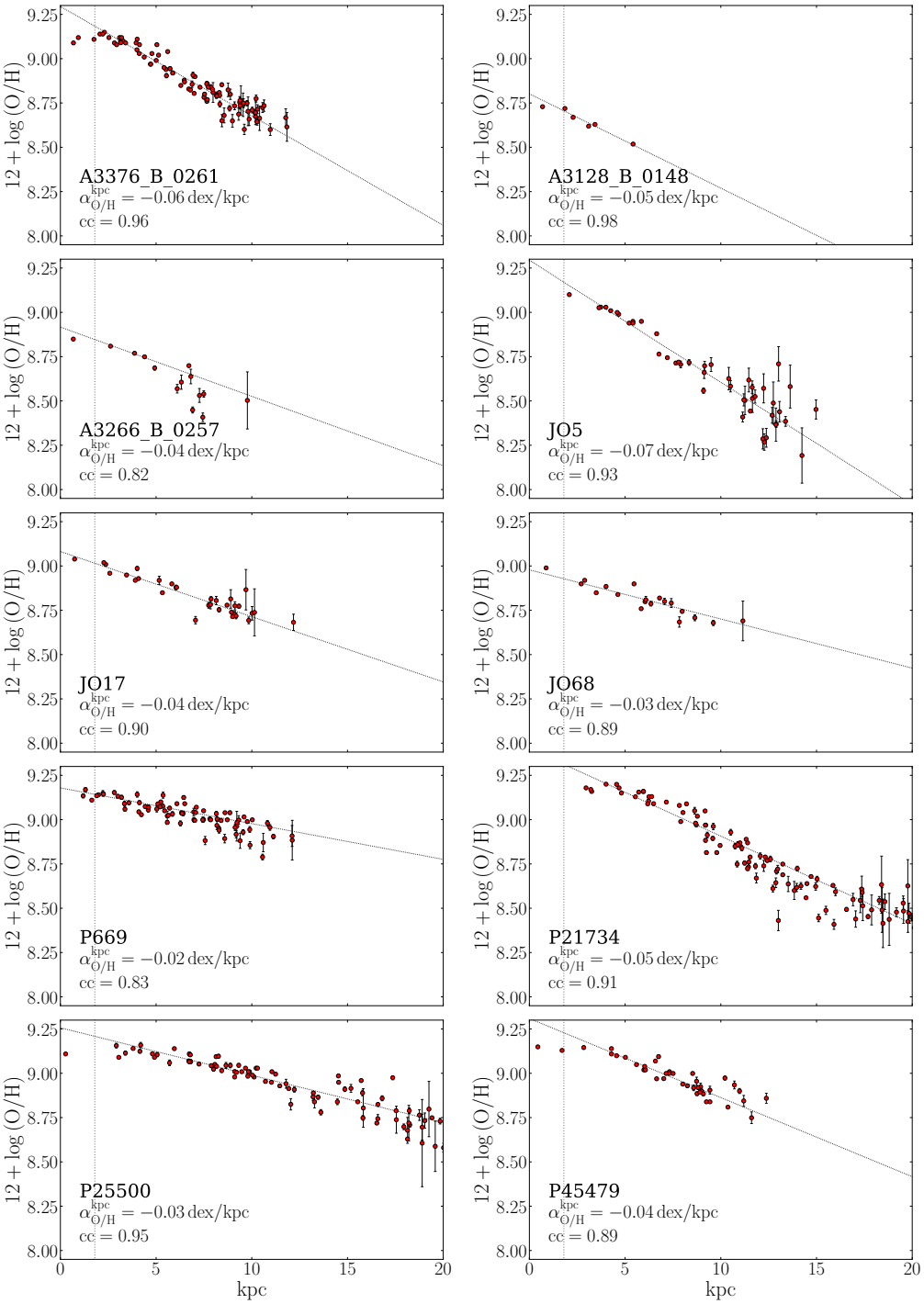

Figure A.6: Knot metallicity profiles of all control-sample galaxies with radial distance in physical units (kpc). All plots share the same x-axis. The black dotted line represents the linear fit performed excluding data within the vertical dotted line. The Pearson correlation coefficient and the mean slope are shown in each panel.

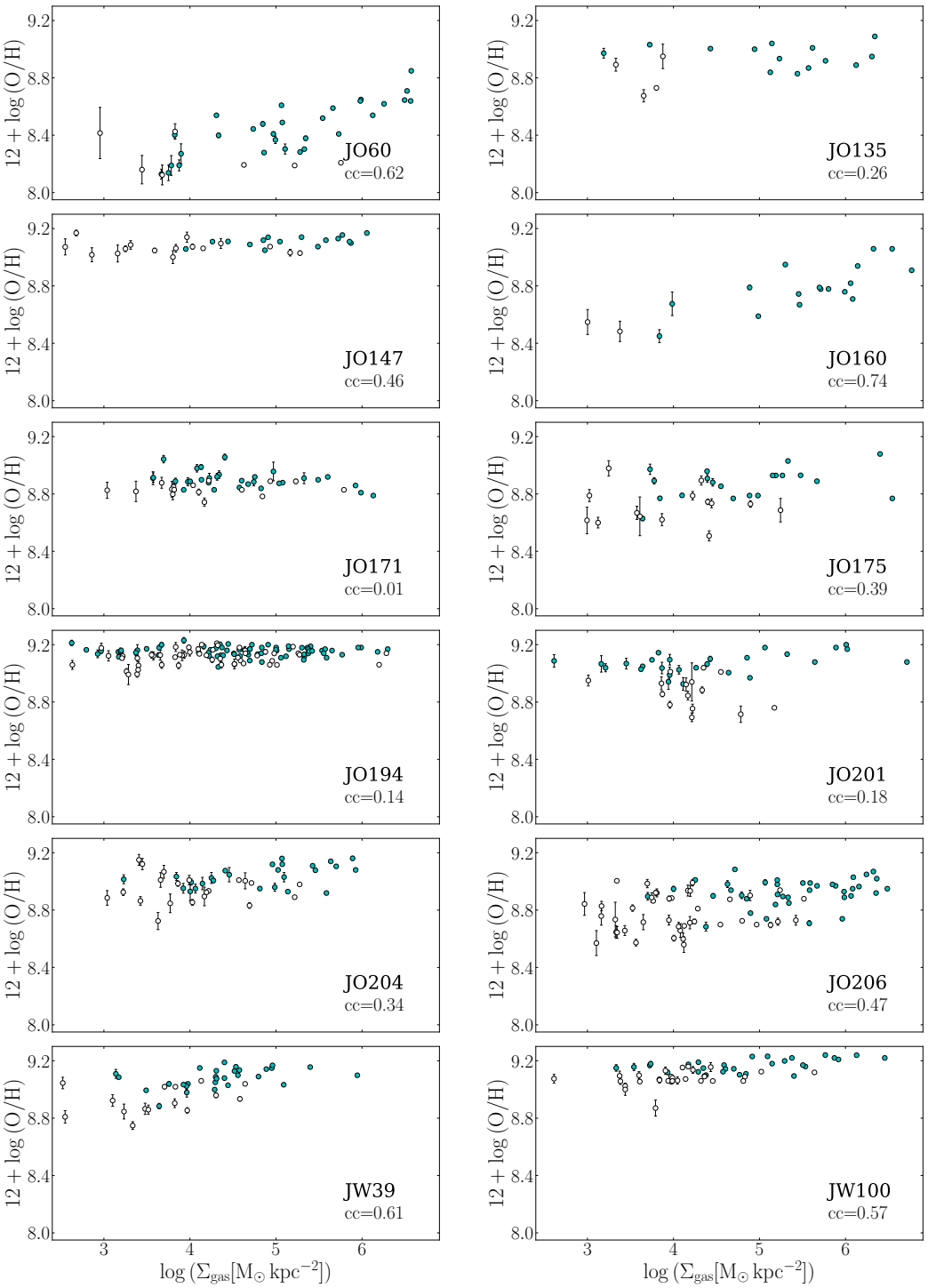

Figure A.7: Metallicity *vs.* surface gas mass density profile of all jellyfish galaxies. All plots share the same x-axis. Cyan filled dots are the knots$_{\rm in}$, the empty dots are the knots$_{\rm out}$. The Spearman correlation coefficient of each profile is shown in panels.

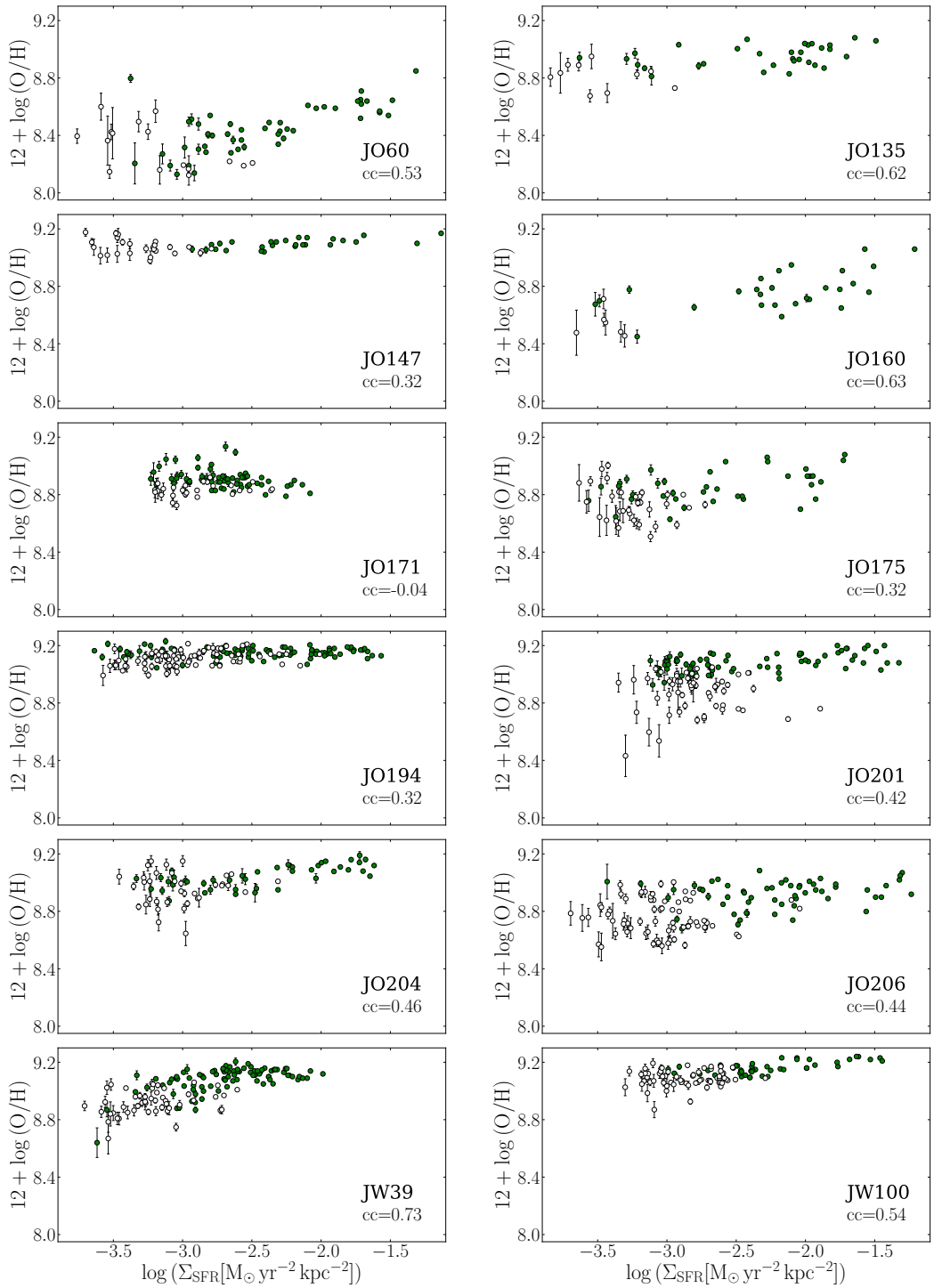

Figure A.8: Metallicity *vs.* star formation rate density profile of all jellyfish galaxies. All plots share the same x-axis. Green filled dots are the knots$_{\rm in}$, the empty dots are the knots$_{\rm out}$. The Spearman correlation coefficient of each profile is shown in panels.

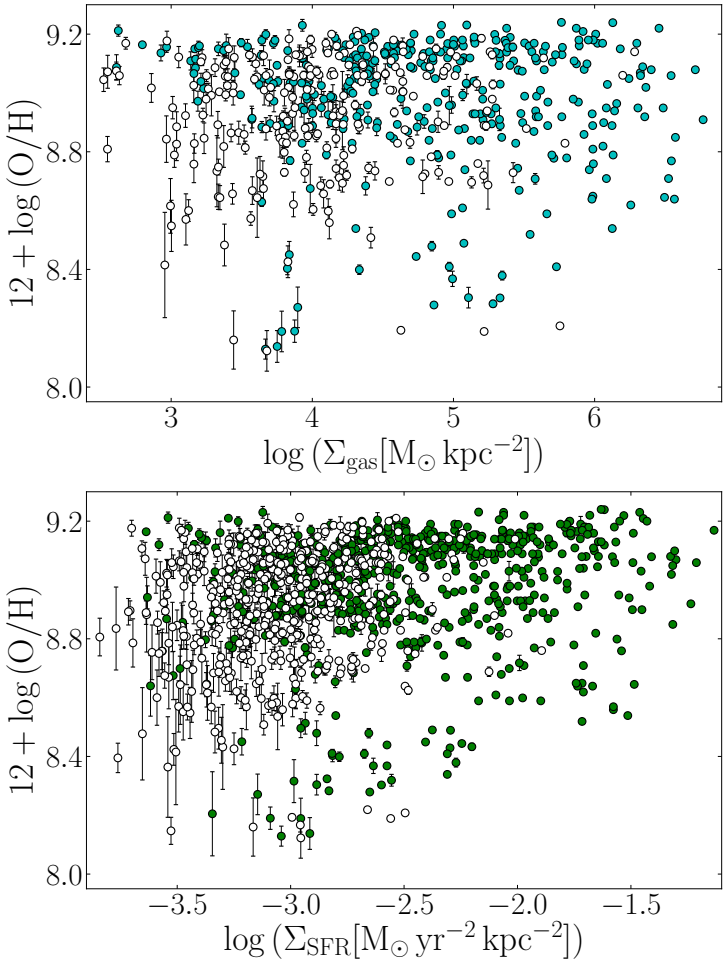

Figure A.9: Metallicity *vs.* surface gas mass density profile (*top panel*) and metallicity *vs.* star formation rate density profile (*bottom panel*) considering all knots of jellyfish sample galaxies. Filled dots are the knots$_{\rm in}$, the empty dots are the knots$_{\rm out}$.

Ringraziamenti

Vorrei, innanzitutto, esprimere la mia gratitudine verso l'intero team di GASP, che mi ha accolto con calore facendomi sentire subito parte del gruppo.

Un ringraziamento speciale è riservato a Bianca e Marco che mi hanno guidato con professionalità, pazienza e grandissima disponibilità in questo percorso di 6 mesi. Mi hanno dato l'opportunità di costruire con soddisfazione un lavoro, che spero possa dimostrare il mio impegno, dedizione e valore.

Ringrazio mia sorella Sara e mio fratello Stefano per avermi supportato e sopportato per tutti questi anni, incoraggiandomi in questa mia impresa.

Infine, la persona a cui sono più grato per il raggiungimento di questo traguardo è mia mamma. Lei mi ha sostenuto ad ogni livello, offrendomi sempre il suo appoggio in questo lungo cammino. Devo a lei il conseguimento di questa laurea, consapevole che questa dedica sia solo una goccia rispetto al mare di affetto che mi ha dato.